University of Reading

Department of Meteorology
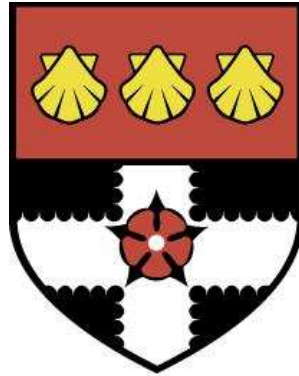
Boundary-layer type classification

and pollutant mixing

Natalie Jane Harvey

A thesis submitted for the degree of Doctor of Philosophy

March 2013

Skymap (11am)

Cloud

another cloud

Cloud

cloud

Cloud

cloud

another cloud

cloud

cloud

cloud

cloud

cloud

cloud

yet another cloud

cloud

cloud

cloud

cloud

cloud

Declaration

I confirm that this is my own work and the use of all material from other sources has been properly and fully acknowledged.

Natalie Harvey

Abstract

In the atmospheric boundary layer the vertical distribution of heat, momentum, water and pollutants is controlled by mixing that is turbulent. This complex mixing is parameterized in weather forecast and climate models. But are the parameterizations implemented in these models representative of the real world?

For the first time, Doppler lidar and sonic anemometer data are used to objectively classify the observed boundary layer into nine different types based on the Met Office scheme. Examples of these types are decoupled stratocumulus cloud, cumulus capped and stable with no turbulent cloud. This method is applied to three years of data from the Chilbolton Observatory, UK, to create a climatology of boundary-layer type. This climatology exhibits clear seasonal and diurnal cycles with the most common type over the three years being a cloud-free stable boundary layer. The decoupled stratocumulus type and the cumulus cloud under a stratocumulus layer type are diagnosed 10.3% and 1.0% of the period respectively.

This new observationally based boundary layer classification is used to evaluate the boundary-layer type diagnosed by the 4 km and 12 km resolution versions of the Met Office Unified Model. The model is found to predict too many decoupled stratocumulus boundary layers by a factor of 1.8, in both the stable and unstable regime. Stratocumulus cloud is present in the morning in the model but it is underestimated in the afternoon. The skill of the model in predicting boundary-layer type at the correct time has also been assessed using the symmetric extremal dependence index measure of skill. This analysis revealed that the skill of predicting the correct boundary-layer cloud type was much lower than the skill of predicting the presence of cloud. The skill of prediction is not affected by model resolution.

Finally, a set of idealised single column modelling experiments have been conducted to investigate the impact of boundary-layer type diagnosis on the vertical distribution of pollutants. It is shown that night-time near-surface concentrations are modulated by an order of magnitude depending on the sign of the predicted surface heat flux and mixing driven by stratocumulus cloud-top cooling acts to keep the residual layer well mixed. During the day the diagnosis of boundary-layer type has little impact on near-surface concentrations; however, the presence of cumulus cloud can modify the shape of the vertical distribution of tracer.

Acknowledgements

First and foremost I would like to thank my supervisors, Helen Dacre and Robin Hogan, for their time, encouragement and support throughout my PhD. I would also like to apologise to Robin for still not really knowing when to use a semi-colon!

I would also like to thank the my monitioring committee, Stephen Belcher and Peter Jan van Leeuwen, for keeping me on track and being interested in my work. I have also had great support and encouragement from both the Boundary Layer and Radar Groups. Particular mentions must go to Alan Grant, Janet Barlow and Ewan O'Connor. In the final stages of my PhD, when I was trying to setup a "simple" single column model I benefitted greatly from the help, knowledge and patience of the NCAS CMS team - thank you.

Thanks must also go to all my friends here in the department, especially Luke, Amanda, Matt and James - my fellow inhabitants of 2U07. Our conversations about Masterchef and The Great British Bake Off are truly memorable.

Finally, I would like to thank Ben for his all his help along my PhD journey. He has been a font of useful meteorological and programming information as well as an amazingly understanding husband!

Contents

Chapter 1

Introduction

1.1 Motivation

Man-made atmospheric pollutants have been a problem to human health since the start of the industrial revolution, primarily due to the burning of fossil fuels and the associated release of soot and sulphur dioxide into the atmosphere. Understanding how pollutants are emitted, transformed and transported throughout the atmosphere has important implications for human health. For instance, it has been estimated that urban outdoor pollution, primarily particulate matter, was responsible for 800,000 deaths world wide in the year 2000, with 23,000 of these in central and western Europe (Cohen et al., 2004). This number is of the same order of magnitude as the average number of deaths from seasonal influenza (World Health Organisation, 2003). A further study by Cohen et al. (2005) attributes fine particulate matter as the cause of 5% of lung cancer deaths and 3% of cardiopulmonary deaths world wide. It is estimated that human-produced fine particulate matter reduces life expectancy in the European Union by 8.6 months (World Health Organisation, 2006).

Air pollution events tend to be episodic. One such episode occurred in Europe during the August 2003 heat wave. The estimated number of air pollution related deaths in the UK during this period was 400–800 (Stedman, 2003). It is also estimated that the same event brought forward over 1000 deaths in the Netherlands (Fischer et al., 2003). With such impacts on human health the dispersion of these pollutants is an important process to understand. Plant seeds, pollen and disease spores are also dispersed into the atmosphere in a similar way to pollutants and this dispersal needs to be understood to manage agricultural crops effectively (Pan et al., 2012).

Forecasting air quality requires the representation of many complex meteorological and chemical processes, particularly in the atmospheric boundary layer. A key process to understand is turbulent mixing. This mixing impacts the dispersal of pollutants in the atmosphere as well as playing an important role in the fluxes of many other meteorological variables such as moisture, heat and momentum. These variables are key for the evolution of the atmospheric boundary layer and clouds and therefore the dynamics of weather forecast and climate prediction models.

1.2 Meteorological effects on air quality

There are many meteorological factors that affect the dispersion of pollutants. Figure 1.1 summarises the key processes. These include wind speed and direction, atmospheric stability, the structure and height of temperature inversions and the presence of clouds and precipitation. The wind speed and direction influences the speed and direction of the dispersion of pollutants. Temperature inversions cap the boundary layer and act as a lid on the vertical distribution of pollutants. This height determines volume of atmosphere that the pollutants can be dispersed throughout.

Pollution episodes occur in both clear and cloudy conditions but some pollutants, such as ozone, are more active in direct sunlight (Hobbs, 2000). Therefore the presence of cloud can be important for chemical transformations. Clouds also contribute to the turbulent mixing within the boundary layer. Humidity can also have an effect on the rate of some chemical reactions. Precipitation can reduce the amount of pollution in the atmosphere by wet deposition and scavenging effects . The timing of the passage of synoptic features, such as fronts (e.g. Donnell et al., 2001), and the presence of sea breezes also have an impact on the distribution of pollutants (e.g. Angevine et al., 2004 and Dacre et al., 2007). Finally, chemical species can influence the weather by changing the atmospheric radiation budget (e.g Ramanathan et al., 2001) as well as through cloud formation.
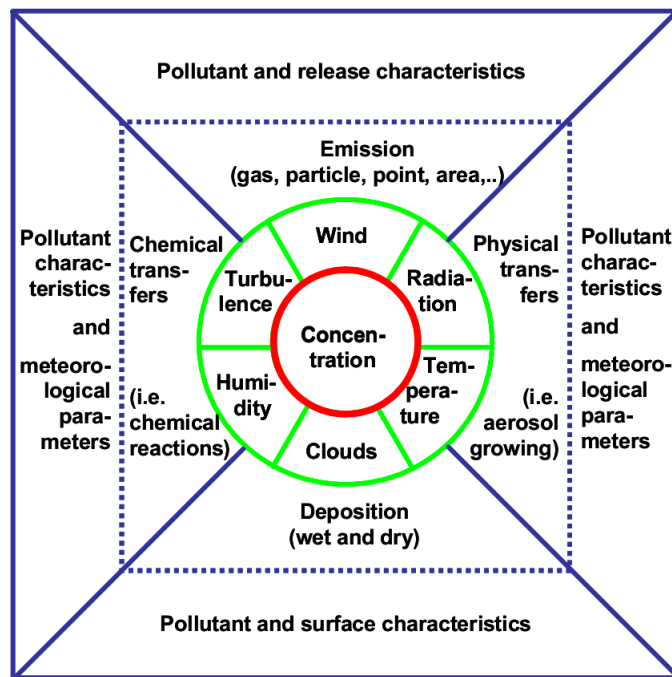
Figure 1.1: A schematic of the meteorological parameters (green circle) and the pollutant characteristics (blue square) that can affect air quality forecasts. Taken from Schlunzen & Sokhi (2006).

1.3 Forecasting air quality

1.3.1 Air quality model summary

Modelling air quality is complex as it involves the coupling of chemical emissions and transformations with meteorological transport processes.

Simple models, such as Gaussian plume and box models, make many assumptions and use simplified meteorological data. Examples of this type of model are the fine resolution atmospheric multi-pollutant exchange (FRAME) (Singles et al., 1998) and the Hull acid rain model (HARM) (Metcalfe et al., 2001). These models can be used to assess the long-term annual mean deposition of reduced and oxidised nitrogen and sulphur. Due to the lack of complexity in these models they can be run multiple times very quickly and therefore can be used to provide uncertainty estimates.

More comprehensive models, such as the Community Mulit-scale Air Quality (CMAQ) model (Byun & Schere, 2006) used by DEFRA, combine the meteorology and chemistry. There are two ways to do this, online or offline. Offline modelling runs a meteorological model separately and uses this data as an input for a chemistry transport model typically every 1–3 hours. This approach is common and, due to the low operational costs, enables ensembles to be run quickly in the case of accidental releases. However, this method

relies on the meteorological input data representing the variability of the meteorological features. Studies have found that the accuracy of chemistry transport models (CTMs) are impacted by the temporal frequency (Grell et al., 2004; Davis & Dacre, 2009; Korsholm et al., 2009) and horizontal resolution of the meteorological data (Queen & Zhang, 2008; Wolke et al., 2012). A spectral analysis of winds by Grell et al. (2004) found that scales of motion with time frequencies less than 10 minutes contribute to the total variability so ideally offline models require a meteorological output time of less than 10 minutes. Therefore to ensure accurate results from CTMs large amounts of meteorological data need to be archived.

De Meij et al. (2009) compared the impact of meteorological input data from the MM5 and WRF model in the Po Valley, Italy. In this case, the particulate matter concentrations were underestimated by a factor of 2 in simulations using the MM5 data and a factor of 3 using the MM5 data in winter conditions. These differences were due to differences in predicted boundary-layer depth. The underestimate of particulate matter is a common problem in air quality modelling and studies by Hongisto (2005) and Minguzzi et al. (2005) showed that uncertainties in meteorological fields, e.g. mixing height, temperature and wind speed, contribute to this problem. However, a study by Smyth et al. (2006) found that the largest difference between the meteorological fields in the GEM and MM5 models was relative humidity. The meteorological data with the higher relative humidity lead to larger predicted particulate matter concentrations due to an increase in particle bound water. However, Mueller (2009) found that wind direction was the main contributor to the low skill of predicting particulate matter concentrations. The importance of wind direction was also found by Warner et al. (1983).

As meteorological models have been developed separately to CTMs there are also errors when linking them as they can have different horizontal and vertical resolutions (Seaman, 2000). Also, offline simulations mean that the chemistry is not able to feedback on the meteorology. Other offline methods of predicting air quality include combining principal component regression of 15 different meteorological variables with the air quality index of the day before(Kumar & Goyal, 2011) and linear regression of synthetic tracer to reconstruct particulate matter concentrations (Fang et al., 2013).

Online coupling is numerically more consistent and allows two way interaction between the meteorological fields and chemistry and therefore includes feedbacks and could improve weather forecasts. This approach means that the same parameterisations and time-step are used for both the meteorology and chemistry and large amounts of me-

teorological data do not have to be archived. However, online models have not yet been subject to the same rigorous testing as offline models and they are computationally much more expensive.

In Europe alone there are at least 18 different mesoscale model families and 47 different transport or transport and chemistry models, 10 of which are online (Schlunzen & Sokhi, 2006). An evaluation of four mesoscale models by (Hanna & Yang, 2001) found the root mean squared error (RMSE) on the hourly averaged wind speed compared to observations was $2 - 3$ ms^{-1} with a wind direction RMSE of 50 degrees due to random turbulent processes and surface heterogeneity. Predicted mixed layer depths were within 20% of observations but had weaker temperature inversions. It was also found that the models underestimated the vertical temperature gradient in the first 100m at night. These differences in the meteorological fields could have a large impact on air quality forecasts.

The same meteorological data can lead to different air quality forecasts. Stern et al. (2008) found that forecasts of particulate matter concentrations over Europe varied dramatically depending on which air quality model is used as each model has internal methods to calculate its mixing parameters. It was found by Zanis et al., 2011 that the RegCM3/CAMx model driven with ERA-40 reanalysis data reproduces more accurately the observed ozone trend in Italy than the meteorological fields from ECHAM5. However, reanalysis products have very low temporal resolution and cannot be used for forecasting. This study also found that the CTM performs better in the day-time than at night in all seasons. It is speculated this is due to greater atmospheric stability in winter and enhanced vertical mixing in the summer.

Further studies have shown that the CTMs are sensitive to wind fields in complex terrain. The COSMO-IT model performed better in flat terrain than mountainous regions, where valley winds overestimated and wind direction prediction was poor (Schlunzen & Sokhi, 2006). Svensson (1996) also found her coupled model was sensitive to the terrain. Topography can also effect wind direction.

In summary, the meteorological input data for offline CTM has important consequences for the prediction of air quality. There have been many studies that assess the impact of data from different meteorological models on different CTMs. It has been found, as expected, that wind speed and direction, stability and mixing height are important in factors in predicting correct pollutant concentrations. This suggests the newly available

online models will also be affected by the forecast accuracy of these fields. In particular boundary-layer mixing which is parameterised in online meteorological CTMs.

1.3.2   Air quality forecasting in the UK

In the UK daily forecasts of pollutant concentrations are produced by the Department for Environment, Food and Rural Affairs (DEFRA). These forecasts are released at 1600 UTC and are valid for 24 hours. Forecasts are issued using an index which ranges from 1–10. This index, know as the Daily Air Quality Index (DAQI), is split into four bands as suggested by the Committee on Medical Effects of Air Pollutants (COMEAP). An index of 1–3 represents low concentrations, 4–6 moderate concentrations, 7–9 high concentrations and 10 represents very high concentrations. The overall index for a region or site is determined by the highest index of the following five pollutants: nitrogen dioxide, sulphur dioxide, ozone, PM10 and PM2.5. The air quality forecasts produced by DEFRA are validated using observations taken by the Automatic Urban and Rural Network (AURN) which monitors various pollutants at 127 sites across the UK.

There are many inputs into the DEFRA air quality forecasts. The main inputs are weather forecasts from the Weather Research Forecast (WRF) model which is used as an input to the CMAQ model plus HYbrid Single-Particle Lagrangian Integrated Trajectory (HYS-PLIT) back trajectories. Other sources of information used to inform UK forecasts are European and global air quality forecasts produced by other organisations, near real-time pollutant concentration observations from the UK and across Europe and satellite imagery. Forecasts of European air quality are also produced routinely by the Monitoring Atmospheric Composition and Climate (MACC) project. This project combines atmospheric modelling and earth observation to provide information on European air quality, global atmospheric composition and climate. Another project working in this area is the UK Chemistry and Aerosol project (UKCA) which aims to develop a coupled aerosol-chemistry-climate model based on the UK Met Office Unified Model.

1.4   The importance of the atmospheric boundary layer and its parameterisation

As the majority of the anthropogenic pollution is released at or near the surface and therefore the meteorological processes near the surface in the atmospheric boundary

layer play an important role in the distribution of pollutants.

A schematic of the classical diurnal evolution of a boundary layer is shown in Figure 1.2. This evolution is driven by surface heating which starts after sunrise. This heating results in convective plumes forming and rising vertically. These plumes mix properties of the boundary layer to form a well-mixed layer. The vertical extent of the plumes is dependent on the temperature inversion which separates the boundary layer from the free troposphere above until they have enough energy to penetrate the layer above. As these overshooting plumes descend back into the boundary layer they entrain air from above into the boundary layer. It is the interface between the boundary layer and the free troposphere that limits the vertical extent of boundary layer clouds. When the sun sets the source of surface heating is removed and the surface cools and a stable nocturnal boundary layer forms. Several studies (Gimson, 1997; Donnell et al., 2001; Kowol-Santen et al., 2001; Agusti-Panareda et al., 2005; Dacre et al., 2007; Sinclair et al., 2008) have found that boundary-layer mixing, along with convection and advection by synoptic scale motions, can impact the ventilation of pollutants out of the boundary layer which in turn impacts the vertical distribution of pollutants and, importantly, the surface concentrations.
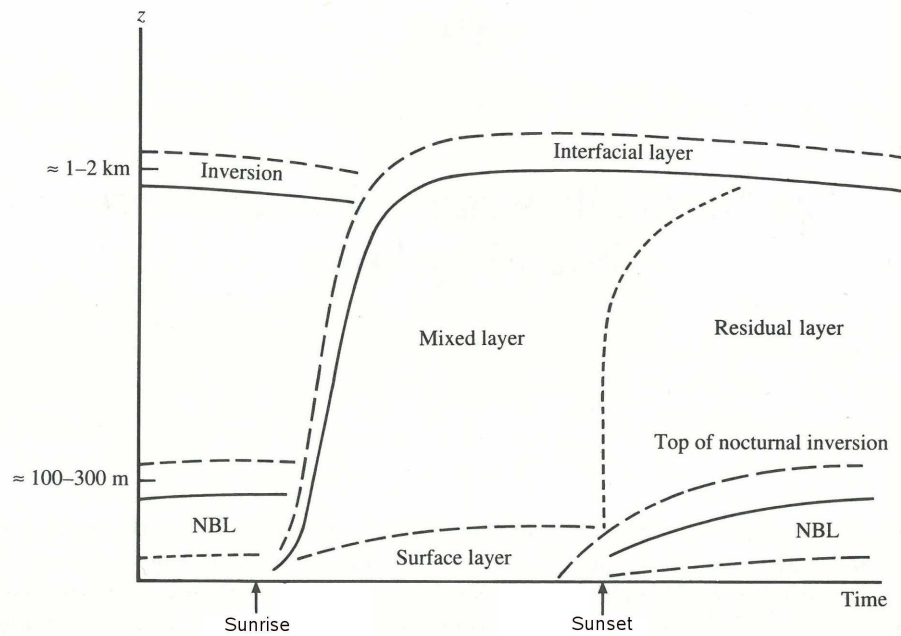
Figure 1.2: The structure of the boundary layer during a typical diurnal cycle, showing different layers present according to atmospheric stability and time of day. Following Stull (1988).

1.4.1   Clouds

Cloud is common in the boundary layer and predicting this cloud correctly has implications for air quality forecasting, numerical weather prediction and climate modelling. This is because clouds interact with longwave radiation, by trapping it close to the Earth's surface, and incoming shortwave radiation, by reflecting it back to space. They therefore contribute to the Earth's radiation budget and form an important component of the climate feedback system (Bony et al., 2006). A further study by Andrews et al. (2012) found that cloud radiative feedback was the largest single cause of interannual variability in the experiments performed for the third and fifth phases of the Coupled Model Intercomparison project (CMIP3 and CMIP5). On a regional level, mixed phase clouds in the Arctic can influence the rates of melting and freezing of the Arctic Ocean and therefore the transition into and out of winter (Jiang et al., 2000).

Boundary-layer clouds are very difficult to model and this is reflected by widely varying climatologies in climate models. In a comparison between ten climate models and satellite observations by Zhang et al. (2005) it was found that, the models under predict low-top cumulus and stratocumulus cloud (Figure 1.3 panels (g) - (h)). The largest under prediction is of the order of 90%. Although cumulus and stratocumulus are under predicted, stratus clouds are over predicted in all but one of the models considered in the study (Figure 1.3 panel i). Figure 1.3 also shows the models considered systematically over predict clouds associated with deep convection (panel (c)) but under predict mid-level altocumulus and altostratus clouds (panels (d) and (e)). These differences in modelled cloud distribution gives uncertainty in the radiative feedbacks of the models and thus make it one of the largest sources of uncertainty in climate prediction (Webb et al., 2006). Bony & Dufresne (2005) have shown that the climate models that predict the most global warming are the ones that also forecast the largest decrease in boundary-layer cloud occurrence in response to increased carbon dioxide. Dai & Trenberth (2004) found that low clouds (those below 700mb) are the main contributor to diurnal variations in cloud amount in the Community Climate System Model (CCSM2), especially in marine stratocumulus regions.

The clouds in weather forecast models have also been evaluated against ground-based radar observations (e.g. Illingworth et al., 2007; Barrett et al., 2009). On these shorter time scales, the prediction of cloud cover impacts the end users of weather forecasts as the presence of cloud impacts surface temperature, precipitation and ultraviolet radiation.
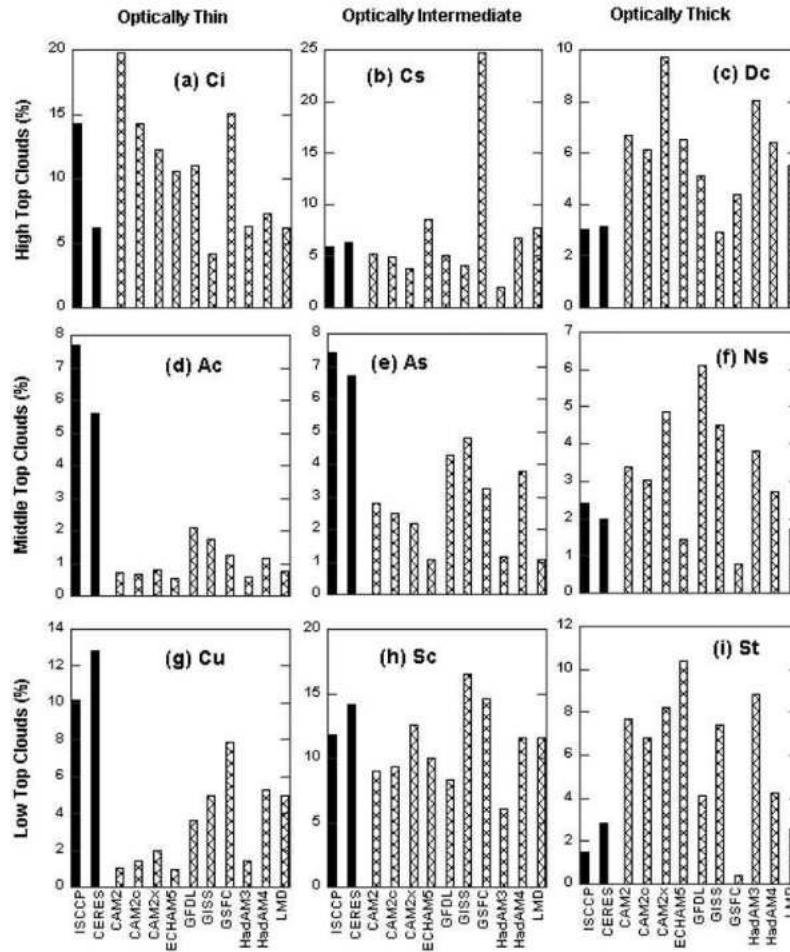
Figure 1.3: Cloud frequency averaged from 60°N to 60°S for December to February season for the nine ISCCP cloud types from satellite measurements and ten climate models (from Zhang et al., 2005. Note the low frequency with which low cumulus clouds are modelled (panel g) and high frequency of stratus clouds compared to satellite measurements in panel i.

Figure 1.4 shows the frequency of occurrence of clouds with cloud fraction, f, greater than four thresholds as a function of height for seven models and corresponding observations for 2003 and 2004 at three Cloudnet sites (Chilbolton, UK, Cabauw, Netherlands and Palaiseau, France) as calculated by Hogan et al. (2009b). Each model has different strengths and weaknesses but for boundary-layer cloud (3 km and below) it can be seen there is a large spread in the frequency of occurrence for all cloud fraction thresholds considered. When evaluating the skill of predicting the correct boundary-layer cloud at the correct time it was found that the UK Met Office Mesoscale model had the highest skill score. This result is supported by the study of Barrett et al. (2009) which found that the Met Office Mesoscale and Global models had the highest skill of forecasting the presence of boundary layer cloud.

Clouds also have an impact on the vertical mixing within the boundary layer. Observa-

tions have shown that top-down driven turbulence is present in stratocumulus cloud (e.g. Albrecht et al., 1995). This is due to longwave cooling at cloud top that generates negatively buoyant plumes that enhance vertical mixing. This mixing can be strong enough to reach the surface. Cumulus clouds can also effect the vertical mixing. Williams et al. (2011) found robust signatures of enhanced venting and sub-cloud-layer mixing when active cumulus clouds are present in vertical profiles radon. Other studies using remote sensing instruments have found distinct signals in vertical velocity skewness and variance associated with the presence of different cloud types (e.g. Hogan et al., 2009a). Thus it is important that the cloud type that is present is taken into account when considering the effect of boundary layer parameterisation on air quality forecasts.

1.4.2 The parameterisation of the boundary layer in numerical weather prediction and climate models

Mixing within the boundary layer is highly turbulent and occurs on short time scales (order minutes) and length scales (order metres) compared to those resolved in numerical weather prediction and climate models. Therefore in numerical weather prediction and climate models its effects on the resolved flow are parameterised . There are many different parameterisation schemes in use and a selection of these are outlined below. Particular attention is given to the boundary layer scheme used in the UK Met Office Unified Model (UM) as this scheme is studied in this thesis. This scheme is outlined in Section 1.5. It is evaluated in Chapter 3 and modifications to it are considered in Chapter 4.

Example parameterisations

Due to the turbulent nature of the mixing within the boundary layer it is not possible to derive a closed set of equations for the evolution of a grid box mean of a quantity in a numerical prediction or climate model. This is known as the turbulence closure problem. One way this problem can be overcome is to retain terms up to a certain order and approximate the remaining terms. In this section various different closure schemes will be outlined.

First-order schemes, also known as gradient transport theory or K-theory schemes, retain prognostic equations for only the mean variables, for example horizontal wind, temperature and humidity and approximate higher order covariances (e.g. Louis, 1979;
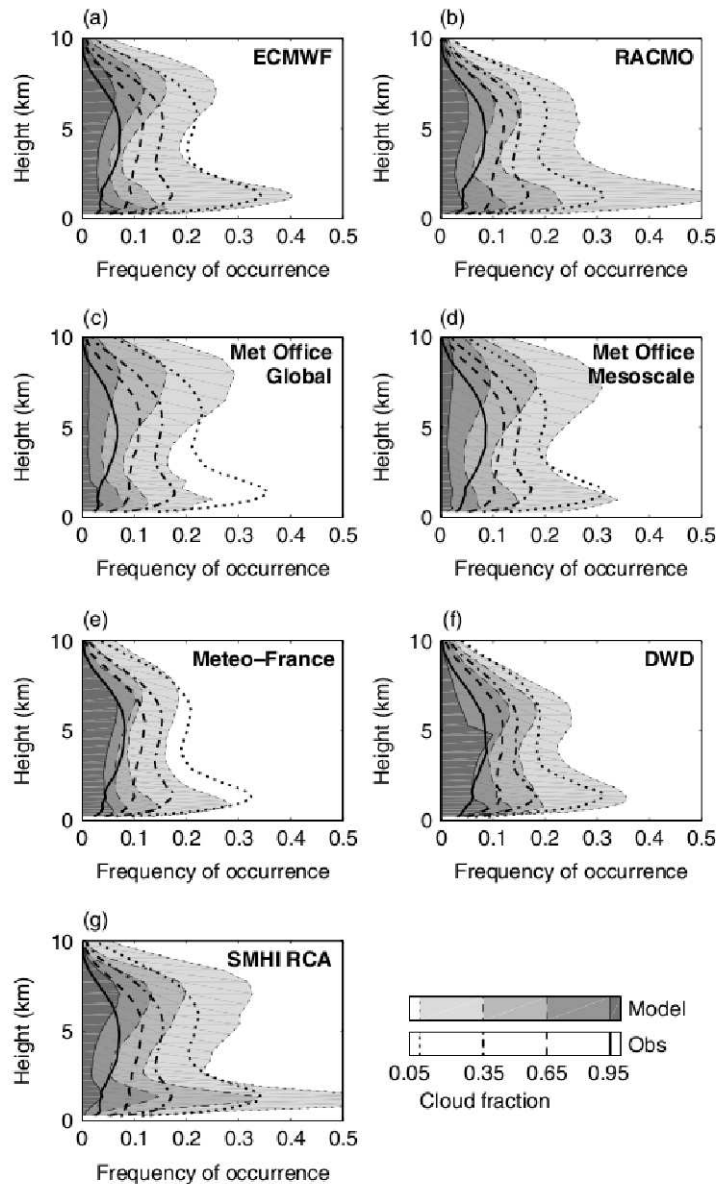
Figure 1.4: Frequency of occurrence of clouds fraction, f, greater than four thresholds for seven models (thin lines and shading), versus height, over Chilbolton, Cabauw and Palaiseau in 2003 and 2004. The corresponding observations are shown by the thick lines. Taken from Hogan et al. (2009b).

Troen & Mahrt, 1986; Hong et al., 2006). They use local (nearby) flux-gradient relationships to transfer the problem of unknown covariances to that of specifying an eddy diffusivity which is often specified from vertical shear, static stability and an appropriate length scale. This method is not suggested for use in convective mixed layers where gradients of mean quantities are zero but it is computationally inexpensive and still used in many operational models (e.g. Meteo-France). This technique does not account for entrainment.

Second-order schemes were developed alongside the development of computer power

and were motivated by the hope that "if a crude assumption for nth moments predicts $(n-1)$th moments adequately, perhaps a similar assumption for $(n+1)$th moments will predict nth moments just as well" (Stull, 1988). Second-order closure requires predictive equations for all the covariance terms (e.g. $\overline{u'w'}$, $\overline{w'\theta'}$ and $\overline{u'q'}$). The equations that need to be solved to obtain these terms are complex and contain triple correlation terms. There are many ways to parameterise these terms but most are based on mixing length theory or Monin-Obukhov similarity theory (e.g Lumley & Khajeh-Nouri, 1974; Mellor & Yamada, 1974; Wichmann & Schaller, 1986; Wyngaard, 1990). A comparison of a second-order simulation to observations taken during the Wangara experiment (Yamada & Mellor, 1975) found that the scheme reproduced the general evolution of the boundary layer but had discrepancies in the profile of potential temperature in the convective regime. Third-order schemes have also been developed (e.g. Bougeault & André, 1986) and it has been shown that these models give better results due to their more accurate treatment of vertical fluxes of second-order moments (Zeman & Lumley, 1976; André et al., 1978). However this improved representation comes at great computational expense.

The other schemes described in this section have been developed to perform better than local schemes in convective and/or cloudy situations. Schemes that use the turbulent kinetic energy (TKE) equation in place of velocity variance equations are known as 1.5 order or TKE closure schemes (e.g. Mellor & Yamada, 1982). This type of scheme creates nearly well mixed layers during the daytime but requires a prognostic variable for TKE and is much more computationally expensive.

Non-local closure schemes recognise that in convectively unstable situations larger eddies can transport fluid across finite distances before the smaller eddies have time to cause mixing and therefore relate unknown variables to known variables at any number of other vertical grid points. The simplest version of this type of scheme is a mixed layer model (e.g. Carson, 1973) which assume that potential temperature is constant throughout the depth of the boundary layer and the surface is horizontally homogeneous. Mixed layer schemes are computationally efficient and are used in some ocean models.

Penetrative convection or Blackadar schemes are based on the assumption that boundary-layer heat exchange takes place between the ground surface and each level within the mixed layer. This scheme naturally produces counter gradient terms. Non-local diffusion methods (e.g. Troen & Mahrt, 1986; Holtslag & Boville, 1993; Hong & Pan, 1996) are based on results from large-eddy simulations and explicitly include a non-local

term in the diffusion equation. The Hong & Pan (1996) scheme performed better at simulating observations from the first international satellite land surface climatology project (ISLSP) field experiment than a local scheme. Another novel non-local scheme is the transilient turbulence scheme (Stull, 1988). This formulation is based on a discrete view of non-local mixing that occurs within the boundary layer and allows for a range of eddy sizes to influence the turbulent mixing.

The traditional K-closure approach has been extended by combining it with an advective mass-flux scheme which is used to treat strongly skewed local updrafts (Siebesma & Teixeira, 2000; Siebesma et al., 2007; Soares et al., 2004). This enables a unified parameterisation of turbulent transport in the cloud-topped boundary layer. This approach is currently used in the ECMWF medium-range weather prediction model (Kohler et al., 2011). The asymmetric convective model (ACM) is a parameterisation which prescribes convective transport originating in the lowest model layer and rising to all other layers in the convective boundary layer with symmetrical return flow from each layer back to the lowest layer. This has been further modified in the ACM2 scheme (Pleim, 2007) which has an asymmetrical layer-by-layer downward transport. It also has an added eddy diffusion component to the non-local transport term. This better simulates the vertical profiles as local and non-local mass fluxes are explicitly defined via a transilient matrix. The ACM2 scheme is available for use in the MM5 and WRF models.

Spectral closure methods also exist (e.g. Sukoriansky et al., 2005). In this type of scheme the diffusivity coefficients are derived using their spectral space representation. A subset of this type of parameterisation uses an quasi-normal scale elimination (QNSE) algorithm which maps the the velocity and temperature fields in a quasi-Gaussian way using the Langevin equations (Sukoriansky et al., 2006). The scheme (Lock et al., 2000) used in the Met Office Unified model uses a combination of first order closure and non-local mixing schemes (see Section 1.5 for a full description of this scheme).

The impact of boundary-layer parameterisations

Extensive work has been done to test the impact of different boundary-layer formulations and it has been found that the scheme chosen can effect the timing and location of deep convection, the forecasting of tornadoes (Stensrud & Weiss, 2002; Hong et al., 2006), flash flood forecasting (Zampieri et al., 2005), the development of hurricanes (Powell, 1980; Nolan et al., 2009) and the climatology of the East Asian Monsoon (Hong, 2010).

A study by Hu et al. (2010) found that the main differences between the Mellor-Yamada-Janjic (MYJ), Yonsei University (YSU) and ACM2 schemes in the Weather Research and Forecast (WRF) model were the strength of vertical mixing and entrainment of air from above the boundary layer. The choice of scheme also impacts the the peak surface temperature by up to 2 K and day-time wind speed by up to 2 ms^{-1}. Zhang & Zheng (2004) found that the five schemes they tested in the MM5 model all correctly predicted the phase of the diurnal temperature variation but with different amplitudes (up to 4 K during the day). When considering day-time wind speed it was found it was generally underestimated by 2 ms^{-1} at the surface increasing to 3 ms^{-1} at 1 km. At night the low level jet strength is overestimated by up to 2 ms^{-1}. A more recent study by Shin & Hong (2011) compared five different schemes in WRF against CASES-99 data found that the predicted surface temperature has a spread of 5 K during the day but converge to be within 1 K at night with a large (5 K) positive bias. Conversely the wind components diverge, by up to 2 ms^{-1}, at night. The daytime divergence in thermodynamic variables was also found by Alapaty et al. (1997), with the largest differences observed during the growth of the mixed layer.

The GEWEX (Global Energy and Water cycle EXperiment) Atmospheric Boundary Layer Study (GABLS) has resulted in a number of single column model and LES intercomparison studies (Cuxart et al., 2006; Beare et al., 2006; Svensson et al., 2011; **?**) focussed on the boundary layer. These inter-comparisons have highlighted the importance of the boundary layer parameterisation on surface temperature and winds. In general modelled surface temperature has a larger diurnal cycle amplitude than observations. This difference is partly due to to modelled night-time surface temperatures being under-predicted, by up to 6 K in some instances. These low level temperature differences are related to differences in low-level stability which affects the turbulence and turbulent heat fluxes. The diurnal cycle in modelled wind speeds is too weak, by up to 2 ms^{-1}. All the models used in the GABLS3 inter-comparison predicted a low-level jet however all of the models analysed under predicted the jet strength. The maximum underprediction was 5 ms^{-1}. The parameterisation scheme chosen also has an impact on the growth and vertical structure of boundary layer. Night-time boundary-layer depths can be overpredicted by more than a factor of 2 which has consequences for turbulent mixing. During the day the differences tend to be smaller although there is still a large spread (up to 500 m in GABLS2 (Svensson et al., 2011).

A major factor in predicting the correct growth, diurnal cycle and cloud evolution is

the inclusion of a non-local mixing scheme and entrainment. A study using the second version of the NCAR Community Climate Model (CCM2) by Holtslag & Boville (1993) found that the non-local scheme they used transported moisture away from the surface more rapidly than the local scheme. The local scheme tended to saturate at the lowest model level unrealistically which leads to clouds too low in the atmosphere. Barrett et al. (2009) found that the best diurnal evolution of a stratocumulus topped boundary layer was given by models that included a non-local mixing scheme. Shin & Hong (2011) found that non-local schemes with entrainment are favourable in unstable conditions; however, they found local TKE closure schemes showed better performance at night.

In this section the impact of boundary-layer parameterisation in models has been discussed. The choice of boundary-layer parameterisation can have a large impact on the diurnal cycle meteorological fields, such as temperature, wind speed and mixing height, as well as forecasting extreme events. In turn these differences would have an impact on the dispersion of pollutants in a CTM and therefore air quality forecasts. To achieve the best possible air quality forecast the best boundary-layer parameterisation must be used.

1.5   The Met Office boundary-layer parameterisation scheme

In this section the key features of the boundary-layer parameterisation scheme implemented in the Met Office Unified Model is described. This model is focussed on as it is this boundary-layer scheme that will be evaluated in Chapter 3 using the algorithm developed in Chapter 2. A full description of the scheme can be found in Lock et al. (2000), Lock (2001) and Lock & Edwards (2011).

In the Met Office Unified Model (UM) parameterisation scheme, the boundary layer is divided into seven different categories (referred to as types) depending on the surface stability and capping cloud. Six of the seven types are depicted in Figure 1.5. The seventh type is known as *shear dominated unstable layer* and is diagnosed when wind-shear might allow deeper turbulent mixing in unstable boundary layers than is apparent purely from the thermodynamic profiles. This enhanced mixing may even be sufficient to inhibit the formulation of cumulus cloud.

The first decision made in the diagnosis of the boundary-layer type in the UM is the determination of the surface stability. This is based on the surface buoyancy flux F_B.
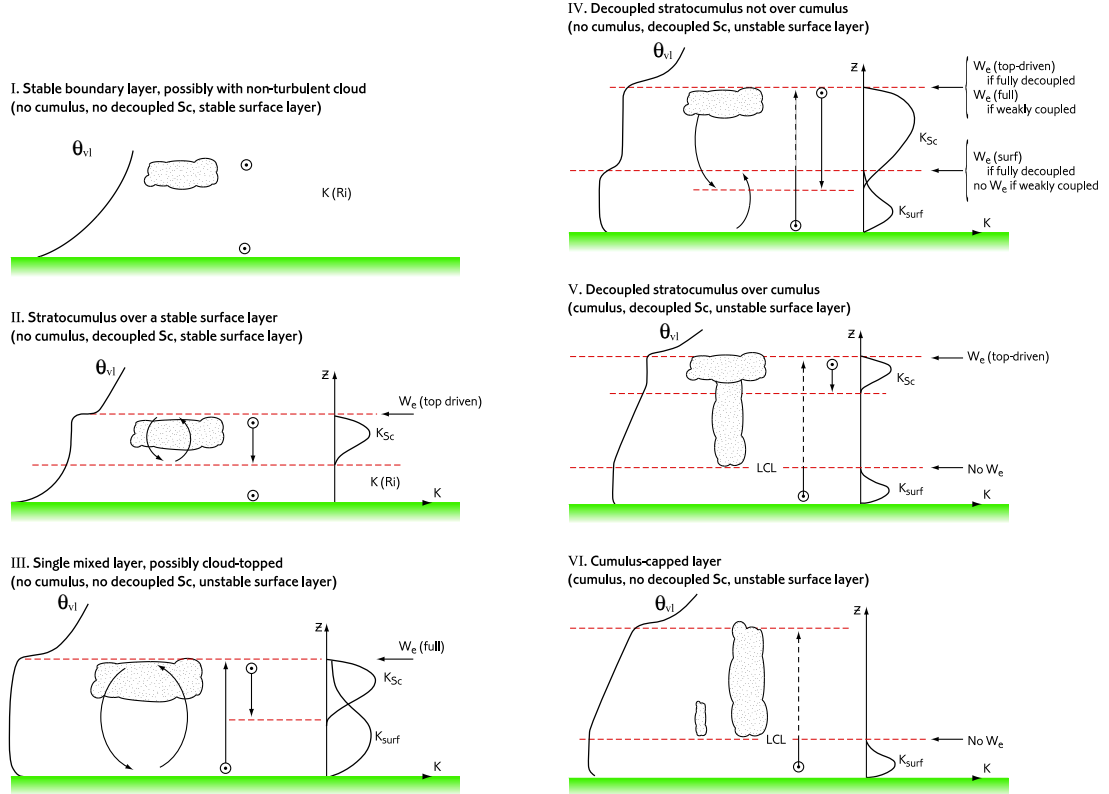
Figure 1.5: Schematic representing boundary-layer types I to VI, from Lock et al. (2000). Arrow tops denote the extent of the surface parcel ascent (z_{par}), whilst their solid line portion indicates the diagnosed boundary-layer top (z_h). Downward arrows indicate the extent of cloud-top driven turbulence (z_{ml}). w_e shows where the explicit entrainment parameterisation is applied and $K(Ri)$, K^{surf} and K^{sc} show where each eddy diffusivity parameterisation is used. See text for further details.

Where unstable layers are found ($F_B > 0$), a moist parcel ascent is used to calculate the level of neutral buoyancy for surface based thermals (z_{par}). If the layer is well-mixed (i.e. cloud-free or stratocumulus capped), the boundary-layer top, z_h, is defined as the top of the parcel ascent, z_{par}. However, if cumulus convection is present, the boundary-layer scheme is capped at the cumulus cloud base (z_h = lifting condensation level (LCL)). In stable layers ($F_B < 0$), z_h is defined where the bulk Richardson number (Equation 1.7) first becomes greater than one.

First-order K-closure is used to parameterise the turbulent fluxes in terms of local gradients and eddy diffusivities with non-local terms included which act only in unstable boundary layers:

$$\overline{\chi'w'} = -K_\chi \frac{\partial \chi}{\partial z} + K_\chi^{surf} \gamma_\chi, \tag{1.1}$$

where χ is a conserved scalar variable and γ_χ is the non-local counter gradient term

which is included to maintain more well mixed potential temperature profiles. This follows earlier work by many including **?**Holtslag & Moeng (1991); Holtslag & Boville (1993).

Local turbulent eddy diffusivities

The eddy diffusivities for momentum, K_m, and scalars, K_h, are given in terms of neutral mixing lengths, $\mathcal{L}_m^2$ and $\mathcal{L}_h^2$, which are defined as the typical vertical depth over which air parcels move before mixing with their surroundings:

$$K_m = \mathcal{L}_m^2 \left| \frac{\partial \mathbf{u}}{\partial z} \right| f_m(Ri) \tag{1.2}$$

$$K_h = \mathcal{L}_h \mathcal{L}_m \left| \frac{\partial \mathbf{u}}{\partial z} \right| f_h(Ri). \tag{1.3}$$

Here $\mathcal{L}_m$ and $\mathcal{L}_h$ are given by the following, which are based on those used by Blackadar (1962),

$$\mathcal{L}_m = \frac{k(z + z_{0m})}{1 + k(z + z_{0m})/\lambda_m} \tag{1.4}$$

$$\mathcal{L}_h = \frac{k(z + z_{0m})}{1 + k(z + z_{0m})/\lambda_h} \tag{1.5}$$

where k is the von Karman constant (equal to 0.4) and z_{0m} is the roughness length for momentum including the orographic component. This formulation allows the mixing length to vary smoothly between kz in the surface layer and the asymptotic mixing length, $\lambda_{m,h}$, in the rest of the boundary layer.

It is assumed that the vertical extent of the boundary layer limits this length scale and in this scheme it is limited by the asymptotic mixing lengths, $\lambda_{m,h}$, given by

$$\lambda_{m,h} = \max[40 \text{ m}, 0.15 z_h]. \tag{1.6}$$

.

Some other schemes use constant asymptotic lengths ranging from 30 m (Global Forecasting System: Holtslag & Boville, 1993; Hong & Pan, 1996) to 150 m (ECMWF: http://www.ecmwf.int/research/ifsdocs/CY28r1/Physics/Physics-04-04.html). Assuming a maximum model boundary-layer depth of 2 km, the possible values of $\lambda_{m,h}$ in the Met Office scheme encompasses the values used by these other schemes. In the pre-

vious Met Office scheme (Smith, 1990) the asymptotic mixing lengths were proportional to the boundary layer height and had no lower limit. The Meteo-France model uses the Bougeault & Lacarrere (1989) mixing length formulation that is determined form the potential upwards and downward displacements that parcels with the kinetic energy equal to the turbulent kinetic energy at a specific accomplish before being stopped by buoyancy effects.

$f_{m,h}(Ri)$ are the stability functions dependent on Richardson number. Richardson number is a local measure of stability and is defined as

$$Ri = \frac{\Delta B / \Delta z}{(\Delta \mathbf{u} / \Delta z)^2} \tag{1.7}$$

where ΔB is buoyancy production ($B = \frac{g \Delta \overline{\theta}}{\theta \Delta z}$).

In stable conditions when Ri is greater than zero and boundary-layer type I or II is diagnosed, the 'long-tailed' functions are used:

$$f_{m,h} = \frac{1}{1 + 10 Ri}. \tag{1.8}$$

This function is determined by empirically fitting to experimental data. Similar functions are used in the ECMWF and GFS models. Note that in stable conditions the non-local term is not applied.

Non-local turbulent eddy diffusivities

When an unstable layer (types III–VII) is diagnosed the local mixing scheme does not always produce enough mixing as in reality surface based thermals which are positively buoyant rise throughout the depth of the boundary layer. This means the turbulent fluxes are dependent more on the surface characteristics and depth of these large eddies, than the local Richardson number. The eddy diffusivities are calculated in the following way which is based on that proposed by Holtslag & Moeng (1991) adjusted to ensure it matches the entrainment diffusivity at the boundary-layer top:

$$K_m^{surf} = k(u_*^3 + w_s^3)^{1/3} z \left(1 - \mathcal{E}^{\int \sqcap \nabla \{} \frac{z}{z_h} \right)^2 \tag{1.9}$$

$$K_h^{surf} = K_m^{surf} / Pr, \tag{1.10}$$

where u_* is the friction velocity. $\mathcal{E}^{\int \sqcap \nabla \{}$ is a factor to ensure that the diffusivities tend to

the entrainment eddy diffusivities as z tends to z_h, and Pr is the turbulent Prandtl number, defined as the ratio of the eddy diffusivities for momentum and heat (K_m^{surf}/K_h^{surf}). w_s is a vertical velocity scaling, defined as

$$w_s^3 = \begin{cases} 2.5\frac{z}{z_h}w_*^3 & for\ z < 0.1z_h \\ 0.25w_*^3 & for\ z \geqslant 0.1z_h \end{cases}, \tag{1.11}$$

where $z < 0.1z_h$ is the definition of the surface layer and w_* is the convective velocity scale for a cloud-free convective boundary layer. In these unstable cases $Ri < 0$ and the stability functions given by

$$f_{m,h} = 1 - \frac{g_0 Ri}{1 + \mathcal{D}_{m,h}(\mathcal{L}_m/\mathcal{L}_h)|Ri|^{1/2}}, \tag{1.12}$$

where $g_0 = 10$, $\mathcal{D}_m = 2.5$ and $\mathcal{D}_h = 0.4$. As for the stable case, this function is derived by fitting to experimental data.

The boundary-layer type diagnosis is also dependent on the type of capping cloud that is present. If cumulus cloud is diagnosed, types V or VI, then the boundary-layer scheme is capped at the cumulus cloud base and the convection within the cloud is treated entirely by the convection scheme. Stratocumulus-capped boundary layers have turbulence driven from the cloud top downwards due to cloud-top radiative cooling in a similar manner to surface-driven turbulence in unstable boundary layers. Therefore this turbulence is parameterised in much the same way. Non-local stratocumulus eddy diffusivities, K_m^{sc} and K_h^{sc}, are defined as

$$K_m^{sc} = 0.63 k V_{sc} \frac{z'^2}{z_{ml}} \left(1 - \mathcal{E}^{\int \rfloor}\frac{z'}{z_{ml}}\right)^{0.8} \tag{1.13}$$

$$K_h^{sc} = K_m^{sc}/Pr, \tag{1.14}$$

where the superscript "sc" indicates that these eddy diffusivities are parameterising turbulent mixing driven from the stratocumulus cloud top. z' is the height above cloud base, z_{ml} is the cloud depth and V_{sc} is a scaling velocity. The shape of this profile was determined by fitting to large-eddy simulations of the stratocumulus-topped boundary layer.

The three components of diffusivity are combined in the following way:

$$K_h = \max[(K_h^{surf} + K_h^{Sc}), K_h(Ri)]. \tag{1.15}$$

This means that the local scheme provides the "minimum possible mixing" in unstable conditions.

Entrainment

The scheme contains an explicit entrainment parameterisation in terms of an entrainment velocity, w_e, as described by Lock (2001). Entrainment is the mechanism by which warm, dry air is carried from the free troposphere into the boundary layer by convective plumes that overshoot their level of neutral buoyancy. As this air sinks back into the mixed layer, it carries with it some of the warmer air from above. This appears as a heat-flux, $H|_{z_h}$, at the top of the boundary-layer. The descending air can also carry moisture and momentum from the troposphere into the boundary layer. For scalar variables, the entrainment fluxes are specified explicitly. It is assumed that the entrainment fluxes reduce from their maximum at $z = z_h$ to zero at $z = h$, a small distance above. The fluxes are then proportional to the change in a quantity between z_h and h:

$$H|_{z_h} = -w_e \Delta\theta + F_{\text{net}} \tag{1.16}$$

$$\overline{w'q'}|_{z_h} = -w_e \Delta q, \tag{1.17}$$

where F_{net} is the net radiation at z_h. Entrainment fluxes for momentum are specified through eddy-diffusivities:

$$K_h|_{z_h} = w_e \Delta z \tag{1.18}$$

$$K_m|_{z_h} = Pr K_h|_{z_h}, \tag{1.19}$$

where Δz is the distance between the two model theta-levels either side of z_h. Further details of the boundary-layer scheme can be found in Lock & Edwards (2011); this includes a detailed description of the surface layer parameterisation.

There are many aspects of this scheme that could be investigated. In this thesis the boundary-layer scheme will be evaluated by focussing on the when each of the types is diagnosed and therefore when each each of the mixing schemes is applied.

1.6 Observations of the atmospheric boundary layer

There are many ways to observe the turbulent atmospheric boundary layer. These include in-situ measurements made on towers, tethered balloons and aircraft measure-

ments and measurements made by remote sensing devices such as lidars, radars and wind profilers. Remote sensing measurements have an advantage over in-situ measurements as they can simultaneously sample many heights in the atmosphere. In this thesis the instruments focussed on are the Doppler lidar and sonic anemometer. In the following sections these two instruments are described and their possible applications are discussed.

1.6.1   The Doppler lidar

A lidar is a remote sensing instrument that can give high spatial and temporal resolution measurements of the atmosphere. A lidar works using the same principles as a radar, transmitting a pulse of radiation and waiting for the return signal from targets in the atmosphere. Instead of using radiation in the radio part of the electromagnetic spectrum, as in radar, lidars use light. The exact wavelength used depends on the application, range required and the availability and affordability of a laser source at the wavelength required. The first use of using beams of light to observe the atmosphere was in pre-laser times and consisted of shining searchlight beams through a telescope to try and determine profiles of air density (Weitkamp, 2005). As early as 1938 pulses of light were used for the first time to measure cloud-base heights. There was rapid developments in lidar technology in the 1960s due to the invention of the laser. Since then lidar developments have been closely linked to the progress in optical and electronic technology.

The basic lidar setup consists of a transmitter and a receiver. The transmitter sends out a coherent pulse of light into the atmosphere. This light is scattered by particles in the atmosphere (e.g. aerosol or water droplets). As the wavelength is much shorter than the size of cloud particles the scattering follows Mie and geometric optics approximation. This scattered light is detected by the instrument receiver. The power received by the lidar, P_R, is given by

$$P_R = P_T \frac{C_{lidar}}{r^2} \beta(r,\lambda) \exp\left[-2\int_0^r \alpha(r,\lambda)dr\right],\qquad(1.20)$$

where P_T is the transmitted power, C_{lidar} is constant dependent on the lidar hardware such as the pulse length and area of the primary optics receiver, r is the range from the instrument, $\beta(r,\lambda)$ is the backscatter coefficient and λ is the wavelength of the lidar. The exponential term relates to the extinction of the lidar signal as it passes through the atmosphere (Weitkamp, 2005). It is a function of the range, r, and wavelength, λ, and is

quantified by the extinction coefficient, α, which is defined as

$$\alpha(r, \lambda) = \frac{1}{V} \sum_V \sigma_{ext}(\lambda), \tag{1.21}$$

where σ_{ext} is the extinction cross section of an individual particle. To be able to compare values of return power independent of the lidar hardware attenuated backscatter, β' is defined as

$$\beta'(r, \lambda) = \beta(r, \lambda) \exp\left[-2\eta \int_0^r \alpha(r, \lambda)dr\right], \tag{1.22}$$

where η is an additional term included to account for multiple scattering of the lidar beam, following Platt (1973). The units of attenuated backscatter are $sr^{-1}m^{-1}$.

The lidar used in this study is a heterodyne Doppler lidar with a wavelength of 1.5 μm. Doppler lidars were first developed in the 1970s to detect clear-air turbulence (Weaver et al., 1981). They detect the change in frequency of the backscattered radiation compared to the frequency of the radiation emitted. This difference is proportional to the relative speed between the target and receiver. A study by Abshire et al. (1974) found significant Doppler returns from snow and rain but it was not until the 1980s that a Doppler lidar was trialled on a NASA test aircraft (Menzies & Hardesty, 1989). Doppler lidar systems are now commercially available (e.g. Pearson et al., 2008). The heterodyne refers to the the detection technique used. The detected backscatter signal is mixed with radiation from a local optical oscillator which gives a high tolerance to background light and the independence of temperature and all properties of the optical components of the system (Werner, 2005). Despite the sophistication of these heteorodyne systems, and their need for fast detection devices and ultra-stable, high-power lasers, the cost of a Doppler lidar has dramatically decreased over the last 10 years. This is due to the availability of cheap components related to advances in telecommunications.

1.6.1.1   Uses of Doppler lidar

Lidars are useful for analysing the structure of the boundary layer due to their ability to sample at many levels throughout the lower atmosphere at a high temporal resolution (order seconds) and to record data over long time periods (order years). Due to the high temporal resolution of the lidar data it is possible to observe turbulent processes and the diurnal cycle of the boundary layer. Many studies have used ground-based and airborne lidars to diagnose boundary-layer depth (e.g. Pul et al., 1994; Steyn et al., 1999; Davis

et al., 2000; Mok & Rudowicz, 2004; Davies et al., 2007; Pearson et al., 2010; Barlow et al., 2011) and retrieve profiles of wind and temperature throughout the lower atmosphere (Newsom et al., 2005). Data from the Lidars-In-Flat-Terrain (LIFT) experiment (Cohn et al., 1998) have been used to determine the vertical velocity, and its higher order moments (variance, skewness and kurtosis) from Doppler lidar measurements (Lenschow et al., 2012). Lothon et al. (2006, 2009) used these data to calculate the integral scale and coherence of vertical velocity, turbulent kinetic energy dissipation rates, spectra and the ratio of surface sensible heat flux to entrainment heat flux. Furthermore a study by Hogan et al. (2009a) showed that vertical velocity skewness derived from Doppler lidar can be used to diagnose the source of turbulence (surface driven or cloud-top driven). These studies show that Doppler lidars are a tool that can be used to obtain long-term turbulence statistics throughout the depth of the boundary layer and thus be used for evaluation of model parameterisation schemes.

Other types of lidar have also been used to study the passage of fronts (e.g. Melfi et al., 1989) and hurricanes (e.g. Kovacs & McCormick, 2003), to monitor stratospheric ozone (e.g. Donovan et al., 1995) and to make measurements of planar ice crystals falling from supercooled layer clouds (Westbrook et al., 2010). Commercially available lidars are eye-safe and easily portable thus making it possible to site them in complex environments, such as cities (Barlow et al., 2011), rainforests (Pearson et al., 2010) and on satellites (e.g Stensrud & Weiss, 2002).

In this thesis observations from a ground-based Doppler lidar are used to diagnose hourly values of boundary-layer type. This is done by determining the boundary-layer depth, using a technique similar to that used by Flamant et al. (1997), the number of cloud layers present, vertical velocity skewness and variance.

1.6.2   The sonic anemometer

The sonic anemometer is a commercially available instrument which is the modern day equivalent of a small propeller type air meter and swinging plate anemometer and bi-vane attached to a recording pen that were used to measure turbulence in 1930 (Kaimal & Finnigan, 1994). The sonic anemometer as we know it is due to the advent of fast-response sensors and digital computing and was first used in the Kansas Experiment in 1968 (Haugen et al., 1971). It records in-situ high temporal resolution temperature (T), horizontal and vertical wind components (u, v and w), carbon dioxide and water vapour

concentration data. These data can be decomposed into a mean and turbulent part (e.g. for variable a, $a = \bar{a} + a'$ where $\bar{a}$ is the mean and a' is the turbulent contribution) as first proposed by Reynolds (1895). By definition the fluctuations average to zero ($\overline{a'} = 0$) but when two fluctuating quantities are multiplied together a covariance term remains. For example,

$$ab = \left(\bar{a} + a'\right)\left(\bar{b} + b'\right) = \bar{a}\bar{b} + \bar{a}b' + a'\bar{b} + a'b'. \tag{1.23}$$

When the average of ab is taken $\bar{a}b'$ and $a'\bar{b}$ average to zero so

$$\overline{ab} = \bar{a}\bar{b} + \overline{a'b'}. \tag{1.24}$$

The surface sensible heat flux, H, is the flux of energy transferred between the surface and adjacent air due to the temperature gradient between them and will be used in this thesis to determine the surface stability of the boundary layer. It can be derived using Reynolds decomposition in the following way:

$$
\begin{aligned}
H =\ & \rho C_p \overline{w\theta}, \\
=\ & \rho C_p \overline{\left(\bar{w} + w'\right)\left(\bar{\theta} + \theta'\right)}, \\
=\ & \rho C_p \overline{\left(\bar{w}\bar{\theta} + \bar{w}\theta' + w'\bar{\theta} + w'\theta'\right)},
\end{aligned}
$$

where ρ is the density of dry air (which is assumed to be constant) and C_p is the specific heat capacity of air. It is assumed that the mean vertical flow is negligible and thus the equation simplifies to

$$H = \rho C_p \overline{\left(w'\theta'\right)}. \tag{1.25}$$

Note that when using this technique all trends from the timeseries being used must be removed before calculating the turbulent component. The temperature timeseries used is the sonic temperature not the absolute temperature. The sonic temperature is sensed along the same path as the vertical velocity, w, and although it is affected by humidity fluctuations and normal wind components, these errors are negligible when temperature fluctuations are large. Absolute temperature can be measured by co-located fine-wire thermocouples or platinum resistance thermometers however these instruments are vulnerable to damage from wind, rain and flying debris and contamination of the sensing element can effect the systems time constant (Kaimal & Finnigan, 1994). Also, the averaging time must be chosen carefully; it must be long enough to sample the largest scales of the turbulence but also must satisfy the assumption of boundary layer station-

arity. Typical averaging times used are 30–60 minutes (Kaimal & Finnigan, 1994). This technique can be used to obtain fluxes, for example latent heat flux and momentum flux.

1.7 Thesis questions and outline

The original work in this thesis is split naturally into three chapters, Chapters 2–4. The subject matter of each chapter is fairly distinct and as such each chapter includes its own introduction section, a section reviewing previous work on the subject and a short discussion section. There is also a final discussion and future work chapter, Chapter 5.

1.7.1 Key scientific questions

There are four key scientific questions that this thesis sets out to answer.

1. How can boundary-layer type be diagnosed from remote sensing measurements? This question is addressed in the first work chapter, Chapter 2, where a novel method for diagnosing observational type using a Doppler lidar and a sonic anemometer is presented. Case study days are discussed to illustrate the new technique along with a three-year climatology of boundary layer type over Chilbolton in Hampshire. Also shown are the most common boundary-layer type diurnal transitions.

2. How well does the Met Office model compare with observations of observed boundary-layer type over Chilbolton? In Chapter 3 the observational boundary-layer type time series created in Chapter 2 is compared to the boundary-layer type forecast by the Met Office model. This is done climatologically, comparing two years of observations and model data, and using a skill score which assesses the model's ability to predict the correct boundary-layer type at the correct time. The boundary-layer type diagnosis can be split into five different decisions each relating to different processes occurring the boundary layer. The skill of each of these decisions is assessed using the Symmetric Extremal Dependence Index (SEDI) verification measure.

3. To what extent does the skill of a forecast of boundary-layer type vary with leadtime and model resolution? This question is also addressed in Chapter 3. It again uses the observationally diagnosed timeseries of boundary-layer type but this time assessing the

skill at forecast leadtimes from 0–36 hours for both the UK Met Office 4 km an 12 km models using the SEDI score.

4. To what extent does the diagnosis of boundary-layer type affect the vertical distribution of pollutants?   In the final work chapter, Chapter 4, the impact of diagnosing a certain boundary-layer type on the vertical distribution of pollutant is investigated. This is done using idealised single column model experiments to assess the effect of mixing associated with stratocumulus and cumulus cloud and entrainment. The impact of pollutant life time is also investigated.

Chapter 2

Can Doppler lidar be used to diagnose boundary-layer type?

This chapter introduces a new method of classifying the boundary layer into different types using Doppler lidar measurements. First the three case studies are presented. This is followed by a full description of the method. A climatology of boundary-layer type over Chilbolton, Hampshire is shown before considering the most common boundary-layer type transitions.

2.1   Introduction

Boundary-layer mixing is a highly turbulent, complex and continually evolving process. One method of understanding this evolution is to classify the boundary layer, at any given time, into a reduced set of types. Observationally the boundary layer is often classified subjectively using stability and the presence of convection (e.g. Clarke, 1970). These observational classifications, as well as being subjective, have previously only been applied over a short time period or on a case study basis. Examples of this include The Stable Atmospheric Boundary-Layer Experiment in Spain (SABLES 98, Cuxart et al., 2000) where two nocturnal periods were analysed, and the Cooperative Atmosphere-Surface Exchange Study (CASES-99, Poulos et al., 2002) where 30 days of data were analysed.

In weather forecast and climate models boundary-layer mixing is parameterised. In order to determine which mixing scheme to apply at a given time, the boundary layer can be classified into types. This classification may be used to determine whether a local or

non-local scheme is applied and whether to apply a cloud-top entrainment parameterisation, or whether to apply a shallow cumulus scheme. One such explicit classification scheme is the one currently used by the UK Met Office (Lock et al., 2000), but most other schemes contain several switches that combine to give a similar result. A long-term observational dataset of boundary-layer type would enable model parameterisations to be rigorously evaluated. It could be used to investigate the impact of cloud presence and distribution on how the state of the boundary layer can affect the transport of moisture and tracer.

Remote sensing techniques, in particular lidar, are very useful for analysing the structure of the boundary layer due to their ability to sample at many levels throughout the lower atmosphere and to record data over long time periods. As such, numerous previous studies have used ground-based and airborne lidars to diagnose boundary-layer depth (e.g. Steyn et al., 1999; Davis et al., 2000; Mok & Rudowicz, 2004; Davies et al., 2007; Pearson et al., 2010; Barlow et al., 2011), determine the vertical velocity, and its higher order moments from Doppler lidar measurements (Lothon et al., 2009; Lenschow et al., 2012) and retrieve profiles of wind and temperature throughout the lower atmosphere (Newsom et al., 2005).

In this chapter it is demonstrated how quantities derived from a continuously operating, vertically pointing Doppler lidar, specifically the backscatter coefficient, the vertical velocity skewness and the vertical velocity variance, combined with surface flux measurements from a sonic anemometer, can be used to classify the boundary layer into types similar to those outlined in Lock et al. (2000). Finally a three-year climatological study of boundary-layer type is presented using data from the Chilbolton Atmospheric Observatory in Southern England.

The Chapter is organised as follows. In Section 2.2 the new method of deriving boundary-layer type from Doppler lidar and sonic anemometer is described. Also in Section 2.2, case studies are presented to demonstrate the performance of the method for a cumulus-topped boundary layer, a stratocumulus-topped boundary layer plus a more complex case representative of a day that does not follow the classical evolution of the boundary layer. In Section 2.3, the three-year study of boundary-layer types is presented before the most probable boundary-layer type transition sequences are discussed. The code used to produce the following analysis is available at www.met.reading.ac.uk/ py904867/research/BL_type_diagnosis.html.

2.2 Method and case studies

The algorithm presented here classifies the boundary layer into nine types using observations from a Doppler lidar, in a vertically pointing configuration, and a sonic anemometer. The nine types diagnosed in the algorithm are based on the six types described in Lock et al. (2000) with their type I (stable) split into three types (Ia, Ib and Ic) and their type III (well mixed) split into two types (IIIa and IIIb), based on the presence of cloud and the number of cloud layers present. Figure 2.1 is a conceptual depiction of the nine boundary-layer types that are diagnosed here. It summarises the stability of the surface layer, the cloud type, where turbulence is being driven from (surface or cloud top), the depth of penetration of cloud-top driven turbulence and the number of cloud layers for each boundary-layer type.

The distinction between type IIIa (well mixed) and IIIb (stratocumulus-capped) is justified since many numerical weather prediction models, including the Met Office Unified Model, effectively distinguish between them by applying a cloud-top entrainment scheme only when cloud is present. Types Ia and Ib are the stable analogues of types IIIa and IIIb. Type Ic (forced cumulus under stratocumulus) is a type not considered in the Met Office scheme. It is a case where a decoupled layer of stratocumulus is present with a layer of cloud beneath. It is assumed that the lower level cloud was once surface-driven cumulus, but now the surface layer is stable. This type is most naturally grouped with type II but the Met Office scheme would most likely treat this as type I so here it is classed as a subset of type I to facilitate the model evaluation presented in Chapter 3.

2.2.1 Instrumentation and variables

The instruments used in this study are located at the Chilbolton Facility for Atmospheric and Radio Research (CFARR) in southern England (51°09′N, 01° 26′W). The lidar used is a HALO photonics 1.5 μm heterodyne Doppler lidar (Pearson et al., 2008) which records vertical profiles of attenuated backscatter coefficient, β, and Doppler velocity, w, once a minute and is sensitive to both cloud and aerosol. The lidar has a range-gate spacing of 36 m.

There are many different definitions of boundary-layer depth and methods to determine it using remote sensing instruments in the literature (Endlich et al., 1979; Flamant et al., 1997; Steyn et al., 1999; Seibert et al., 2000; Davis et al., 2000; Hennemuth & Lammert,
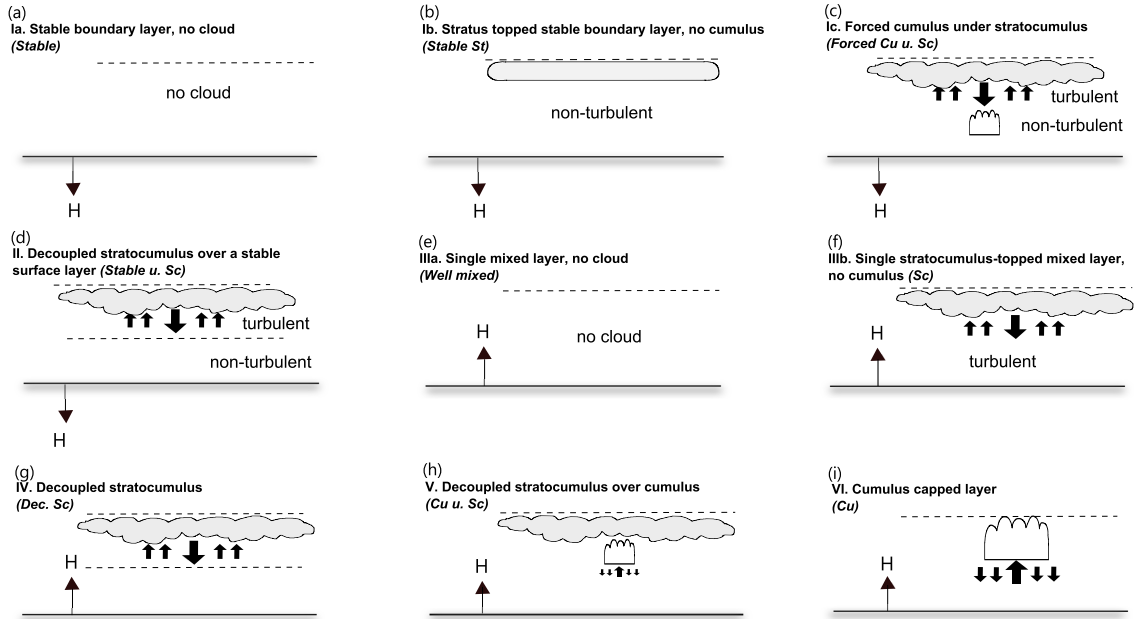
Figure 2.1: Conceptual representation of the nine boundary-layer types. The upper dashed line indicates the top of the aerosol layer. The direction of the large thick black arrow indicates whether the cloud-base turbulence is being driven from either the surface (upward-pointing arrow) leading to positive vertical-velocity skewness or cloud top (downward-pointing arrow) leading to negative skewness. The lower dashed lines represent the depth to which turbulence driven by cloud top cooling reaches (for types II and IV only). The direction of the narrow arrow labelled H indicates the sign of the sensible heat flux and the stability of the surface layer. The text in brackets are shortened descriptions of the boundary-layer types used in later figures and tables.

2006; Davies et al., 2007; Emeis et al., 2008). Here the boundary layer depth is determined using the attenuated backscatter coefficient. It is defined as the lowest height at which 80% of the lidar profiles within an hour have no detectable backscatter; this is similar to the gradient method for determining boundary-layer height (e.g. Flamant et al., 1997). This method has been used over other more sophisticated methods as only an hour-mean value is required. Note that as the lidar is sensitive to aerosol this definition actually estimates the aerosol depth, h_{aer}. During daylight hours h_{aer} and other measures of boundary-layer height can be equivalent but during the night h_{aer} gives a depth more representative of the residual layer rather than a measure of the depth of the stable boundary layer. Also, the lidar beam is rapidly attenuated by cloud, so in the presence of thick cloud h_{aer} will be lower than cloud top.

The Doppler velocity, w, can be used to calculate both the vertical velocity variance,

$$\sigma_w^2 = \overline{w'^2}, \tag{2.1}$$

and the vertical velocity skewness,

$$s = \frac{\overline{w'^3}}{\overline{w'^2}^{3/2}}. \tag{2.2}$$

Here the overbars denote both time and spatial means. Time means are two-hour averages centered on the hour of interest, calculated hourly. Spatial means are calculated over each set of three adjacent range gates (covering 108 m). These choices were made to increase the sample sizes for each observation whilst retaining sufficient temporal and spatial resolution. Together these quantities are used to determine both the cloud type, cumulus or stratocumulus, and also whether any cloud layers are decoupled from the surface. One use of the climatology produced by this algorithm will be to provide an observation-based data set that can be used to evaluate numerical weather prediction and climate models, and therefore the boundary-layer types diagnosed relate to the underlying physics that is affecting the boundary layer such as the turbulent kinetic energy budget or turbulent transport. This makes a skewness-based approach to the cumulus/stratocumulus distinction more attractive than just using a cloud fraction threshold.

The sonic anemometer used in this study is mounted at a height of 5 m above the ground and measures the three components of the wind and the sonic temperature at a rate of 20 Hz. Standard eddy-correlation techniques are used to estimate the hourly mean sensible heat flux, $H = \rho C_p \overline{w'T'}$, where ρ is the density of air, C_p is the specific heat capacity of dry air, w' is the fluctuation of the vertical velocity from its detrended hourly-mean value and T' is the fluctuation of the sonic temperature (equivalent to the virtual temperature, not true air temperature) from its detrended hourly-mean value. The hour-mean sensible heat flux is used to determine the stability of the surface layer. It should be noted that in principle this method would work with any Doppler lidar and sonic anemometer.

2.2.2 Probability calculation

In practice, each of these quantities are calculated from finite samples of data and therefore have associated sampling uncertainties. As a result, the algorithm presented here is probabilistic; for each hour of observational data a probability is assigned to each boundary-layer type rather than deterministically producing the most likely type. Figure 2.2 shows the decision path taken to diagnose each boundary-layer type, and the probabilities outlined in Table 2.1. Table 2.1 also shows the observed variable that each probability is based on.

Table 2.1: Definition of probabilities calculated by the algorithm and the variable each probability is based on.

Probability	Variable	Description
p_c	β	probability of the presence of boundary-layer cloud (0 or 1)
p_{st}	$\overline{H}$	probability of the surface layer being stable ($\overline{H} < 0$)
p_{sk}	s	probability of mixing driven by cloud top-cooling being present in the top third of the boundary layer ($s < 0$)
p_{var}	σ_w^2	probability of significant turbulence being present in the top third of the boundary layer ($\sigma_w^2 > 0.1$ m^{2}s^{-2})
p_{de}	σ_w^2	probability of the cloud layer being decoupled
p_{2lay}	β	probability of two cloud layers being present

The use of this probabilistic approach gives information on the significance of the most likely type diagnosed, and in particular highlights when there is uncertainty in the type diagnosed. In addition it reduces the dependence of our results on arbitrary thresholds, although it does not eliminate them. If the number of independent samples of a particular variable X is large enough then, using the central limit theorem, the probability of the mean value of X being less than a threshold value, χ is given by the normal cumulative distribution function

$$p_X = 0.5 \left[1 + \mathrm{erf} \left(\frac{z}{\sqrt{2}} \right) \right], \tag{2.3}$$

where

$$z = \frac{\chi - \overline{X}}{\Delta \overline{X}}. \tag{2.4}$$
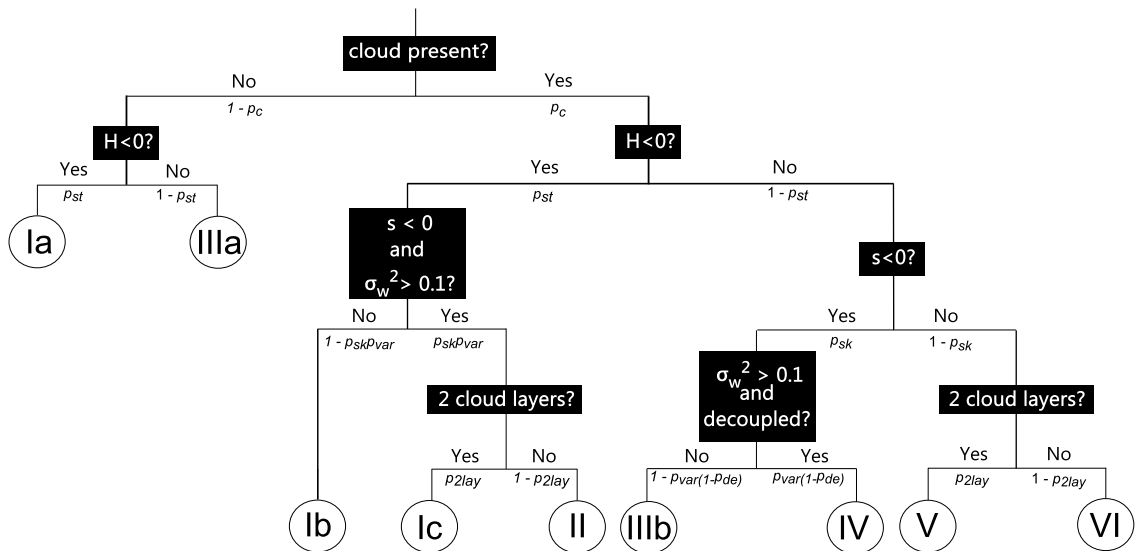
Figure 2.2: A schematic diagram illustrating the decisions made for each boundary-layer type depicted in 2.1 (circles) and its associated probability as described in Table 2.1.

It is assumed that the probability determined at each decision is independent of all other decisions. Table 2.2 shows how, based on Figure 2.2, the probabilities are multiplied to

give the overall probability for each boundary-layer type for each hour. For example the probability of the boundary layer being type V (decoupled stratocumulus over cumulus) is $p_c \times (1 - p_{st}) \times (1 - p_{sk}) \times p_{2lay}$ (probabilities defined in Table 2.1). Note that not all decisions are needed to determine each boundary-layer type. For example, if there is no cloud present ($p_c = 0$) then the only possible types are Ia (Stable) and IIIa (Well mixed).

Table 2.2: How the probabilities are combined to give overall boundary-layer type probability, where the probabilities are defined in Table 2.1.

Boundary-Layer Type	Probability
Ia Stable	$(1 - p_c)p_{st}$
Ib Stable Sc	$p_c p_{st}(1 - p_{sk}p_{var})$
Ic Forced Cu u. Sc	$p_c p_{st} p_{sk} p_{var} p_{2lay}$
II Stable u. Sc	$p_c p_{st} p_{sk} p_{var}(1 - p_{2lay})$
IIIa Well mixed	$(1 - p_c)(1 - p_{st})$
IIIb Sc	$p_c(1 - p_{st}p_{sk})[1 - p_{var}(1 - p_{de})]$
IV Dec Sc	$p_c(1 - p_{st})p_{sk}p_{var}(1 - p_{de})$
V Cu u. Sc	$p_c(1 - p_{st})(1 - p_{sk})p_{2lay}$
VI Cu	$p_c(1 - p_{st})(1 - p_{sk})(1 - p_{2lay})$

2.2.3 Case studies

Here three case study days are presented. These are included to give confidence in the inferences from the observations and to aid the description of the method.

2.2.3.1 Cumulus-topped boundary layer

Figure 2.3 shows the observations for a shallow cumulus-capped layer on 11 September 2009. The difference between the stable and unstable periods can be seen in all variables. The growth of the convective boundary layer throughout the morning is evident in both the backscatter and the standard deviation of the vertical velocity. Just after midday the turbulence driven by surface heating is associated with a skewness value of 1 (panel b) and a maximum vertical velocity standard deviation greater than 1 ms^{-1} (panel c). The sensible heat flux peak is approximately 200 Wm^{-2} (panel d). In this case the clear sky stable boundary-layer type Ia is diagnosed until the sensible heat flux changes sign at 0800 UTC after which unstable types are diagnosed. Cloud appears at 0900 UTC and caps the boundary layer throughout its development until it disperses at 1800 UTC, although the boundary-layer type diagnosed is not cumulus (VI) until 1300 UTC due to the fraction of the hour that is cloudy being less than the threshold required by the

algorithm (5%). The sensible heat flux changes back to negative values at 1800 UTC from which point boundary-layer type Ia is diagnosed indicating a stable surface layer and clear-sky conditions. Examples of raw vertical velocity measurements from similar days can be found in Hogan et al. (2009a). Table 2.3 shows the probability of each boundary-layer type for each hour on this day as derived by the algorithm. The most probable type is shaded in grey. In this straightforward case the most probable boundary-layer type has a probability of greater than 87% for all hours.
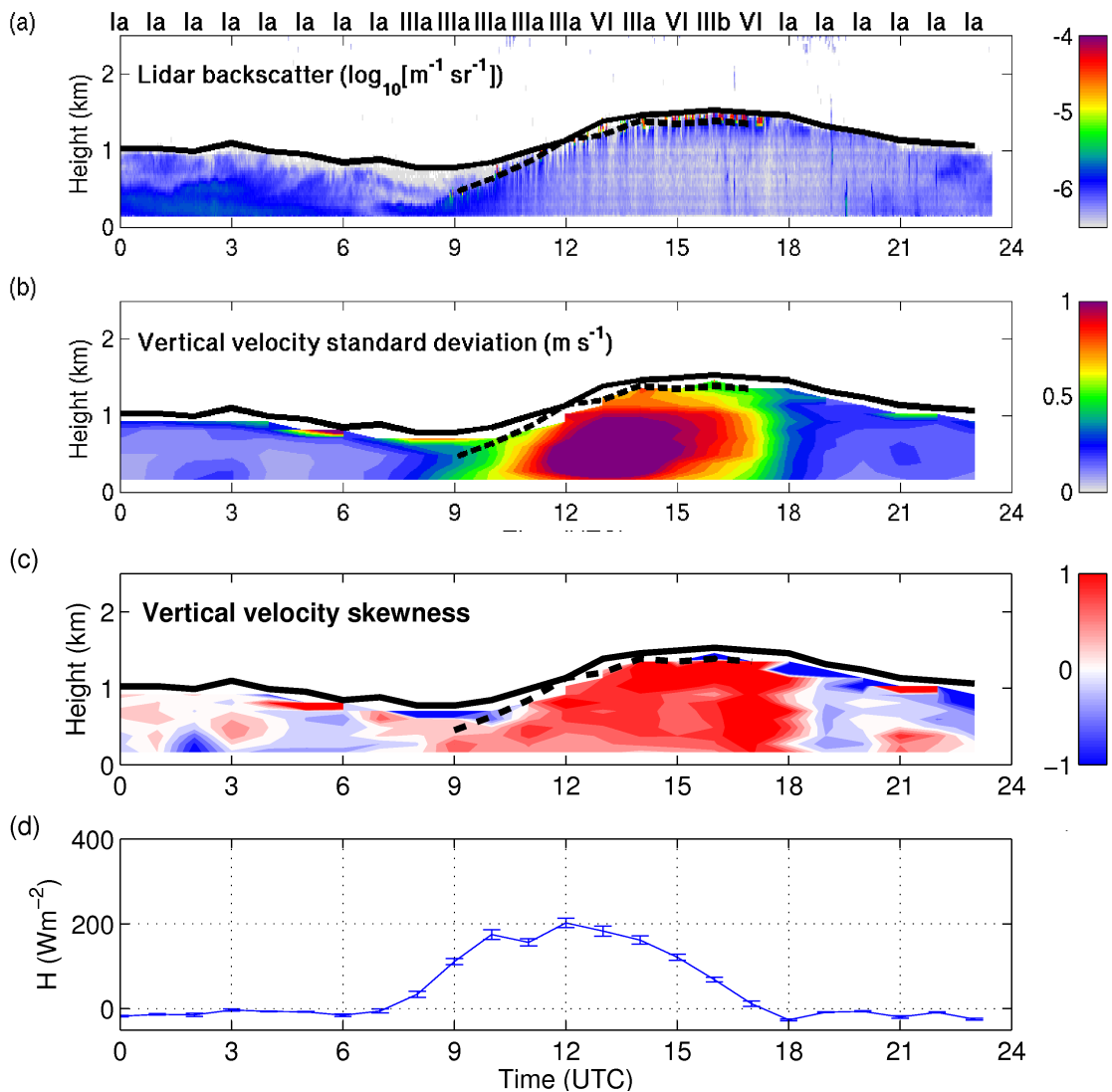
Figure 2.3: Observations taken on 11 September 2009: (a) attenuated lidar backscatter coefficient with the most probable boundary-layer type shown in Roman numerals, (b) 2-hourly mean standard deviation of vertical velocity, (c) 2-hourly mean skewness of vertical velocity, (d) hourly-mean surface sensible heat flux. In (a), (b) and (c) the solid black indicates the diagnosed boundary-layer and the dashed lines indicate the diagnosed cloud bases .

Table 2.3: The probability of each boundary-layer type for each hour of 11 September 2009. Grey shading indicates the most probable type.

Time		0	1	2	3	4	5	6	7	8	9	10	11	12	13	14	15	16	17	18	19	20	21	22	23
Ia	Stable	1	1	1	0.919	1	1	1	0.875	0	0	0	0	0	0	0	0	0	0	1	1	1	1	1	1
Ib	Stable St	0	0	0	0	0	0	0	0	0	0	0	0	0	0	0	0	0	0.032	0	0	0	0	0	0
Ic	Forced Cu u. Sc	0	0	0	0	0	0	0	0	0	0	0	0	0	0	0	0	0	0	0	0	0	0	0	0
II	Stable u. Sc	0	0	0	0	0	0	0	0	0	0	0	0	0	0	0	0	0	0	0	0	0	0	0	0
IIIa	Well mixed	0	0	0	0.081	0	0	0	0.125	1	1	1	1	1	0	1	0	0	0	0	0	0	0	0	0
IIIb	Sc	0	0	0	0	0	0	0	0	0	0	0	0	0	0.094	0	0.119	1	0	0	0	0	0	0	0
IV	Dec Sc	0	0	0	0	0	0	0	0	0	0	0	0	0	0	0	0	0	0	0	0	0	0	0	0
V	Cu u. Sc	0	0	0	0	0	0	0	0	0	0	0	0	0	0	0	0	0	0	0	0	0	0	0	0
VI	Cu	0	0	0	0	0	0	0	0	0	0	0	0	0	0.960	0	0.881	0	0.968	0	0	0	0	0	0

2.2.3.2 Stratocumulus-topped boundary layer

Next a case where stratocumulus breaks up during the day to give a cumulus-capped boundary layer is considered. Figure 2.4 shows the observational data as in Figure 2.3 but from 18 October 2009. Turbulence driven by cloud-top cooling occurs between 0600 and 1000 UTC. This turbulence has a peak of vertical velocity standard deviation, σ_w, of approximately 0.5 ms^{-1} and does not extend to the surface. This is similar to the signature of decoupled stratocumulus cloud observed by Hogan et al. (2009a). At 1100 UTC the turbulence driven from the cloud base reaches the surface and the cloud is no longer decoupled from the surface. Increased surface heating gives rise to an increase in surface-driven turbulence with a peak σ_w of approximately 0.8 ms^{-1} and positive vertical velocity skewness throughout the depth of the boundary layer until 1500 UTC when the sensible heat flux changes sign and the surface layer becomes stable. As expected this stability persists until the end of the day with cloudy boundary-layer types diagnosed. This cloud layer becomes decoupled from 1700 UTC onwards due to turbulence generated by cloud-top cooling. In this more complex case there are four hours in which the most probable boundary-layer type has a probability of less than 60% (Table 2.4).

Table 2.4: As Table 2.3 but for 18 October 2009.

Time		0	1	2	3	4	5	6	7	8	9	10	11	12	13	14	15	16	17	18	19	20	21	22	23
Ia	Stable	0.992	0.096	0.860	0.959	0.917	1	0	0	0	0	0	0	0	0	0	0	0	0	0	0	0	0	0	0
Ib	Stable St	0	0	0	0	0	0	0.001	0	0	0	0	0	0	0	0	0	0.009	0.060	0.111	0.121	0.272	0.625	0.014	0.007
Ic	Forced Cu u. Sc	0	0	0	0	0	0	0	0	0	0	0	0	0	0	0	0	0	0	0	0	0	0	0	0
II	Stable u. Sc	0	0	0	0	0	0	0.982	0.104	0	0	0	0	0	0	0	0	0.030	0.555	0.781	0.56	0.672	0.359	0.552	0.938
IIIa	Well mixed	0.008	0.904	0.140	0.041	0.083	0	0	0	0	0	0	0	0	0	0	0	0	0	0	0	0	0	0	0
IIIb	Sc	0	0	0	0	0	0	0	0	0.014	0.018	0.046	0.942	0.091	0.862	0.875	0.400	0.662	0.129	0.081	0.158	0.001	0	0	0
IV	Dec Sc	0	0	0	0	0	0	0.017	0.896	0.986	0.982	0.921	0.011	0.071	0.016	0	0.030	0.289	0.246	0.025	0.160	0.039	0.006	0.423	0.055
V	Cu u. Sc	0	0	0	0	0	0	0	0	0	0	0	0	0	0	0	0	0	0	0	0	0	0	0	0
VI	Cu	0	0	0	0	0	0	0	0	0	0	0.033	0.047	0.838	0.122	0.125	0.570	0.010	0.010	0.002	0.001	0.016	0.010	0.011	0

2.2.3.3 A more complex day

Figure 2.5 shows the same as Figure 2.3 but for 4 July 2009. This case has been included as it is an example of a more complex day when the "textbook" boundary layer evolution is not as evident. It also includes boundary-layer type V (cumulus under stratocumulus) at 1000 and 1200 UTC, when more than one cloud layer is observed. At 1200 UTC positive vertical velocity skewness can be seen up to a height of approximately 500 m
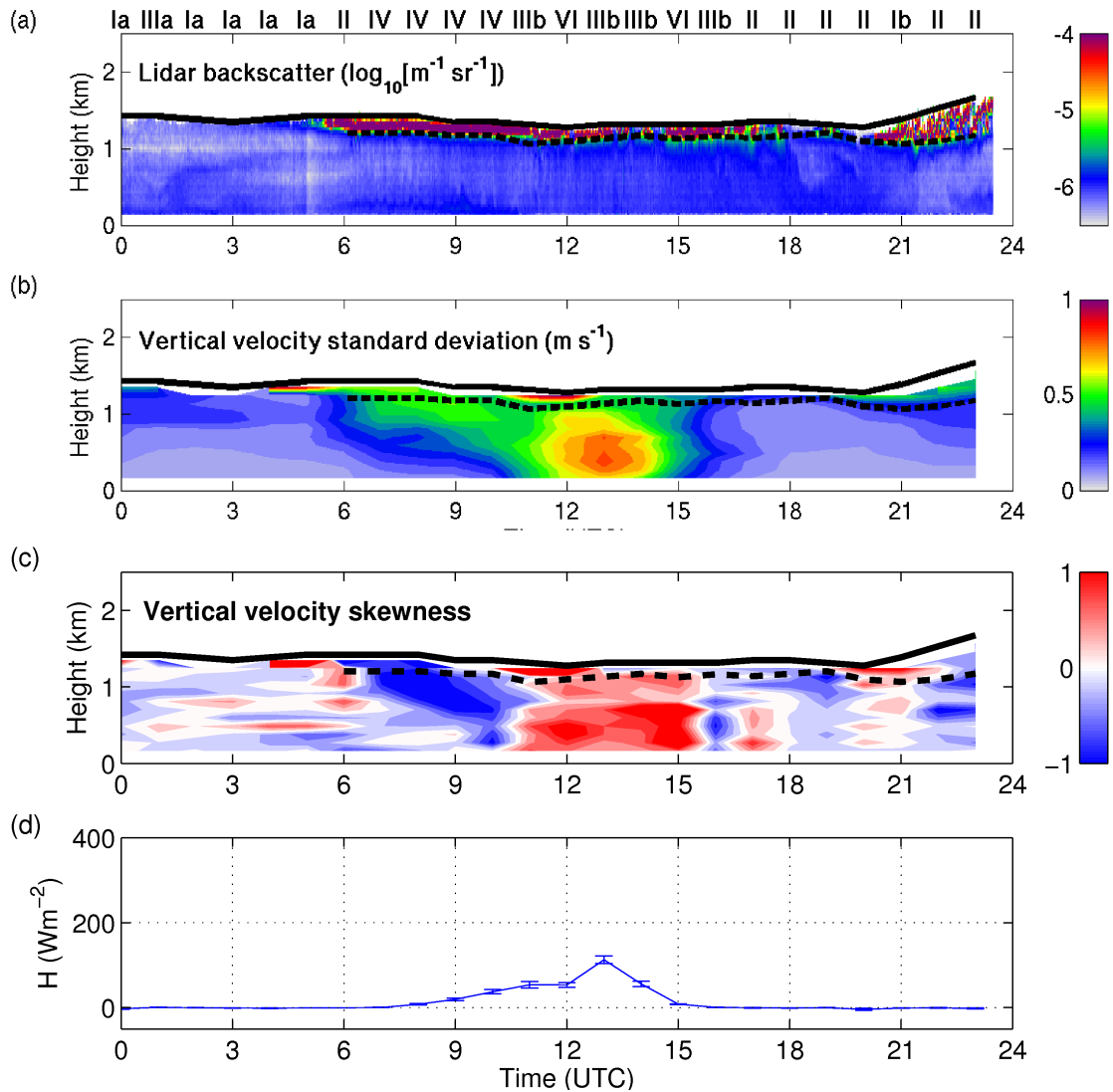
Figure 2.4: As Figure 2.3, but for 18 October 2009.

beneath a cloud layer which is indicative of cumulus cloud; however, above the cloud at 1 km there is a shallow layer, approximately 200 m thick, of negative vertical velocity skewness beneath another cloud layer which is indicative of stratocumulus cloud, hence the diagnosis of cumulus under decoupled stratocumulus. This boundary-layer type is common over the ocean (Norris, 1998), but there have been no long term studies of this boundary-layer type over land to evaluate its frequency. In this case there are three hours in which the most probable boundary-layer type has a probability of less than 50% (Table 2.5). Note that no boundary-layer type was diagnosed at 0300 or 0400 UTC as the cloud base is below the first range gate of the lidar during those times and therefore there was no skewness or variance information to base the diagnosis on.
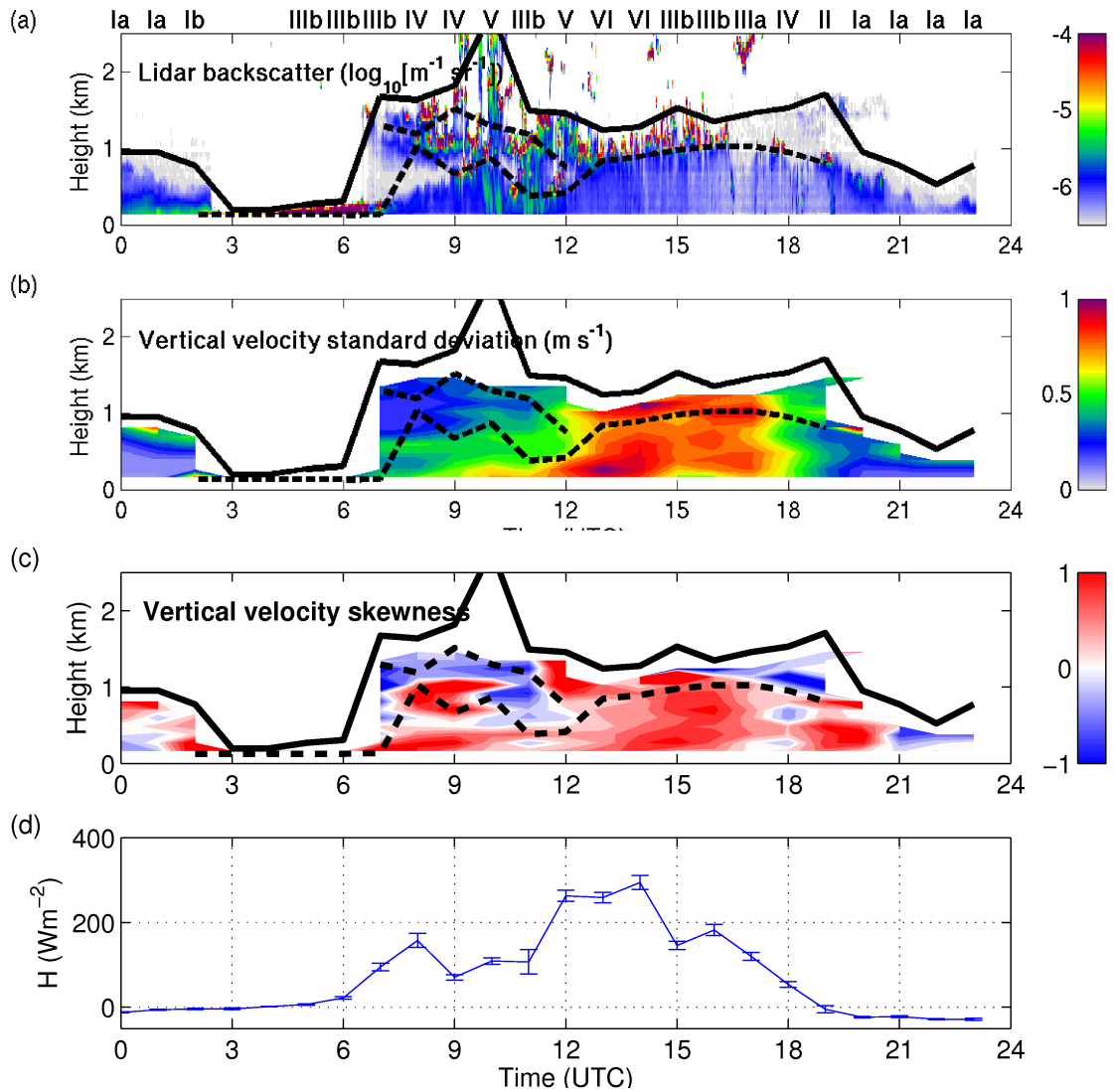
Figure 2.5: As Figure 2.3, but for 4 July 2009.

Table 2.5: As Table 2.3 but for 4 July 2009.

Time		0	1	2	3	4	5	6	7	8	9	10	11	12	13	14	15	16	17	18	19	20	21	22	23
Ia	Stable	1	1	0			0	0	0	0	0	0	0	0	0	0	0	0	0	0	0	1	1	1	1
Ib	Stable St	0	0	0.985			0	0	0	0	0	0	0	0	0	0	0	0	0	0	0.243	0	0	0	0
Ic	Forced Cu u. Sc	0	0	0			0	0	0	0	0	0	0	0	0	0	0	0	0	0	0	0	0	0	0
II	Stable u. Sc	0	0	0			0	0	0	0	0	0	0	0	0	0	0	0	0	0	0.475	0	0	0	0
IIIa	Well mixed	0	0	0			0	0	0	0	0	0	0	0	0	0	0	0	1	0	0	0	0	0	0
IIIb	Sc	0	0	0.015			1	1	1	0.366	0.003	0	0.499	0.001	0.009	0.155	0.987	0.941	0	0.011	0.119	0	0	0	0
IV	Dec Sc	0	0	0			0	0	0	0.488	0.906	0	0.479	0.001	0.256	0.058	0.013	0.059	0	0.989	0.068	0	0	0	0
V	Cu u. Sc	0	0	0			0	0	0	0.097	0.091	1	0.004	0.665	0	0	0	0	0	0	0	0	0	0	0
VI	Cu	0	0	0			0	0	0	0.049	0	0	0.333	0.735	0.787	0	0	0	0	0	0.095	0	0	0	0

2.2.4 The algorithm in detail

Here each decision in the algorithm, as shown in Figure 2.2, is discussed and justified.

2.2.4.1 Presence of cloud

All clouds below h_{aer} are considered, by our definition, to be in the boundary layer and are therefore included in the diagnosis of the boundary-layer type. It is important to reiterate that h_{aer} is actually a measure of the aerosol depth and is not necessarily equal to other measures of the boundary layer height in the literature. Cloud is considered to be present during a given hour if a cloud is detected for more than 5% of the hour-long window. The value of 5% was chosen as it is comparable to the cloud fraction of small cumulus clouds that need to be detected. The sensitivity to this threshold has been tested and Table 2.6 shows the percentage of cloudy and non-cloudy boundary-layer types diagnosed for a range of threshold values. When the threshold is increased to 10% approximately 3% of the boundary-layer types diagnosed change from cloudy to non-cloudy. If the threshold is removed completely approximately 4% of the types move from cloud-free to cloudy. The backscatter threshold used to identify cloud is 5×10^{-5} m^{-1}sr^{-1}. This threshold is consistent with that used in other studies such as Hogan et al. (2004) and Westbrook et al. (2010). Note that p_c can only have a value of 0 or 1 as it is the presence of cloud that is being determined, not the fraction of time a cloud is present. No error on cloud presence is determined as the difference in backscatter attenuation coefficient between cloud and aerosol is very large and therefore the error in detecting a cloud with the lidar is very small.

2.2.4.2 Stability

The stability of the surface layer is determined using the sign of the sensible heat flux, H. The probability of H being negative, i.e. the surface layer being stable, p_{st}, is found by calculating the sampling error of H using an autocorrelation method (Wilks, 1995) as follows.

Table 2.6: Cloud fraction threshold sensitivity analysis

Cloud fraction threshold (%)	Cloudy types (%)	Non-cloudy types (%)
0	58.21	41.79
5	54.91	45.09
10	52.03	47.97
20	47.73	52.27
50	37.48	62.52

The autocorrelation function is defined as

$$R(\tau) = \frac{1}{N\sigma_H^2} \sum_t H(t)H(t+\tau),$$
(2.5)

where N is the number of samples of H in 1 hour and τ is a time lag (Kaimal & Finnigan, 1994). The time to independence or integral time scale, τ_{ind}, of the autocorrelation function is then defined as

$$\tau_{ind} = \int_0^{\tau^*} R(\tau)\,\mathrm{d}\tau$$
(2.6)

where τ^* is the smallest lag time such that $R(\tau) = 0$. Equation (2.6) is used to calculate the effective number of independent samples, N_i, in the hour using the expression

$$N_i = \frac{N\tau_0}{2\tau_{ind}},$$
(2.7)

where τ_0 is the time between each sample, equal to 0.05 s for our instrument. The standard error of the hourly mean sensible heat flux measurement, $\Delta\overline{H}$, is then determined using

$$\Delta\overline{H} = \frac{\sigma_H}{\sqrt{N_i}},$$
(2.8)

where σ_H denotes the standard deviation of the H measurements over the hour.

Due to the large number of independent samples, typically around 600, Equations 2.3 and 2.4 can be used to calculate the probability, p_{st}, of a negative hourly-mean value of sensible flux with X replaced with H and threshold value χ taken to be zero. Note that the probability of the surface layer being stable derived here is not sensitive to our choice of sonic temperature over true temperature.

2.2.4.3 Cloud type

The distinction between stratocumulus and cumulus is needed to distinguish between unstable types IIIb (Sc), IV (Dec Sc), V (Cu u. Sc) and VI (Cu), and stable types Ib (Stable St), Ic (Forced Cu u. Sc) and II (Stable u. Sc). The sign of the minimum of the vertical velocity skewness (see (2.2)), in the top third of the boundary layer indicates whether stratocumulus or cumulus cloud is present if it is assumed that in stratocumulus cloud turbulence is mostly driven from above the cloud through cloud-top cooling (negative skewness) and the turbulence associated with cumulus cloud is driven from the surface (positive skewness) (LeMone, 1990; Moeng & Rotunno, 1990; Moyer & Young, 1991;

Lothon et al., 2009; Hogan et al., 2009a).

An example of the difference between cumulus and stratocumulus skewness profiles is illustrated in Figure 2.4(c). Negative skewness can be seen in the top third of the boundary layer from 0600 UTC to 1000 UTC implying the dominance of turbulence driven by cloud top cooling and the presence of stratocumulus cloud. However, from 1100 UTC positive skewness can be seen, implying that surface driven turbulence becomes dominant and therefore the presence of cumulus cloud. Note that if the boundary layer is diagnosed as stable and two layers of cloud are present then only the skewness between the cloud layers is considered, as it is the type of the upper-level cloud that is of interest.

The probability of the minimum skewness in the top third of the boundary layer being negative, p_{sk}, is calculated using an autocorrelation method analogous to that described in Section 2.2.4.2. The standard error in the sample skewness, Δs, is given by

$$\Delta s = \sqrt{\frac{6}{N_i}},$$

(2.9)

(Tabachnick & Fidell, 1989). As before, it is assumed that the distribution is Gaussian, with N_i in this case being approximately 60. The same method used to determine p_{st} in Equations 2.3 and 2.4 is also used to calculate p_{sk}.

The vertical velocity variance is also used to determine cloud type as it is a proxy for the presence of turbulence. For cloud to be considered as stratocumulus rather than stratus, a significant amount of turbulence driven by cloud-top cooling by outgoing long-wave radiation is needed within and possibly below the cloud depending on the thickness of the cloud layer. The distinction between stratus and stratocumulus is important as stratus cloud will have no influence on the aerosol layer beneath but may have a similar skewness and backscatter profile. In this method a significant level of turbulence is defined as having maximum vertical velocity variance greater than 0.1 $m^2 s^{-2}$, as observed by Albrecht et al. (1995), in the top third of the boundary layer or at the top of the first cloud layer. Sensitivity tests have been performed on this threshold value. The results of these are shown in Table 2.7. Reducing the threshold to 0.05 $m^2 s^{-2}$ only changes the percentage of cases where stratocumulus cloud is diagnosed from 8.85% to 8.37%. A larger impact is seen when threshold was increased to 0.2 $m^2 s^{-2}$ especially in the cases where the surface layer is stable.

The calculation of p_{var} is the same as that for p_{sk} except the standard error in variance

measurements, $\Delta\overline{w'^2}$, is given by

$$\Delta\overline{w'^2} = \sigma_w^2 \times \sqrt{\frac{2}{N_i - 1}}, \qquad (2.10)$$

(Spiegel & Stephens, 1998) and the threshold value in (2.4), χ, is set to 0.1 m^{2}s^{-2}.

2.2.4.4 Decoupled stratocumulus

Figure 2.4 shows a case study day where the cloud layer evolves from decoupled to coupled. At 0900 UTC there is a layer of cloud diagnosed as stratocumulus due to negative skewness in the top third of the boundary layer and vertical velocity variance greater than 0.1 m^{2}s^{-2} in the top third of the boundary layer. It is trivial to diagnose the layer as decoupled by eye as the turbulence below the cloud base does not reach the surface or the top of any turbulence driven by surface heating. At 1500 UTC on the same day the cloud layer still persists but the surface-driven turbulence reaches up to cloud base and thus the boundary layer is coupled. Again, by eye this diagnosis is trivial. However, in practice, implementing this decision as an objective algorithm is non-trivial.

One method of determining whether the cloud layer is decoupled is by considering the profiles of vertical velocity variance. In the case where the cloud layer is coupled with the surface it is expected that the vertical variance profile would have a maximum in the bottom half of the boundary layer. Associated with this a convex variance profile is expected, i.e. the variance profile to have a gradient that decreases with height in the lower half of the boundary layer (Lenschow et al., 1980; Sorbjan, 1989). On the contrary, if a layer is decoupled then a maximum in the vertical velocity variance profile in the top half of the boundary layer is expected which in turn will give a gradient that increases with height in the lower half of the boundary layer. These differences can be seen in Figure 2.6 (panels (a) and (c)) which shows the vertical profiles of two-hour mean vertical

Table 2.7: Variance threshold sensitivity analysis

Variance threshold (m^{2}s^{-2})	Types Ic and II (%)	Type IV (%)
0.05	18.62	8.37
0.1	17.65	8.85
0.2	14.09	7.87
0.3	11.08	6.83

velocity variance for 0900 UTC and 1400 UTC on the 18 October 2009. It is possible to classify the shape of the variance profile using its second derivative as this describes the change of gradient with height. As the vertical profiles of variance are noisy, one cannot simply use the numerical second derivative of the raw measurements so a quartic function is fitted to the observed profile and the second derivative of this quartic is used. This fit is shown in Figure 2.6 by a dashed line. Figure 2.6 panel (b) shows a decoupled case. The second derivative is positive at all but one range gate in the bottom half of the boundary layer and therefore the boundary layer is diagnosed as decoupled. Figure 2.6 panel (d) shows the same plot but in this case the second derivative is negative in the bottom half of the boundary layer and thus the boundary layer is diagnosed as coupled.

The probability of this second derivative being negative is calculated at the height of maximum curvature of vertical velocity variance in the lower half of the boundary layer, indicated by a black circle in Figure 2.6(b) and (d), the error covariance matrix of the co-efficients of the quartic fit is used to compute the standard error of the second derivative. As before, the distribution is assumed to be Gaussian and therefore the probability, p_{de}, that the second derivative of the variance is negative in $0 < z < h/2$, can be calculated using the same method as Sections 2.2.4.2 and 2.2.4.3, which can be equated to the probability the boundary layer is coupled. Where there is insufficient data to perform the quartic fit p_{de} is set to 0.5.

2.2.4.5   Number of cloud layers present

Finally, the number of cloud layers present during the hour is estimated directly from the lidar backscatter data. The lidar beam is rapidly attenuated by cloud and therefore have little information about the depth of the clouds or whether there are multiple cloud layers in a single profile. However, it is possible to use an hour of backscatter profiles from the lidar to determine whether shallow cumulus cloud is present under a stratocumulus layer (types Ic and V). The probability of two or more cloud layers being present in a given hour is estimated by first splitting the hour into three 20 minute windows. The height at which cloud is identified in each lidar profile is found in the first window. These heights are then binned into intervals of 108 m, 3 lidar range gates, and a pdf of these heights is created. Independent cloud layers are identified as peaks in the pdf separated by at least one bin where the probability of cloud is less than 5%. This threshold is used to ensure that ascending or descending layer clouds (e.g. in the vicinity of fronts)
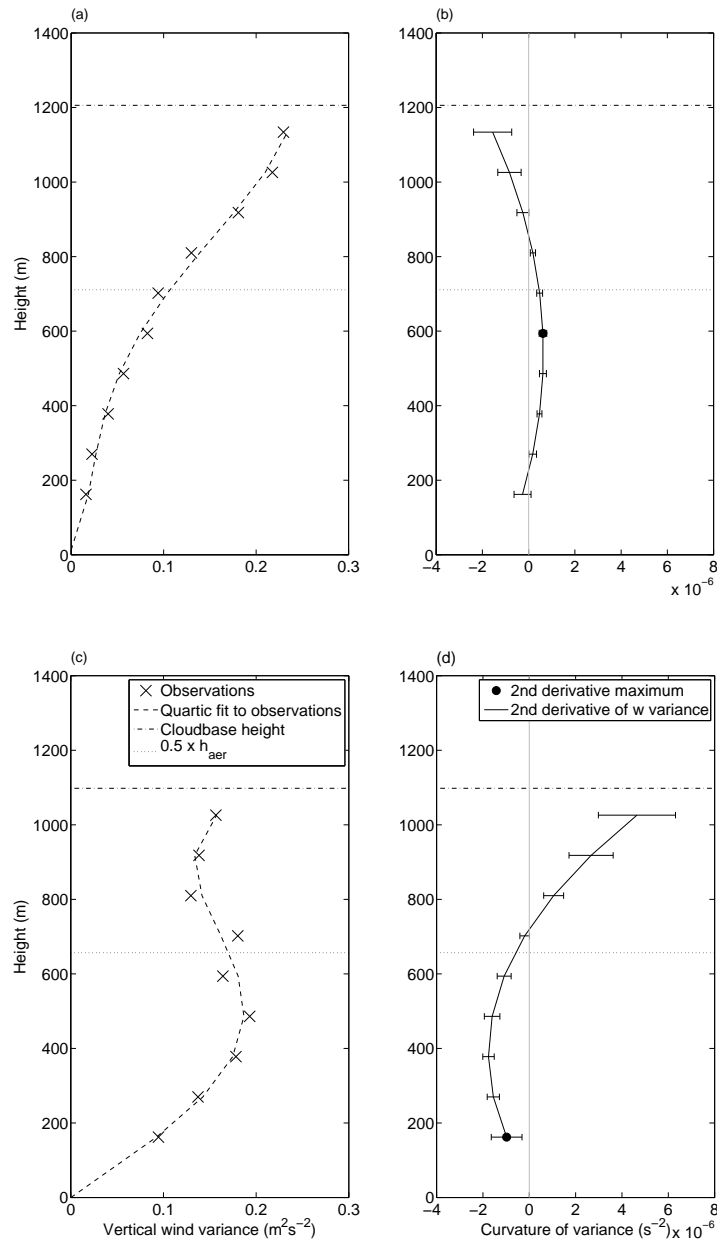
Figure 2.6: (a) Vertical profile of 2-hourly mean vertical velocity variance observations (crosses) and its corresponding quartic fit (dashed line) for a decoupled boundary layer at 0900 UTC on 18 October 2009. Also shown are the cloud base height (dot-dash line) and the height of the lower half of the boundary layer (dotted line). (b) Vertical profile of the second derivative of the fit of vertical velocity variance and associated error (solid black line). The black circle highlights the height of the maximum curvature of vertical velocity variance in the lower half of the boundary layer which the algorithm uses to assess the probability of the boundary layer being decoupled. (c) As (a) for a coupled boundary layer at 1500 UTC on 18 October 2009 . (d) As (b) for a coupled boundary layer.

are not diagnosed as multiple layers. The same process is repeated on the remaining two windows (Figure 2.7). The probability of two or more layers of cloud being present, $p_{2\text{lay}}$, is the number of 20-minute windows with two or more layers divided by three, the number of 20-minute windows considered. This probability is only used to distinguish

between stable boundary-layer types Ib and Ic and unstable types V and VI.
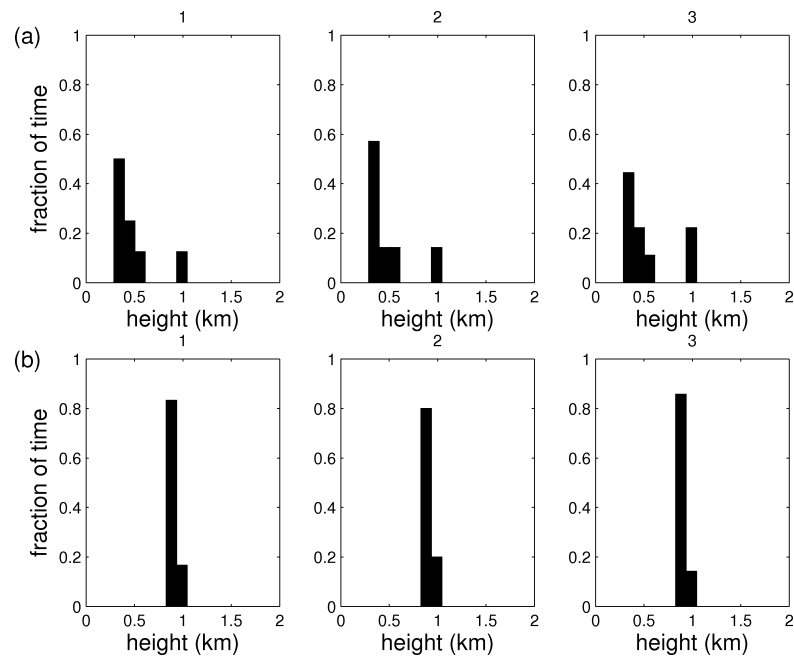
Figure 2.7: (a) Cloud base height distributions for 1130–1230 UTC on 4 July 2009 (shown in Figure 2.5) at which time $p_{2lay} = 1$ (two cloud layers present). (b) Cloud base height distributions for 1430–1530 UTC on 4 July 2009 at which time $p_{2lay} = 0$ (one cloud layer present). A full description can be found in Section 2.2.4.5.

2.2.5   Additional constraints

As with all observational techniques there are limitations in the case of missing data. Firstly, for a boundary-layer type to be diagnosed, it is stipulated that more than 90% of the sonic anemometer and 50% of the lidar data must be available for each hour. The three lowest lidar range gates are removed as they are unreliable. Therefore the minimum detectable height of the lidar is 108 m. If the aerosol depth is found to be below 270 m (the 4th range gate) then boundary-layer type is not diagnosed as there are no measurements of below cloud vertical velocity skewness and variance measurements to base the decision on. If the cloud base is diagnosed to be below 270 m then boundary-layer type is diagnosed as type Ib or IIIb with the probability of each type being based in the probability of the surface layer being stable. This is imposed as in this situation there is only one lidar gate of information about the vertical velocity skewness and variance to base the decision on. Also, the type is not diagnosed when rain is recorded at Chilbolton. This is due to the lidar retrieval being unreliable when it is raining. Table 2.8 shows the number of hours each of the above constraints effect in the three year data set considered in this study 62.38% of hours are diagnosed. Within the hours that have a boundary-layer

type diagnose there are situations that cannot be easily categorised into one of the nine types shown in Figure 2.1. In these circumstances the most probable boundary-layer type can have a probability as low as 40%.

2.3 Results

The probabilistic algorithm has been applied to 3 years of lidar and sonic anemometer data, 1 June 2008 to 31 May 2011, from Chilbolton. This has been used to produce a long-term statistical analysis of boundary-layer type derived from observations. The distribution of boundary-layer types throughout this period is shown in Figure 2.8. This distribution is created by summing the probabilities of each type for each hour and then dividing by the total number of hours diagnosed. Overall, it can be seen that the most frequently occurring boundary-layer type is stable with clear skies (30.0%). The most frequently occurring unstable type is well mixed with no cloud (15.4%), followed by decoupled stratocumulus (10.3%). Cumulus under stratocumulus, little studied over land, occurs during 1.0% of the period studied. The distribution of types between stable and unstable is similar to that found by Luna & Church (1972) which classifies the boundary layer according to Pasquill stability classes at a single site in Augusta, Georgia. The percentage occurrence of cumulus and stratocumulus cloud is in broad agreement that found over the Southern Great Plains (Lazarus et al., 2000 and Kollias et al., 2007) and all land averaged between 50 and 60°N (Hahn et al., 1990).

The observed time series of boundary-layer type can be split both into seasons and time of day. This is shown in Figure 2.9; note all times are UTC. A clear diurnal and seasonal cycle is present in the boundary-layer types. As expected the boundary layer is nearly always stable in the hours of darkness and in the spring and summer nearly always unstable in daylight thus winter has a much shorter period of unstable boundary-layer types than the summer. This supports the study by Liu & Liang (2010) which classified

Table 2.8: The breakdown of the number of hours where boundary-layer type is diagnosed.

Number of hours	
With rain	5560
With missing missing sonic anemometer data	3663
With missing lidar data	502
With h_{aer} less than 270m	159
Diagnosed	16396
Total in dataset	26280
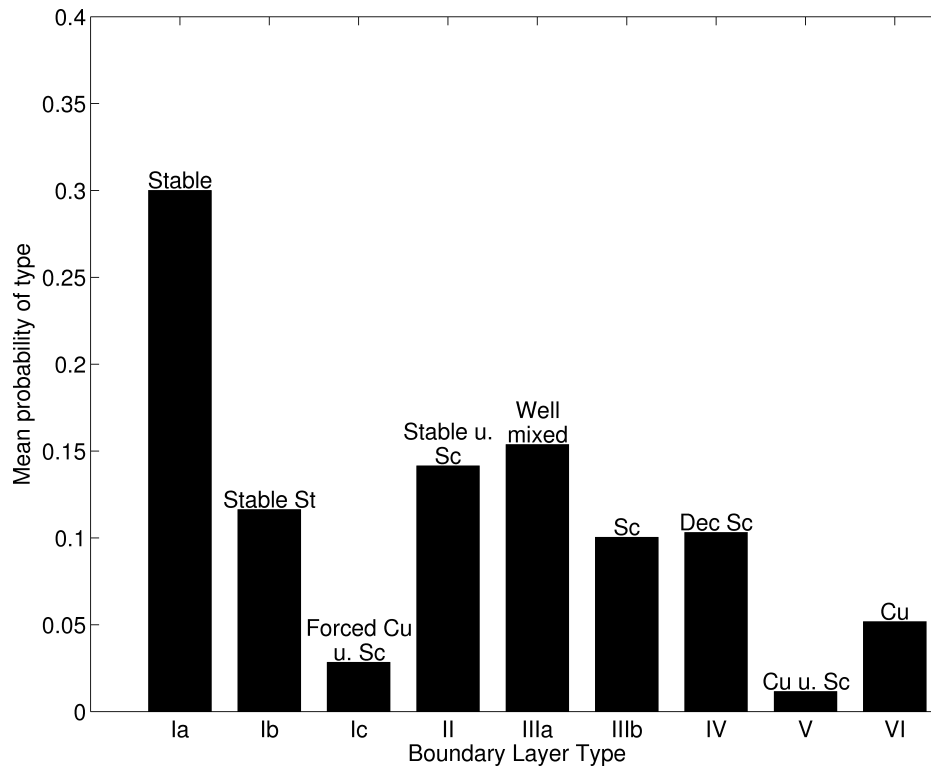
Figure 2.8: The mean probability of each boundary-layer type over the study period of 1 June 2008 - 31 May 2011.

the boundary layer into three regimes, stable, neutral and unstable, using potential temperature profiles from radiosonde ascents from 14 different field campaigns around the world. For the land sites included in their study, they also found a much greater prevalence of unstable convective and neutral boundary layers between 09 UTC and 15 UTC (daylight hours) than during the hours of darkness

As in the overall distribution the most common type in all seasons is type Ia (stable with
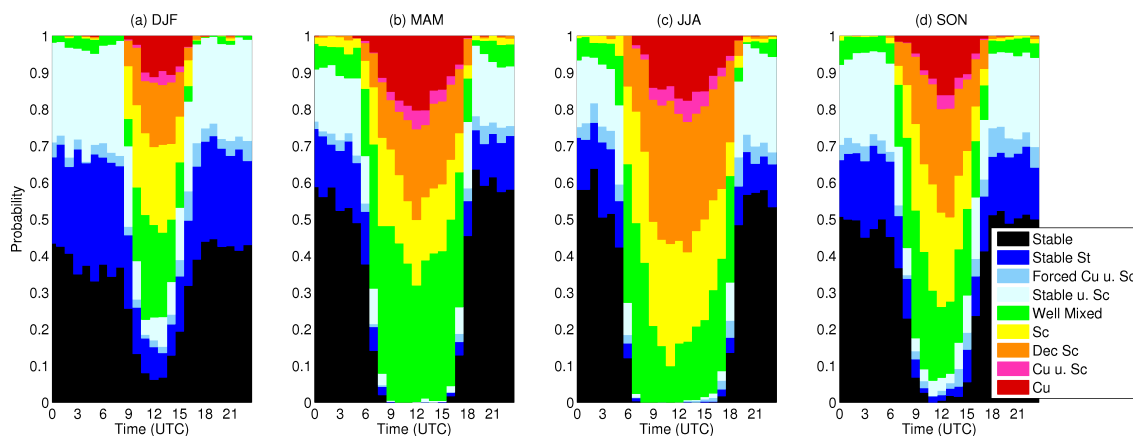
Figure 2.9: The diurnal distribution of boundary-layer types as a function of season (a) winter, (b) spring, (c) summer, (d) autumn.

no cloud). The occurrence of stable boundary-layer types Ia, Ib, Ic and II is much higher in the winter than the summer. Boundary-layer types V and VI, those with cumulus cloud, are more prevalent in the warm seasons as are types with stratiform cloud. Cumulus cloud was also found to be most common in warm seasons in the studies by Hahn et al. (1990), Lazarus et al. (2000) and Kollias et al. (2007) however they found that stratiform cloud was more prevalent in the cold seasons which contradicts the increase in the presence of stratiform cloud over the North Atlantic in warm seasons found by Klein & Hartmann (1993). Although the study presented here is over land, not ocean, and so a different cloud climatology might be expected. Cumulus cloud occurrence peaks at midday in the observations presented here. This agrees with Lazarus et al. (2000). Another feature to note is that stratocumulus-topped boundary layers occur more frequently in the afternoon, after 1200 UTC, in all seasons. This finding is also supported by Lazarus et al. (2000). The distribution found using the hourly probabilities is very similar to the distribution of the most common boundary-layer type (not presented here).

2.3.1 Most likely sequences of boundary-layer type

Another feature that can be studied is the most common sequence of boundary-layer type throughout the day. As there are 9 possible types and 24 hours in a day to transition from there are too many possible combinations to consider the complete diurnal cycle. By taking the most probable boundary-layer type at five representative times throughout the day it is possible to deduce the most likely evolution of boundary-layer type through the day and whether they concur with the "textbook" evolution of a stable nocturnal boundary layer, with a well mixed convective boundary layer growing after sunrise and cumulus cloud developing as the convective boundary layer grows (Stull, 1988 and Garratt, 1992). Table 2.9 shows the 20 most common combinations of boundary-layer type, using the most probable type at 0300, 0900, 1200, 1500 and 2100 UTC, along with their frequency of occurrence. Note that only days with boundary layers diagnosed at all these times are included in this analysis. For the period considered here the number of days used is 807. The distribution of boundary-layer types for this reduced period is shown in Figure 2.10.

The most common "day" is that of no cloud with the stability changing from stable to unstable during daylight hours. Even though cloud is common over the UK, this transitional pattern occurs 6.4% of the time, which equates to 52 days in our 3-year dataset.
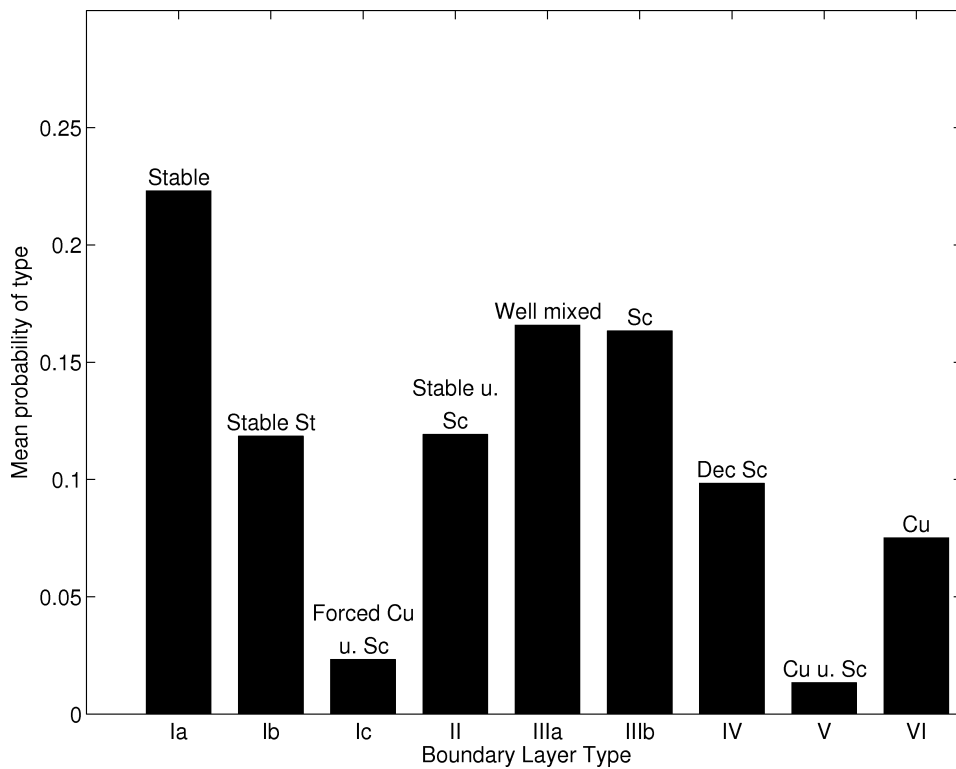
Figure 2.10: The probability distribution of boundary-layer types diagnosed on the days considered in the most likely sequences of boundary-layer type analysis.

Table 2.9: The top 20 most common boundary-layer type evolutions, grey shading indicating the presence of cloud.

	Time of Day					Occurrence	
	03:00	09:00	12:00	15:00	21:00	percentage of time	number of days
1	Stable	Well mixed	Well mixed	Well mixed	Stable	6.4	52
2	Stable St	Sc	Sc	Sc	Stable St	1.4	11
3	Stable	Stable	Well mixed	Stable	Stable	1.2	10
4	Stable	Well mixed	Well mixed	Well mixed	Well mixed	1.0	8
5	Stable	Well mixed	Cu	Cu	Stable	0.9	7
6	Well mixed	Well mixed	Well mixed	Well mixed	Stable	0.9	7
7	Stable u. Sc	Well mixed	Well mixed	Well mixed	Stable	0.7	6
8	Stable	Sc	Sc	Well mixed	Stable	0.7	6
9	Stable	Well mixed	Well mixed	Well mixed	Stable u. Sc	0.7	6
10	Stable u. Sc	Sc	Dec. Sc	Dec. Sc	Stable	0.6	5
11	Stable	Sc	Dec. Sc	Dec. Sc	Stable u. Sc	0.6	5
12	Stable	Well mixed	Well mixed	Cu	Stable	0.6	5
13	Stable St	Sc	Sc	Sc	Stable u. Sc	0.5	4
14	Stable St	Sc	Sc	Dec. Sc	Stable	0.5	4
15	Stable St	Sc	Dec. Sc	Dec. Sc	Stable u. Sc	0.5	4
16	Stable St	Sc	Cu	Dec. Sc	Stable	0.5	4
17	Stable St	Sc	Cu	Cu	Stable	0.5	4
18	Stable St	Sc	Cu	Well mixed	Stable	0.5	4
19	Stable St	Sc	Well mixed	Well mixed	Stable	0.5	4
20	Stable St	Dec. Sc	Dec. Sc	Dec. Sc	Stable	0.5	4

This pattern being the most probable is not unexpected as there is only one possible sequence for boundary layers that have no cloud (assuming the boundary layer is stable at night and unstable during the day). This low percentage for the most probable sequence implies there is a very large diversity of sequences observed even when using a reduced number of observations. The "textbook" diurnal evolution (Stull, 1988) of the boundary layer over land (Stable → Well mixed → Cu → Cu → Stable) only occurs 0.9% of the time at Chilbolton, the fifth most probable transition. It is more common to have stratocumulus-capped boundary layers throughout all daylight hours (1.2%). The top ten boundary-layer transition sequences account for approximately 13.9% of the period studied. It is surprising to find such a large number of unstable cases during the night. Well mixed cases at 21 UTC (fourth) are related to longer day length in the warm seasons but the well mixed types at 03 UTC (sixth) are due the probability of the surface layer being stable, p_{st}, being small. The top twenty results are largely invariant of whether the start time used is 0200, 0300 or 0400 UTC.

The skewness and variance characteristics of boundary-layer types IIIa (well mixed) and VI (cumulus) are similar but with type VI having a cumulus cloud capping the aerosol layer. This similarity can be seen by comparing Figures 2.3 and 2.5. Also, there are several transitions that are similar if the time of the transition from stable to unstable is ignored. An example of this is pattern one and three. Both sequences are cloud free but pattern three comes from winter days where the sensible heat flux is negative at 0900 and 1500 UTC but positive at 1200UTC with no cloud. If Table 2.9 is reconsidered with this in mind then transition patterns 1, 3, 4, 5, 6, 7, 9 and 12 can be combined giving the most common transition occurring 11.5% of the time. Sequences 2,10, 11, 13, 14, 15 and 20 can be combined as stratocumulus cloud is present throughout daylight hours (4.5%). Also, sequences 5 and 12 can be combined increasing the occurrence of the "textbook" diurnal evolution of the boundary layer to 1.5% of the time considered.

Boutle et al. (2010) outline another paradigm for the evolution of the boundary layer during the passage of a mid-latitude cyclone. In this case the forcing is not diurnal heating and cooling but large scale thermal advection. In regions of positive sensible heat flux a convective boundary layer develops as the cyclone intensifies. Firstly a single mixed layer forms (types IIIa and IIIb) with capping cloud once the lifting condensation level is reached. In the idealised simulations performed by Boutle et al. (2010), by day 4 stratocumulus cloud becomes decoupled from the surface (type IV) with shallow cumulus cloud beneath in some regions (type V). By day 7 cumulus convection is strong enough

to produce a cumulus-capped boundary layer. In the warm conveyor belt region features of a classical nocturnal boundary-layer are seen (types Ia, Ib, Ic and II). As cyclones propagate eastwards, at any fixed point in space the boundary-layer will undergo transitions between stable and unstable regimes on a timescale of 3-4 days. However, the method described here does not lend itself to validating this evolution as it is not reliable in the presence of precipitation.

2.4   Conclusions

In this chapter it has been demonstrated that it is possible to classify the boundary layer into 9 different types using variables obtained from a continually operating vertically pointing Doppler lidar combined with surface sensible heat flux measurements. The new method has been applied to 3 years of data and a climatology of boundary-layer type has been produced. This climatology exhibits clear diurnal and seasonal cycles which are dominated by variations in the surface sensible heat flux. The most common boundary-layer type is stable with clear skies (30.0%). The most common unstable boundary-layer type is unstable cloud free (15.4%). Decoupled stratocumulus-capped boundary layers which are little studies over land occur 10.3% of the time. More cumulus capped boundary layers are diagnosed in the warm seasons than in the winter.

The most probable diurnal sequence of boundary-layer type has also been investigated. It has been found that the most probable evolution is that of a cloud free boundary layer (6.4% of the period studied) with the "textbook" boundary layer evolution of stable, well mixed, cumulus-capped, stable, occurring approximately 0.9% of the period studied. The sensitivity of these results to the chosen threshold values, and other limitations of the method are also discussed.

In Chapter 3 this approach will be used to evaluate the boundary-layer type diagnosed in the Met Office Unified Model. This is feasible as each of the categories in this study map directly on to the six categories used in the Met Office scheme ((Lock et al., 2000)). This comparison could also be extended to other operational models or to different geographical locations which have co-located Doppler lidar and surface heat flux measurements.

Chapter 3

How well do models predict boundary-layer type?

This chapter deals with the evaluation of a numerical weather prediction model, the 4 km resolution Met Office Unified model, using the observed boundary-layer types diagnosed using the method outlined in Chapter 2. First the data being compared are described and then climatologies of boundary-layer type are presented for both the model and observations. The effect of forecast lead time, model resolution and season on skill are investigated, and ,finally, the most probable boundary-layer type transitions are considered.

3.1   Why evaluate the skill of boundary layer type?

Climate models vary substantially in their predictions of boundary layer clouds in a warmer climate. This gives an uncertainty in radiative feedback which is one of the largest sources of uncertainty in climate prediction (Bony et al., 2006; Webb et al., 2006). Bony & Dufresne (2005) have shown that those climate models with the largest climate sensitivity are the ones that also forecast the largest decrease in boundary layer cloud occurrence. Also, Dai & Trenberth (2004) found that low clouds (below 700 mb) are the main contributor to diurnal variations in cloud amount especially in marine stratocumulus regions. Another meteorological feature occurring in the boundary layer that may have important consequences for climate is the representation of the low level jet (Stensrud, 1996).

On a more local scale, boundary layer clouds are a forecasting challenge. Small differ-

ences in the boundary layer scheme can result in forecasts changing from completely clear to completely cloudy conditions (Martin et al., 2000). This impacts on surface temperatures and the timing and location of deep convection (Baldauf et al., 2011). The boundary layer parameterisation used can also have an impact on the prediction of tornadoes (Stensrud & Weiss, 2002), hurricanes (Powell, 1980) and floods (Zampieri et al., 2005).

Due to the importance of the boundary layer scheme there are many different formulations used in numerical weather prediction and climate models (e.g. first order closure with local/non-local diagnosis of diffusivity and prognostic TKE). There are also a great number of studies comparing and contrasting different schemes in different situations. Many of these are for a specific case study or short periods of time where observational data is available (Beesley et al., 2000; Betts & Jakob, 2002; Zhang & Zheng, 2004; Hu et al., 2010; Shin & Hong, 2011) or just use single column models (Cuxart et al., 2006; Svensson et al., 2011). These studies typically focus on near-surface variables, e.g. 2 m temperature and 10 winds, and boundary-layer height. There are a few studies of boundary layer cloud (e.g. Sengupta et al., 2004; Barrett et al., 2009) , however the new dataset of observed boundary-layer type provides an opportunity to do a more long term evaluation of the Met Office boundary layer parmameterisation. It is novel in that it brings together surface and above surface observations so the boundary layer and cloud schemes can be tested simultaneously. Finally, the method of boundary-layer type diagnosis presented in this thesis can be split down into five contributing processes, surface layer stability, presence of cumulus cloud, decoupling, number of cloud layers and presence of stratocumulus over a stable layer, which can be evaluated individually.

3.2 Datasets

3.2.1 Observational data

The observational boundary-layer type is diagnosed using data from a ground-based vertically pointing Doppler lidar and sonic anemometer located at the Chilbolton Facility for Atmospheric and Radio Research (CFARR), Hampshire as described in Chapter 2 and Harvey et al. (2013). This method gives probabilities for each of the nine boundary-layer types for each hour of available data. In the following model comparison only the boundary-layer types that are the most probable are considered. This is due to only

having instantaneous model boundary-layer types available to validate.

As described in Section 2.2, the algorithm divides the Met Office types I and III into sub-types Ia, Ib, Ic, IIIa and IIIb according to presence and nature of cloud. For the model comparison presented here these sub-types are re-grouped. This re-grouping is done as it was not possible to split the model data into the nine observational boundary-layer types, shown in Figure **??**, with the model data that was available. Also, the condensing of the types ensures a fair test of the model which does not apply different diffusivity profiles when cloud is present in types I and III.

Finally, the Met Office 4 km model only considers cloud to be cumulus if it is greater than 400 m thick (Lock & Edwards, 2011). This constraint ensures cumulus cloud is at least two model levels thick and mixing can occur within it. Therefore, in order to ensure a fair comparison, if cumulus cloud is diagnosed observationally (types V and VI) and is less than 400 m then it is re-classified as type III if originally diagnosed as type VI or type IV if originally diagnosed as type V. The cloud depth used for this reclassification is derived using the Cloudnet 'target classification' product (Illingworth et al., 2007). This uses radar and lidar co-located at Chilbolton to classify the targets in each radar-lidar pixel into a number of different categories. Examples of the categories are liquid cloud, ice cloud, snow, insects and aerosol. This classification can be used to calculate the mean cloud base and cloud top height for liquid clouds with a cloud base below 2 km for each hour, centred on the hour. The 2 km threshold is chosen as this is the height typically associated with mid-latitude boundary-layer height. Also, the model defines 3 km as the maximum height of the boundary layer. Only clouds detected by both the lidar and radar are used in this calculation as optically thick clouds only detected by the lidar may report an artificially low cloud-top height due to attenuation of the lidar beam. The difference between the mean cloud base and cloud top is then taken as the cloud depth. Days where radar data are not available have been removed from the following comparison. Figure 3.1 shows the distribution of two years (01/09/2009 - 31/08/2011) of cloud depths found using the 'Cloudnet' classification. By applying the 400 m cloud depth constraint that used in the model it could remove up to 69% of cumulus cloud.

3.2.2   Model data

The Met Office Unified Model (version 5.2 onwards) solves non-hydrostatic, deep-atmosphere dynamics using a semi-implicit, semi-Lagrangian numerical scheme (Cullen
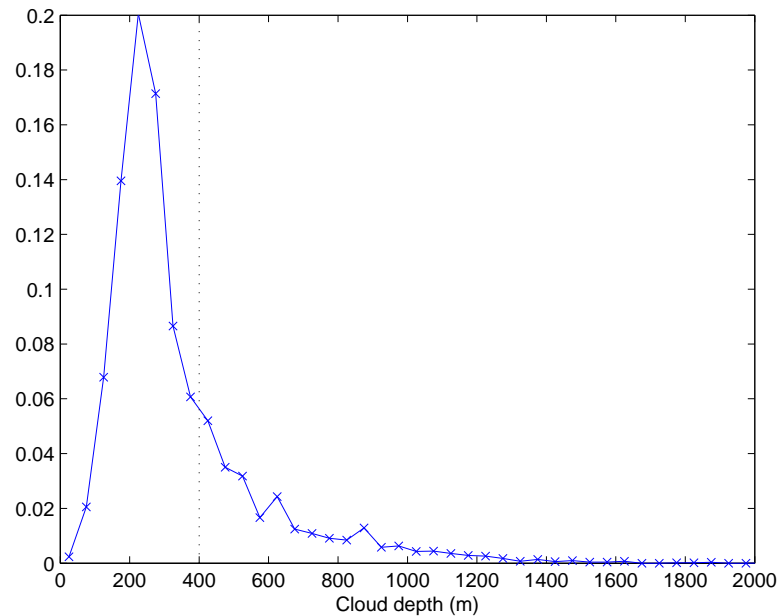
Figure 3.1: The distribution of observed cloud depths found using the 'Cloudnet' target classification method. The black dotted line shows the 400 m depth constraint applied to cumulus clouds in the Met Office Unified Model.

et al., 1997 and Davies et al., 2005). The model includes a comprehensive set of parameterisations, including surface (Essery et al., 2001, Best et al., 2011 and Clark et al., 2011), boundary layer (Lock et al., 2000), mixed-phase cloud microphysics (Wilson & Ballard, 1999) and radiation (Edwards & Slingo, 1996) schemes. The model also includes an option for convection parameterisation (Gregory & Rowntree, 1990) which is used in all resolutions greater than 4 km, with additional downdraught and momentum-transport parameterisations. The model runs on a rotated latitude/longitude horizontal grid with Arakawa C staggering and a terrain-following hybrid-height vertical coordinate with Charney-Philips staggering.

In the 4 km resolution version of the model (UK4), the convection parameterisation used is Gregory & Rowntree (1990) with a modification that restricts mass flux using a convective available potential energy (CAPE) closure timescale (Lean et al., 2008) and 3D-Var assimilation is used. There are 70 levels in the vertical up to the model top at 40 km. In order to increase the resolution in the boundary layer, the distribution of the levels near the ground is quadratic so, for example, there are 16 levels in the lowest 1 km of the atmosphere. This version of the model is used for the main comparison presented in Sections 3.3.1 - 3.3.2.2.

The North Atlantic European (NAE) version of the model has a 12 km horizontal resolu-

tion and a much coarser vertical resolution, 38 levels, with 7 levels in the lowest 1 km. It uses the standard Gregory & Rowntree (1990) scheme, diagnostic rain and 4D-Var data assimilation. This setup of the model is used to investigate the effect of horizontal resolution on the skill of the model predicting boundary-layer type.

The model data available for evaluation are hourly snapshots of boundary-layer type for the 9 closest grid points to CFARR. The forecasts are 36 hours long and are initialised at 03, 09, 15 and 21 UTC for the UK4 and 00, 06, 12 and 18 UTC for the NAE. UK4 data are available for the period 01/09/2009 - 31/08/2011. Data from the NAE model data are available from 01/09/2009 - 31/5/2010, a much shorter time period than the UK4. The availability of data at 9 grid points enables a comparison of the nearest grid point to the location of the Doppler lidar and a comparison to the modal boundary-layer type. Unstable shear-dominated boundary layer types (VII) cannot be diagnosed using the observational method. Hours where this type is diagnosed in the model have been combined with well mixed boundary layers (type III). All hours where model rain rate is above 0.02 mm hr^{-1} are removed from the analysis. This is to be consistent with the removal of observational boundary-layer types when it raining. This removes approximately 20% of the data, which is comparable to the percentage of data removed due to rain in the observational dataset (see Chapter 2).

3.3 Comparison of observational and model boundary-layer types

3.3.1 Climatology

Before examining the skill of the UK4 model in predicting boundary-layer type at the correct time, the ability to reproduce the observed climatology of boundary-layer type is assessed. Figure 3.2 shows the overall distribution of boundary-layer types for the closest model grid point to Chilbolton with a forecast lead time of 0–5 hours (the first six hours of each forecast that is have available) and observations with and without the cumulus cloud constraint applied for two years of data, 01/09/2009 - 31/08/2011. There is good agreement between the model and observations for stable types (I and II), but there is less agreement for the unstable types. The model predicts more decoupled stratocumulus (IV) and decoupled stratocumulus over cumulus (V) than the observations but less well mixed (III) and cumulus without depth constraint (VI). When the cumulus

cloud constraint is applied to the observational data the discrepancy between the model and observations increases for well mixed (III) and stratocumulus over cumulus (V), reduces slightly for decoupled stratocumulus (IV) and changes sign for cumulus-capped boundary layers (IV). The application of the cumulus cloud constraint, by definition, does not affect the fraction of stable boundary-layer types observed.

The distribution of boundary-layer type can also be analysed as function of season, as shown in Figure 3.3. In both the model and observations more stable types (I and II) are diagnosed in the cold seasons than the warm seasons, more cumulus types (V and VI) are diagnosed in the warm seasons than the cold seasons and decoupled stratocumulus over cumulus (type V) is rare compared to other types. The model diagnoses more decoupled stratocumulus (types II and IV) in both the stable and unstable regime than the observations in all seasons except type II in winter (DJF). Decoupled stratocumulus is least common in DJF in the model and observations. When the cumulus cloud constraint is applied the same pattern of discrepancy seen in Figure 3.2 is also seen in each season.

Figure 3.4 shows the diurnal distribution of the most probable observational boundary-
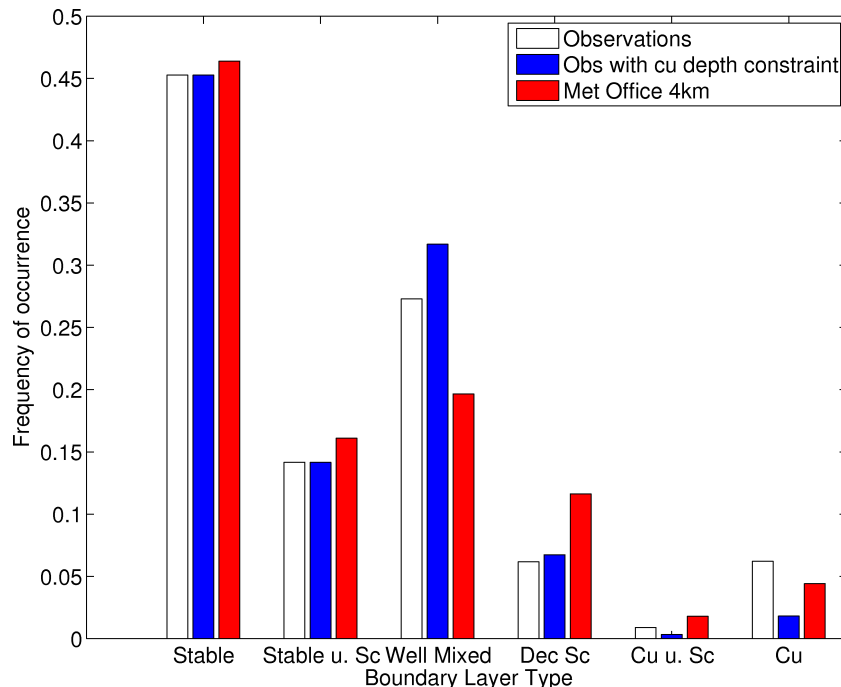
Figure 3.2: The overall distribution of boundary-layer types for the most probable boundary-layer type with and without the cumulus depth constraint and the Met Office 4 km model grid point closest to Chilbolton with lead time of 0–5 hours. Thus the blue bars indicate the observations process in a way most comparable with the model assumptions, but the white bars are closer to the "true" distribution with shallow cumulus clouds.
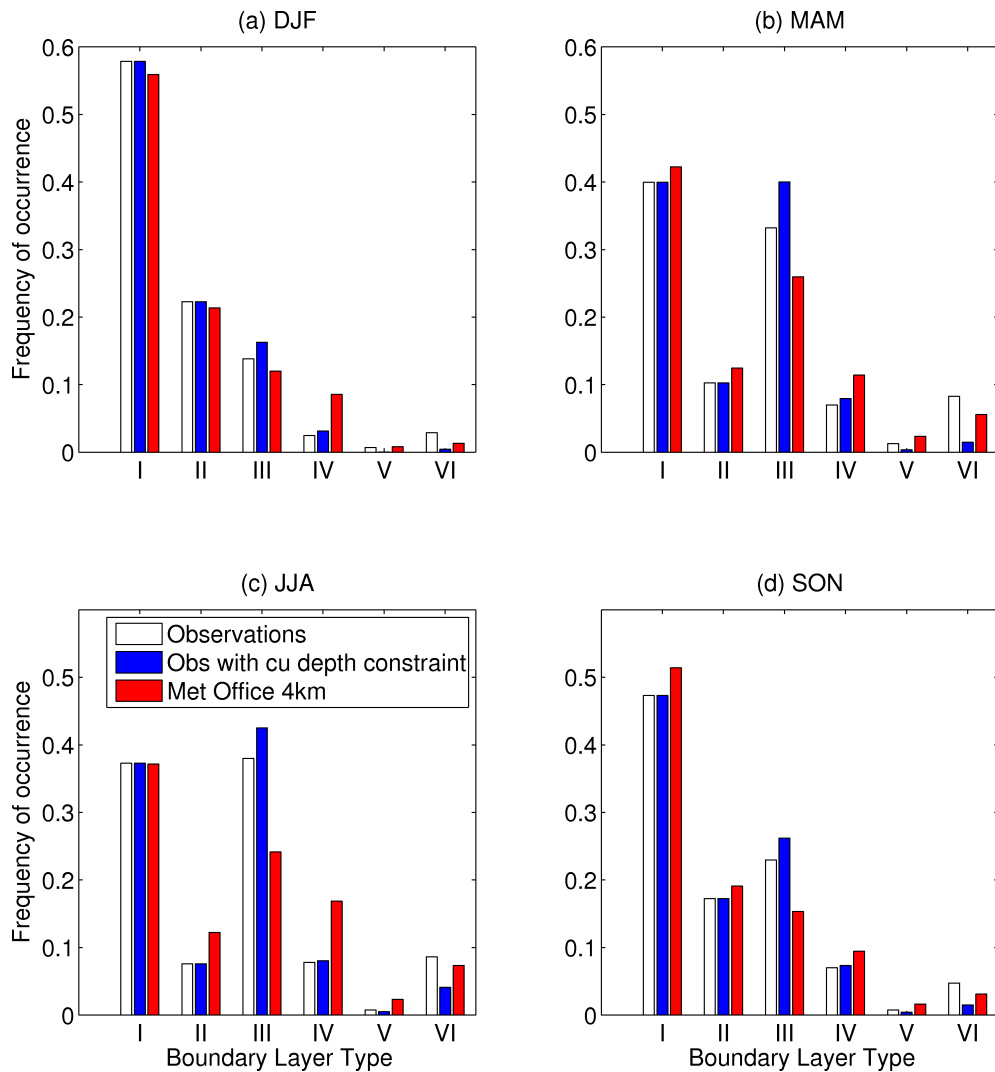
Figure 3.3: The overall distribution of boundary-layer types as a function of season (a) winter (DJF), (b) spring (MAM), (c) summer (JJA), (d) autumn (SON) for the most probable boundary-layer type with and without the cumulus depth constraint and the Met Office 4 km model grid point closest to Chilbolton with lead time of 0–5 hours. Thus the blue bars indicate the observations processed in a way most compatible with the model assumptions, but white is closer to the "true" distribution with shallow cumulus clouds

layer type and the Met Office 4 km forecast with a lead time of 0–5 hours as a function of season. A clear seasonal and diurnal cycle is present in both the model and observations. As expected more stable types are diagnosed in the cold seasons. The length of time that unstable types dominate is longer in the warm seasons. More unstable types are diagnosed at night in the observations except during DJF when more unstable types are diagnosed at night in the model. Decoupled stratocumulus cloud is more likely to be present in the morning, before 1200 UTC, in the model but it is more common in the afternoon, after 1200 UTC, in the observations. The difference made by applying the cumulus thickness constraint to the observations is shown in yellow. This again highlights the removal of the majority of the observationally diagnosed cumulus-capped bound-

ary layers when this constraint is applied. Although there are differences between the two datasets, overall they do have similar distributions, which gives confidence when comparing the two data sets using other measures.

3.3.2 Verification methods

Here the model skill at predicting the correct boundary-layer type at the correct time is assessed using verification measures derived from the joint histogram of model and observations. For binary events this problem has a long history dating back to Finley (1884) but more recently similar techniques have previously been used by Hogan et al. (2009b) and Mittermaier (2012) to evaluate the model cloud properties. Figure 3.5 shows an example of a joint histogram for forecast lead time of 0–5 hours for the closest model grid point to Chilbolton. The main panel is a contingency table showing how many times each combination of observed and modelled boundary-layer type occurs. It shows that rather than all of the data lying along the diagonal, which would be expected for a perfect forecast, there is a large spread. Also shown are the histograms from observations and
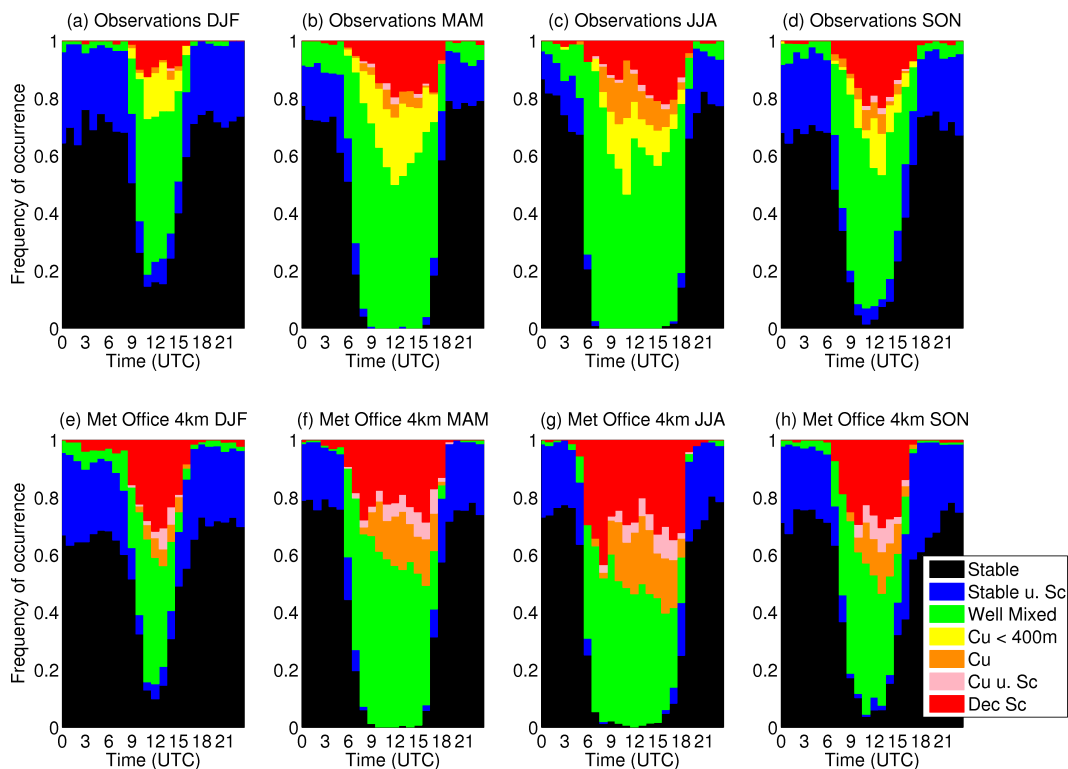
Figure 3.4: The diurnal distribution of the most probable observational boundary-layer type as a function of season (a) winter, (b) spring, (c) summer, (d) autumn. The diurnal distribution of the Met Office 4 km forecast boundary-layer type for a lead time of 0–5 hours as a function of season (e) winter, (f) spring,(g) summer, (h) autumn.
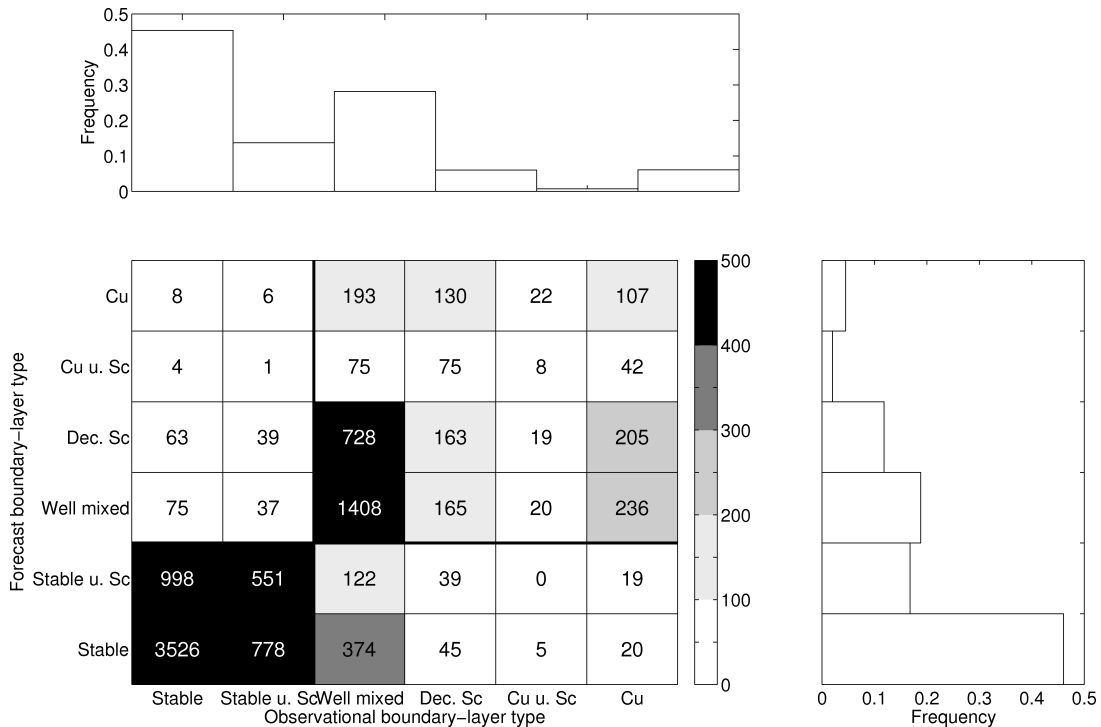
Figure 3.5: The main (lower left) panel shows the joint histogram of the most common boundary-layer type derived from observations and the Met Office 4 km model forecast of boundary-layer type with a lead time of 0–5 hours for the closest grid point to Chilbolton. The panels to the top and right show the probability distribution of observed and modelled boundary-layer type. The cumulus cloud constraint has not been applied to the observational data.

model separately. The histograms were computed for both the boundary-layer type at the closest model grid point to Chilbolton and the modal boundary-layer type calculated from the nine closest grid points to Chilbolton for model lead times 0–5 hours, 6–11 hours, 12–17 hours, 18–23 hours, 24–29 hours, 30–36 hours. As the observations used hour-averaged values to determine boundary-layer type it is assumed that advection over time is the same as instantaneous spatial variability as in Barnett et al. (1998) and therefore it can be directly compared to instantaneous model grid-box values.

It is is difficult to evaluate the entire joint probability distribution function of the boundary-layer types. Many verification measures, e.g. odds ratio (Stephenson, 2000), cannot be generalised simply to more than 2 categories and signal detection methods result in multiple relative operating characteristic diagrams that are hard to visualise and interpret Livezey (2012). Here a simpler approach is to split up the joint histogram into a contingency table simply by dividing it into four quadrants based on a decision made in the observational diagnosis of boundary-layer type. In this case there are five decisions that can be assessed. The decisions are described in Table 3.1. Figure 3.6 shows how each the contingency table is split up for each decision. For the case shown in Figure 3.5, the

contingency table for stability (decision 1) is

$$\begin{pmatrix} a & b \\ c & d \end{pmatrix} = \begin{pmatrix} 5853 & 624 \\ 233 & 3596 \end{pmatrix}.$$

(3.1)

There are many verification measures that can be used to assess model performance in predicting binary events (Wilks, 1995; Von Storch & Zwiers, 1999; Casati et al., 2008; Hogan et al., 2009b; Hogan & Mason, 2012). Here the Symmetric Extremal Dependence Index (SEDI) is considered (Ferro & Stephenson, 2011). This measure was chosen as it has many desirable properties. It is equitable meaning that all random forecasting systems will receive the same expected score. It is difficult to hedge and therefore cannot be influenced by issuing a forecast that is not the true judgment of the forecaster. Many verification measures tend to meaningless values for rare events the SEDI measure is
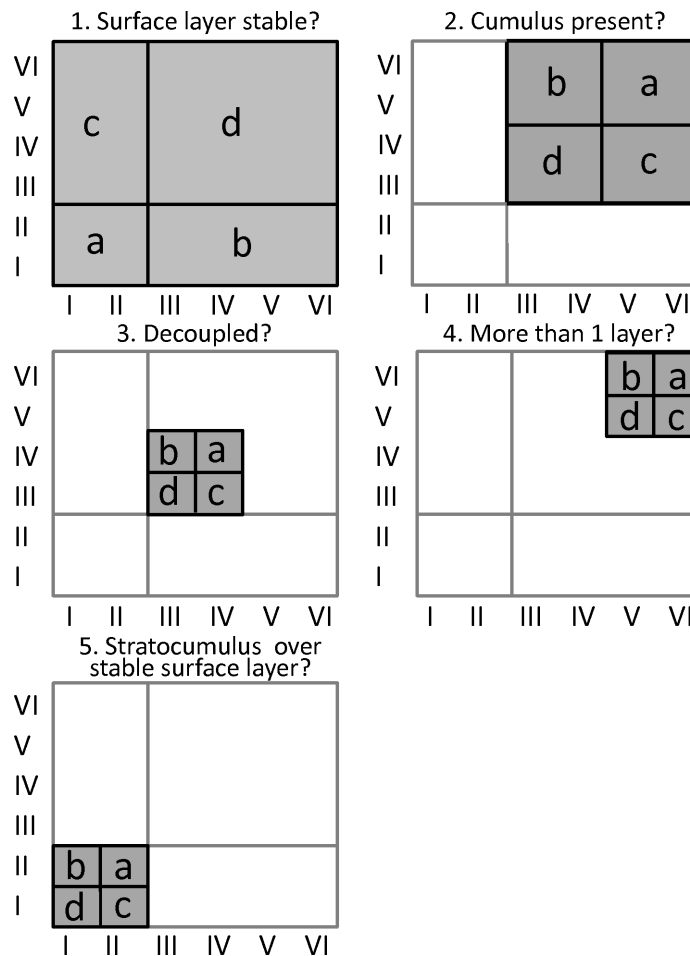
Figure 3.6: Schematic of how the joint histogram in Figure 3.5 is split into multiple 2x2 contingency tables corresponding to each decision. The number refers to the decision being considered (as in Table 3.1). Abscissa refers to the observed boundary-layer type and ordinate to the modelled type.

Table 3.1: Summary of decisions that are assessed using a binary verification measures.

Decision	Description	Types
1	Surface layer stable or unstable	I and II vs. III, IV, V and VI
2	Cumulus cloud present or not present	V and VI vs. III and IV
3	Decoupled or coupled	IV vs. III
4	More than 1 cloud layer when cumulus cloud present	VI vs. V
5	Stable stratocumulus present or not present	II vs. I

independent of the frequency of occurrence of an event and therefore can be used for rare events. A SEDI value of 1 indicates perfect forecasting skill whereas a value of 0 indicates no more skill than a random forecast.

Equation 3.2 shows the mathematical form of SEDI, where H is the hit rate ($H = a/(a + c)$) and F is the false-alarm rate ($F = b/(b + d)$).

$$\text{SEDI} = \frac{\ln F - \ln H + \ln(1 - H) - \ln(1 - F)}{\ln F + \ln H + \ln(1 - H) + \ln(1 - F)} \tag{3.2}$$

3.3.2.1 Dependence of skill on forecast lead time

The SEDI score was calculated for all decisions and forecast lead times 0–5 hours, 6–11 hours, 12–17 hours, 18–23 hours, 24–29 hours and 30–36 hours for the period 01/09/2009 - 31/08/2011 for the most probable boundary-layer type at the grid point closest to Chilbolton and the modal boundary-layer type taken from the 9 closest grid points to Chilbolton. It was also calculated for the observational climatology and 24 hour persistence forecast (i.e. the boundary-layer types forecast today are the same as those forecast yesterday).

Figure 3.7 shows the performance of the Met Office 4 km model as a forecast lead time for each of the decisions outlined in Table 3.1 without the cumulus depth constraint applied. The error bars shown are calculated firstly by scaling the elements *a-d* by the number of independent events for each decision divided by the number of that event as done by (Hogan et al., 2009b). The number of independent events are estimated by determining how many times there is a transition to a different boundary-layer type. For example, the sequence 1 1 1 1 1 would be one event but 1 3 3 2 2 would be three events. The scaling is applied as the error variance assumes that each event is independent, which is not true in the case of boundary-layer type. These scaled coefficients are then used to calculate the SEDI error variance, S_{err}, using Equation 3.3 (Jolliffe & Stephenson, 2012) where the
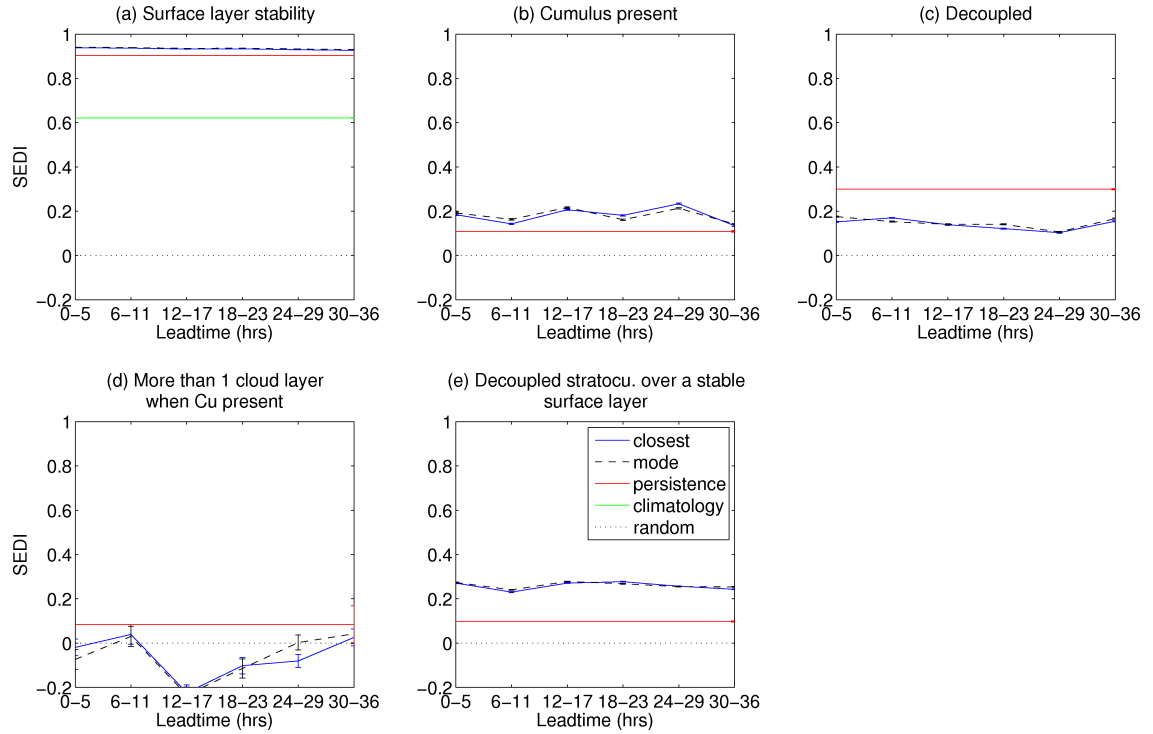
Figure 3.7: Plot of SEDI versus forecast lead time for decisions 1 - 5 (Table 3.1). The solid blue line indicates SEDI for the closest grid point to Chilbolton, the dashed black line represents the SEDI for the modal boundary-layer type for the 9 closest model grid points to Chilbolton, the red line indicates a persistence forecast, the dotted black line indicates a random forecast and the green line, Figure 3.7a only, a climatological forecast. The error bars are found using the SEDI variance scaled by the number of independent events for each decision.

error variances of H and F are $S_H^2 = H(1-H)/(a+c)$ and $S_F^2 = F(1-F)/(b+d)$, leading to

$$S_{err}^2 = \frac{S_H^2 \left[\frac{\text{SEDI}(1-2H)+1}{H(1-H)}\right]^2 + S_F^2 \left[\frac{\text{SEDI}(1-2F)+1}{F(1-F)}\right]^2}{[\ln F + \ln H + \ln(1-H) + \ln(1-F)]^2}. \tag{3.3}$$

The highest value of skill, 0.933, is for the stability decision (Figure 3.7). Skill is greater than both the climatology and persistence values and remains high for all lead times. The cumulus and stable stratocumulus decisions remain above persistence for all lead times (Figure 3.7b and e), persistence has a much lower value ($\sim$0.4) for these decision than for the stability decision ($\sim$0.9). The decoupled decision is significantly poorer than persistence at any lead time (Figure 3.7c). The sharp decrease in SEDI between the stability and cloud related decisions is probably related to the fact it is fundamentally more difficult to predict cloud related variables due their sensitivity to subtle changes in thermodynamic profiles. This hypothesis is supported by Hogan et al. (2009b) who found that the Met Office 12 km NAE systematically under predicted cloud fractions greater than 5% in the lowest 5 km of the atmosphere. The lowest values of SEDI are for the 2 layer cloud decision (Figure 3.7c), which is not better than random. Although

skill appears to increase with model lead time, it is possible that this increase is not statistically significant. Another method of assessing a different aspect of performance of a weather forecast is calculate its 'half-life' (Hogan et al., 2009a). However it cannot be calculated here as decisions 2, 3, 4 and 5 appear to have a cycle in them but have no systematic decrease with forecast lead time. Also, the skill of the decision relating to stability does not decrease a significant amount over the forecast lead times available. To properly assess forecast half-life data from longer forecast runs would be required.

Figure 3.8 summarises the skill for all forecast lead times combined for each of the decisions in Table 3.1 for the closest grid point to Chilbolton and the modal boundary-layer type from the 9 closest grid points with its associated error compared to the climatology and persistence. Here the error is the 95% confidence interval, CI, is estimated from the root mean square (RMS) deviation of the detrended time series of SEDI score versus forecast lead time, σ, and the number of forecast lead times used, N, in the following way

$$CI = \pm 1.96 \frac{\sigma}{\sqrt{(N-2)}}. \tag{3.4}$$
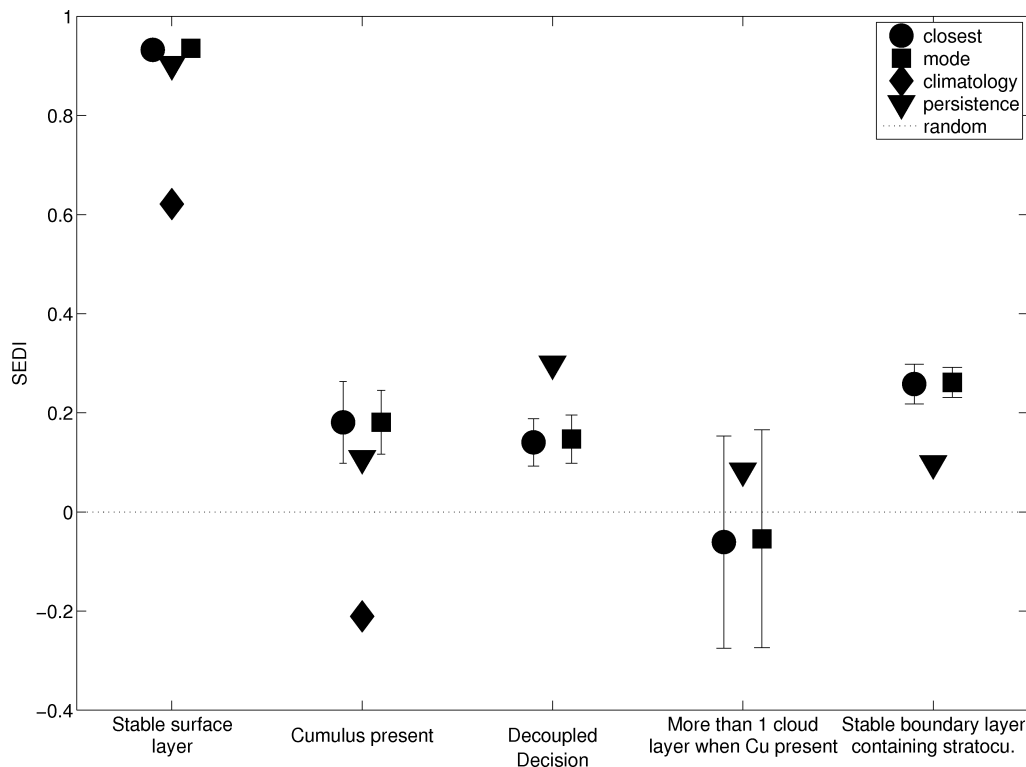
Figure 3.8: Summary of the SEDI score for each decision for the the modal 4 km boundary-layer type and 4 km boundary-layer type closest to Chilbolton with 95% confidence intervals calculated using the forecast lead time data.

This has can be done as each forecast is an alternative realisations of the same period and there is no systematic degradation of the forecast with lead time (shown in Figure 3.7).

3.3.2.2 Dependence of skill on season

The same analysis as described in Section 3.3.2.1 has been applied to each season within the 2 year dataset.
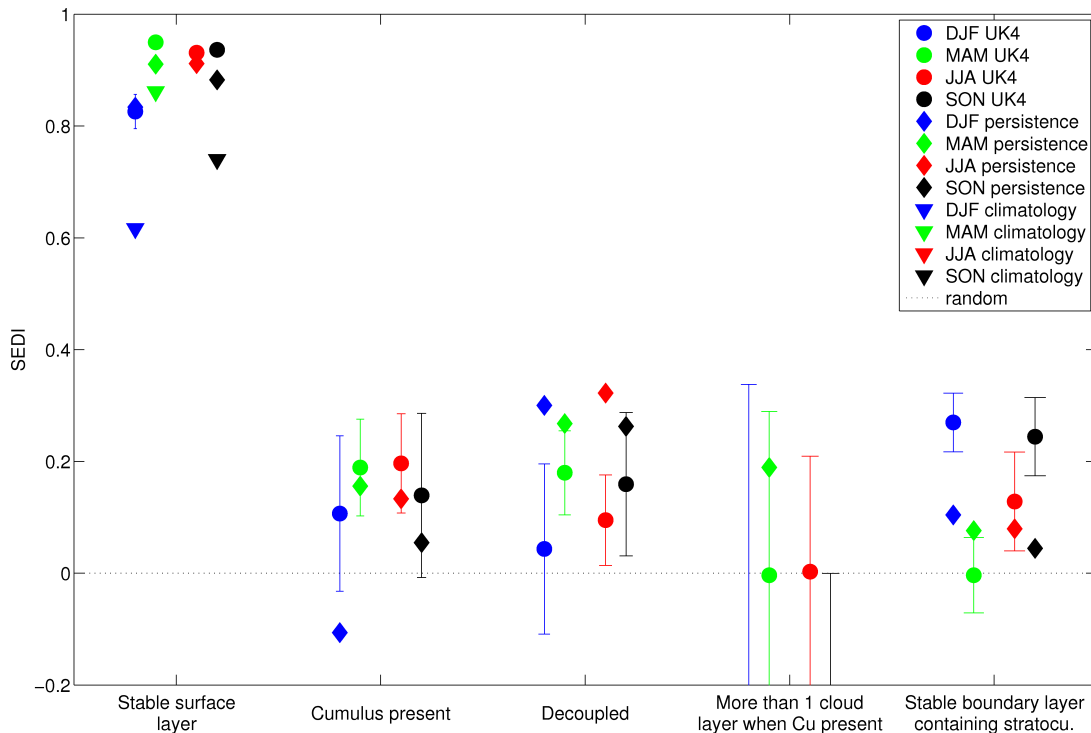
Figure 3.9: Summary of the SEDI score split by season for each decision for the the modal 4 km boundary-layer type and 4 km boundary-layer type closest to Chilbolton with 95% confidence intervals calculated using the forecast lead time data.

Figure 3.9 summarises the SEDI score for each decision for each season for the closest model grid point to the Chilbolton. In winter most unstable decisions (2–5) are predicted with less skill than in all other seasons. The stable stratocumulus decision is more skillful than other seasons. The stability decision has the lowest skill in this season. Observationally it is seen that during winter sensible heat flux can remain close to zero throughout the day this can make it difficult for the model to predict when the transition from stable to unstable occurs. Spring (MAM) has the highest SEDI scores for stability, decoupled and stratocumulus over a stable layer. Summer (JJA) has the highest score for the presence of cumulus and cloud layers.

Figures 3.10 - 3.13 show the behaviour of each decision as a function of lead time for

each season. In all seasons the most skillful decision is the stability decision. During winter, SEDI drops below persistence for lead times greater than 12 hours. This is the only instance of this occurring for the stability decision. The behavior of the SEDI score is broadly the same for the cumulus decision for all seasons and thus the behaviour of the whole dataset. All seasons have a SEDI below persistence for the decoupled decision and during the winter, for short lead times, it is not significantly better than a random forecast. The layers decision, as in the combined results for all seasons, has a worse than random SEDI in all seasons. The stable stratocumulus decision is significantly greater than persistence for all seasons except summer. During summer, for short lead times, the skill is not significantly greater than persistence and it appears to increase with forecast lead time.
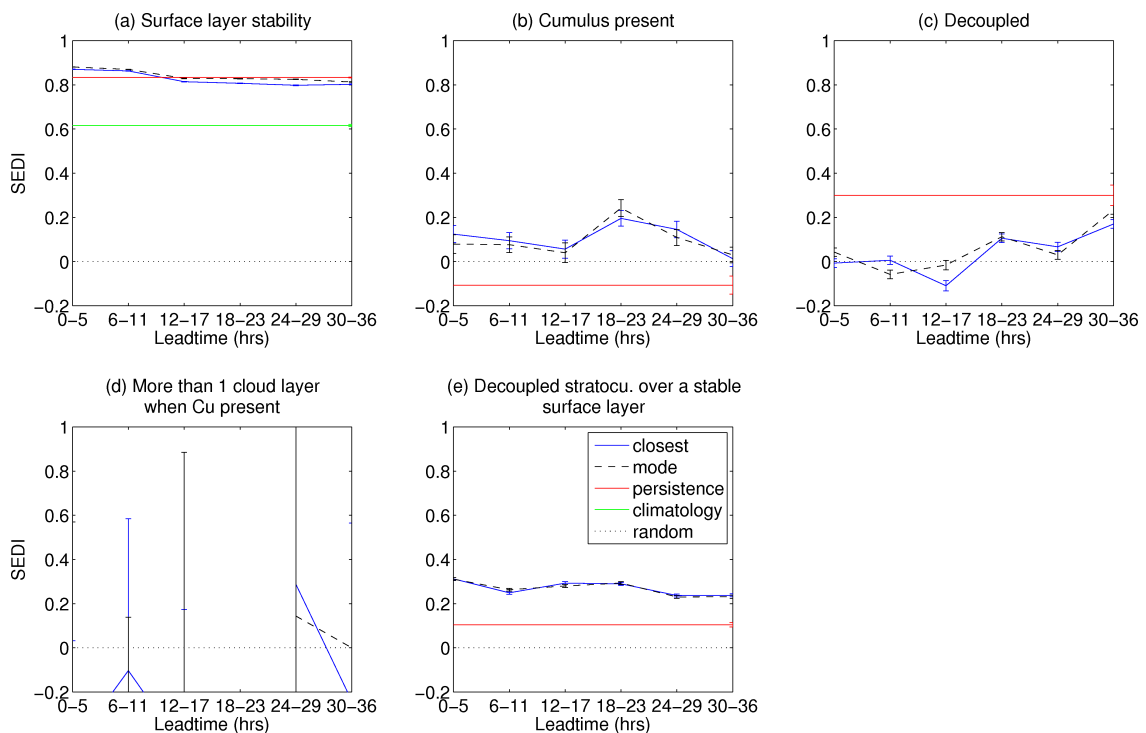
Figure 3.10: Plot of SEDI versus forecast lead time for decisions 1 - 5 for December, January and February (DJF) only. The solid blue line indicated SEDI for the closest grid point to Chilbolton, the dashed black line represents the SEDI for the modal boundary-layer type for the 9 closest model grid points to Chilbolton, the red line indicates a persistence forecast and the green line a climatological forecast. The error bars are found using the SEDI variance scaled by the number of independent events for each decision.

3.3.2.3 Dependence of skill on model resolution

The effect of model resolution is investigated by using another model in the operational suite of the UK Met Office. Here the 12 km NAE is used, however the due to availability
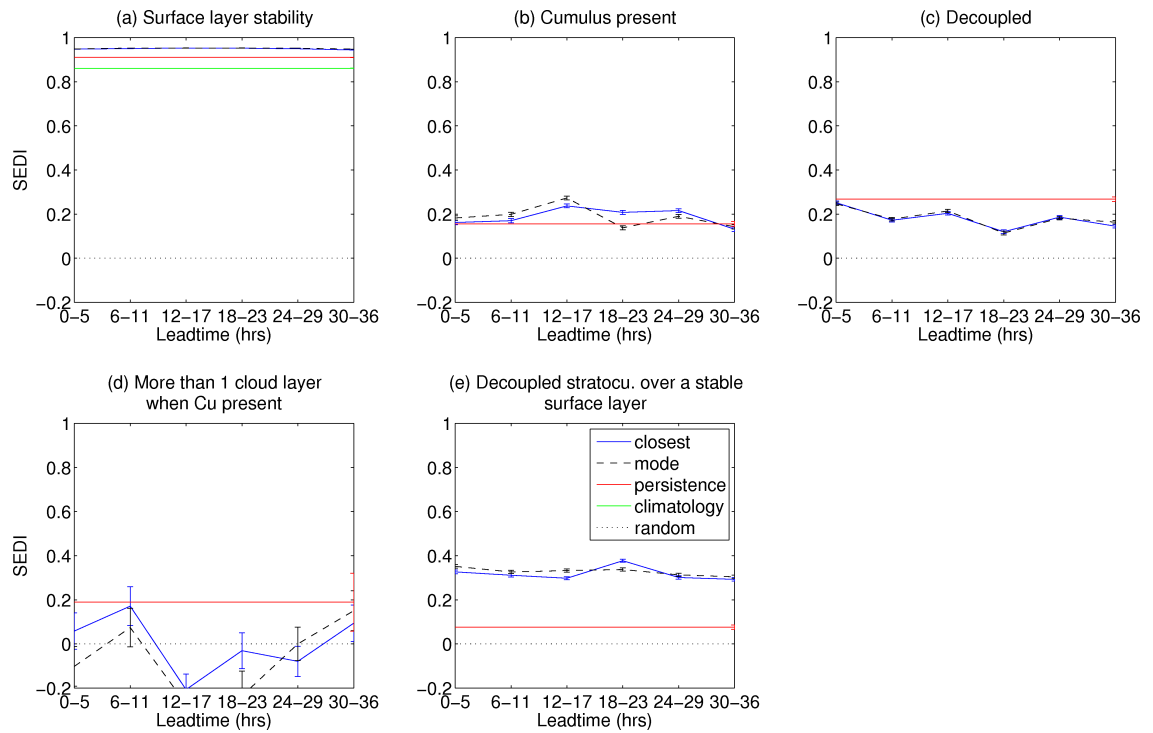
Figure 3.11: As Figure 3.10 but for March, April and May (MAM) only.
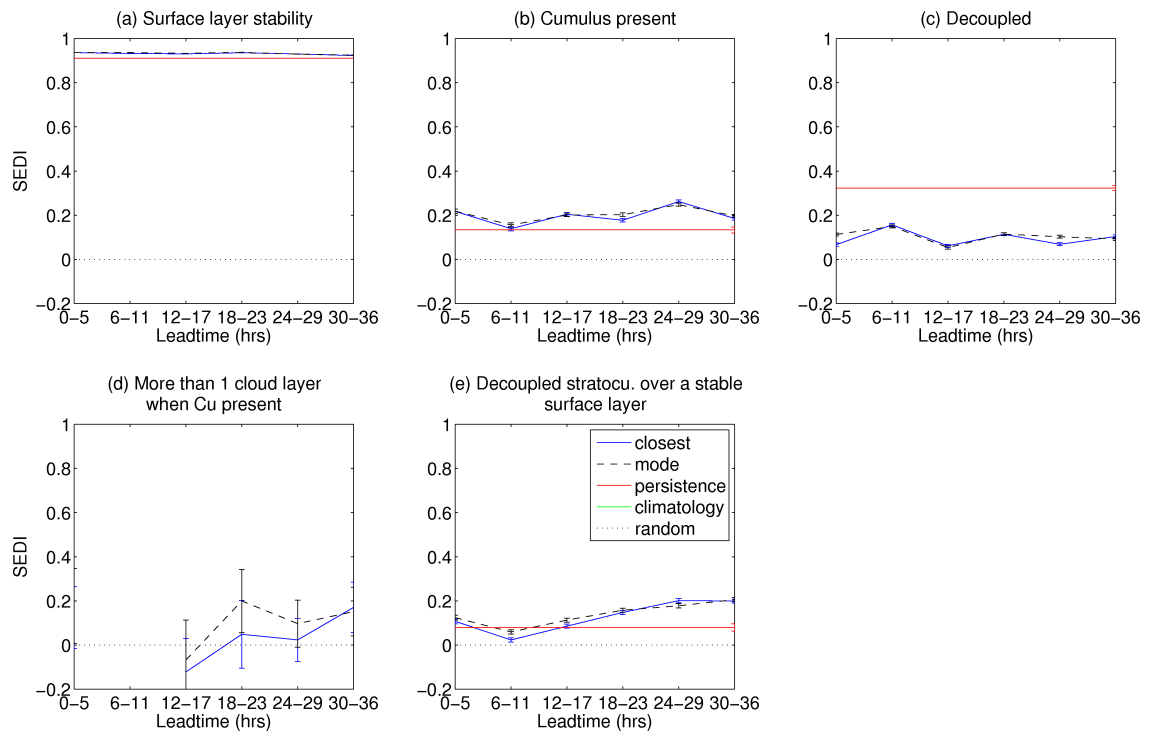
Figure 3.12: As Figure 3.10 but for June, July and August (JJA) only.

of data only the period 01/09/2009 - 31/5/2010 can be considered.

Figure 3.14 shows the overall distribution of boundary-layer types for the observations,
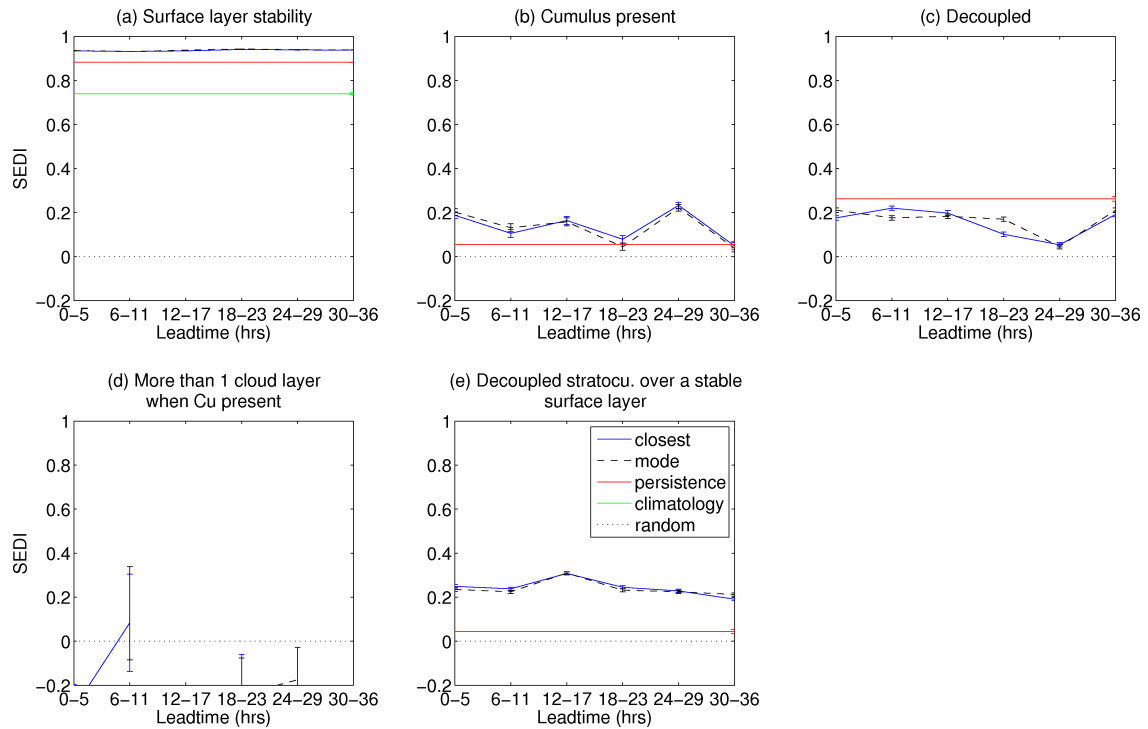
Figure 3.13: As Figure 3.13 but for September, October and November (SON) only.

4 km model and 12 km NAE model for the period 01/09/2009 - 31/5/2010. As before the observations and 4 km model agree reasonably well for the stable boundary-layer types (I and II) but there is a much greater discrepancy for the 12 km NAE model. It has a much greater frequency of occurrence of stable boundary-layer type I than the other data sets. This is compensated by a lower frequency of occurrence of stable under stratocumulus (type II). This difference is consistent with the impact of the vertical resolution of the Met Office global model increasing from 50 to 70 levels (A. Lock, personal communication). As the resolution increases the grid boxes become smaller and thus it is easier to have a larger cloud fraction resulting in more boundary layers diagnosed as cloudy (a cloud fraction greater than 0.1 is required for a grid box to be considered cloudy in the model).

The 12 km NAE model also diagnoses cumulus types (V and IV) much less frequently than the UK4. This low frequency of cumulus types matches very well the observations with the cumulus cloud constraint applied but the 4 km models matches more closely to the unconstrained observations. The decrease in occurrence of cumulus types in the 12 km model is compensated by an increase in the number of well mixed boundary-layer types diagnosed. The occurrence of decoupled stratocumulus cloud is very similar in all data sets.

The SEDI score has been calculated for each of the decisions described in Section 3.3.2.1
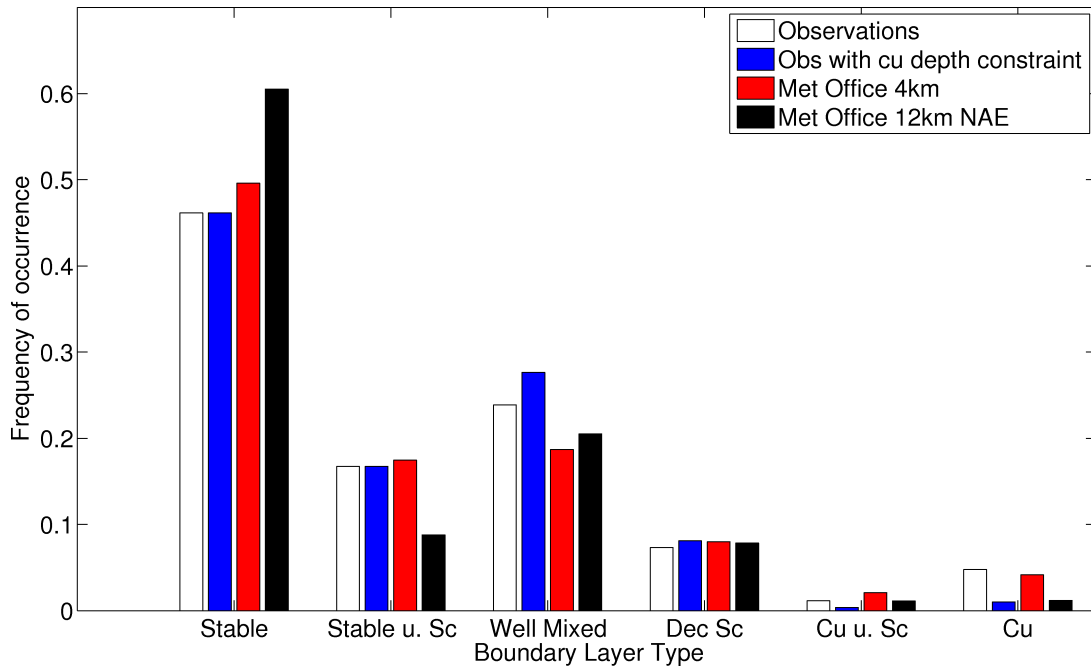
Figure 3.14: The overall distribution of boundary-layer types for the most probable boundary-layer type with and without the cumulus depth constraint and the Met Office 4 km and 12 km NAE models for the grid point closest to Chilbolton with a lead time of 0–5 hours for the period 01/09/2009 - 31/05/2010

using all forecast lead times. A comparison to the skill of the modal boundary-layer type from the 4 km model is shown in Figure 3.15. As in the analysis of the larger dataset the highest value of skill is for the stability decision. Within the 95% confidence intervals shown there is no significant difference in skill as model resolution increases from 12 km to 4 km. This is true for all the decisions considered. This is not surprising as the model parameterisations used have not changed as model resolution has increased. This is supported by Mittermaier (2012) who could not draw any conclusion about the impact of horizontal resolution on the Symmetric Extreme Dependency Score (SEDS) of cloud base height and total cloud amount in the 12 km NAE, 4 km and UKV (1.5 km resolution) versions of the Met Office model. Conversely, Lean et al. (2008) found that increasing horizontal resolution increased Fractions Skill Score (FFS) of precipitation events over the UK for a forecast lead time of 6 hours. Small differences in skill as model resolution increases were also seen in the NCEP Eta model by Mass et al. (2002). They found that more realistic mesoscale structures and evolution was seen in the model as the was resolution increased from 36 km to 12 km. This gave improvements in precipitation amount, 10m winds, 2 m temperature and surface pressure. However there was not much impact on skill as the resolution was further increased from 12 km to 4 km.

Also shown in Figure 3.15 is the SEDI score for the presence of low cloud (below 3km).

This score is significantly higher than all of the cloud decisions related to boundary-layer type. This suggests that although the model does a reasonable job of predicting low cloud it does not predict the correct type of cloud. In turn this suggests that cloud presence may be controlled by the large scale humidity field, not local mixing.

3.4 Most likely sequences of boundary layer type

By taking the boundary-layer type at five representative times throughout the day it is possible to find the most common sequences of boundary layer type. As in Chapter 2, the representative times chosen are 0300, 0900, 1200, 1500, 2100 UTC and boundary-layer type data must be available for all hours to be considered in the following analysis. As in Chapter 2, all hours with rain observed are removed. Also, to ensure a fair comparison to the model observed types Ia, Ib, Ic have been combined into a single type I and types IIIa and IIIb have been combined into type III. Note the following analysis is only applied to the Met Office 4 km model with raining hours removed.

Table 3.2 shows the 20 most common observational boundary-layer type transitions. The
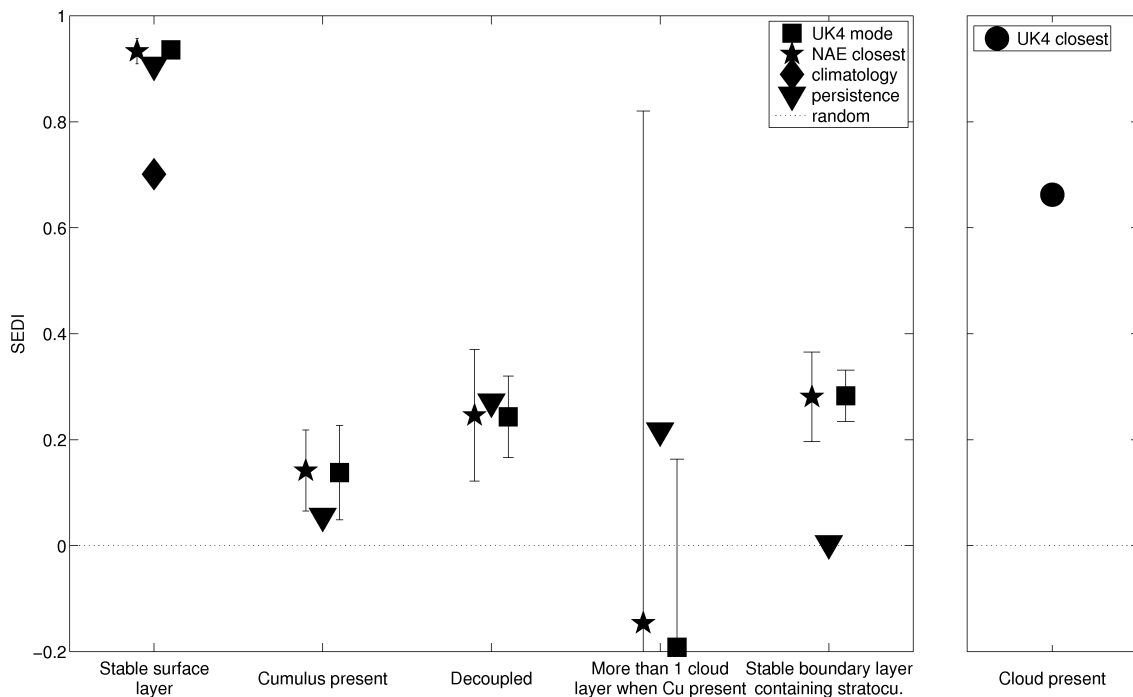
Figure 3.15: Summary of the SEDI score for each decision for the the modal 4 km boundary-layer type and 12 km NAE boundary-layer type closest to Chilbolton with 95% confidence intervals calculated using the forecast lead time data for the period 01/09/2009 - 31/05/2010. The right panel shows the SEDI score for the presence of cloud below 3 km for the same period for the 4 km resolution of the model for the closest grid point to Chilbolton.

most common boundary-layer type transition is that of stable to well mixed (with or without stratocumulus cloud) then back to stable. This transition pattern occurs 23.1% of the time in the observations. This is also the most common model boundary-layer type transition (shown in Table 3.3) but with a much greater frequency (41.3%). This implies that the sequences are more diverse in the observations than in the model. This is supported by the percentage of time that the top 20 sequences include, 84.7% for the model and 74.3% for the observations.

Table 3.2: Most common **observational boundary-layer type evolutions with no cumulus constraint applied.**

Time of Day					Occurrence	
03:00	09:00	12:00	15:00	21:00	percentage of time	number of days
Stable	Well mixed	Well mixed	Well mixed	Stable	23.1	57
Stable	Well mixed	Cumulus	Well mixed	Stable	8.1	20
Stable u. Sc	Well mixed	Well mixed	Stable	Stable	6.1	15
Stable	Well mixed	Well mixed	Well mixed	Stable u. Sc	4.9	12
Well mixed	Well mixed	Well mixed	Well mixed	Stable	4.9	12
Stable	Well mixed	Cumulus	Cumulus	Stable	4.0	10
Stable	Cumulus	Well mixed	Stable	Stable	3.2	8
Stable	Cumulus	Cumulus	Cumulus	Stable	2.4	6
Stable	Stable	Well mixed	Stable	Stable	2.0	5
Stable	Well mixed	Well mixed	Cumulus	Stable	2.0	5
Stable u. Sc	Cumulus	Well mixed	Well mixed	Stable	2.0	5
Stable	Well mixed	Well mixed	Well mixed	Well mixed	1.6	4
Stable	Well mixed	Cumulus	Cumulus	Stable u. Sc	1.6	4
Stable	Stable	Well mixed	Well mixed	Stable	1.2	3
Stable	Well mixed	Well mixed	Cumulus	Stable u. Sc	1.2	3
Stable	Well mixed	Cu u. Sc	Well mixed	Stable	1.2	3
Stable	Cumulus	Well mixed	Well mixed	Stable u. Sc	1.2	3
Stable	Cumulus	Cumulus	Well mixed	Stable	1.2	3
Stable u. Sc	Well mixed	Well mixed	Cumulus	Stable	1.2	3
Stable u. Sc	Well mixed	Cumulus	Well mixed	Stable	1.2	3

Table 3.3: Most common **4 km model boundary-layer type evolutions.**

Time of Day					Occurrence	
03:00	09:00	12:00	15:00	21:00	percentage of time	number of days
Stable	Well mixed	Well mixed	Well mixed	Stable	41.3	90
Stable	Well mixed	Well mixed	Well mixed	Stable u. Sc	12.8	28
Stable u. Sc	Well mixed	Well mixed	Well mixed	Stable	4.6	10
Stable	Stable	Well mixed	Stable	Stable	4.1	9
Stable	Well mixed	Well mixed	Stable	Stable	2.3	5
Stable u. Sc	Well mixed	Well mixed	Well mixed	Stable u. Sc	2.3	5
Stable	Stable	Well mixed	Stable u. Sc	Stable	1.8	4
Stable	Well mixed	Well mixed	Stable	Stable u. Sc	1.8	4
Stable	Well mixed	Well mixed	Cu u. Sc	Stable	1.8	4
Stable	Well mixed	Well mixed	Cumulus	Stable	1.4	3
Stable	Well mixed	Cumulus	Well mixed	Stable	1.4	3
Stable u. Sc	Well mixed	Well mixed	Stable	Stable	1.4	3
Well mixed	Well mixed	Well mixed	Stable u. Sc	Stable	1.4	3
Stable	Stable	Well mixed	Stable	Stable u. Sc	0.9	2
Stable	Stable u. Sc	Well mixed	Stable	Stable	0.9	2
Stable	Well mixed	Well mixed	Well mixed	Well mixed	0.9	2
Stable	Well mixed	Well mixed	Cumulus	Stable u. Sc	0.9	2
Stable	Well mixed	Cumulus	Stable u. Sc	Stable	0.9	2
Stable	Well mixed	Cumulus	Well mixed	Stable u. Sc	0.9	2
Stable	Well mixed	Cumulus	Cu u. Sc	Stable	0.9	2

Cumulus cloud is present in more of the observational transitions than the model transitions. It occurs in twelve of the top twenty observed diurnal transitions, 25.3% of the time, including the second most common transitions. This compares to only 5% in the model transitions. Cumulus cloud is also more persistent in the observations with 9.2% of the dataset having cumulus cloud that persists for two or more adjacent periods of observation that are considered here. Cumulus cloud is present in the morning in the observations. This is also shown in the diurnal distribution of boundary-layer types (Figure 3.4) where there is a greater occurrence of cumulus-capped boundary layers in the morning in the observations than the model in all seasons. There is not one model sequence in Table 3.3 where cumulus cloud occurs in the morning, the first instance is at 1200 UTC. Cumulus under stratocumulus only appears in the sequence ranked 16 in the observations, 1.2% of the time. But sequences with this type in are more than twice as common in the model (2.7%).

Decoupled stratocumulus is not present in any of the transition patterns in either the model or observations. This is surprising as it is the second most common unstable boundary-layer type in the model and third most common in the observations. However, decoupled stratocumulus over a stable layer is common in both the model (24.2%) and observations (19.4%). It is also interesting to note that it occurs in the afternoon in the model but at midday in the observations.

Well mixed boundary layer types are seen during the night in both the model and observations. These are occasions where although the sun has set sensible heat flux is still positive. This occurs more frequently in the observations (6.5%) than the model (2.3%).

The results presented here are largely invariant to the choice of start time although the time of sunrise and sunset will have an impact time of the transition from stable to unstable and vice-versa.

3.5 Conclusions

This chapter has evaluated the skill of the UK Met Office 4 km and 12 km models at predicting boundary-layer type. Firstly the climatology of boundary-layer type has been compared. Although there are some differences, notably the prevalence of decoupled stratocumulus cloud and lack of cumulus cloud in the model, the seasonal and diurnal cycles seen in the model and observations are not dissimilar. Overall, the most common

boundary-layer type in both the model and observations is stable, type I, followed by well mixed, type III.

Contingency tables have been used to assess model forecasts of boundary-layer type at the correct time. Although there is a spread in the stable and unstable quadrants of these tables there is good distinction between the two stability regimes. These have then been used calculate the SEDI for the decisions made to diagnose boundary layer type. These decisions are stability, presence of cumulus cloud, presence of decoupled stratocumulus, presence of more than one layer of cloud and presence of decoupled stratocumulus cloud over a stable surface. The decision with the highest skill is stability. This is true for all forecast lead times, seasons and resolutions. The cumulus decision is significantly better than a persistence or random forecast for all lead times and seasons but much less skillful than the stability decision. The decision with the lowest skill is the one relating to the presence of more than one layer of cloud given that cumulus cloud is present. The prediction of this rarely occurs in the model and observations and has a skill score no better than a random forecast. The remaining decisions relating to decoupled stratocumulus in stable and unstable conditions, are not significantly more skillful than persistence.

There is no significant impact of changing model resolution on the skill of predicting boundary-layer type. This is presumably due to the same parameterisations being applied to both resolutions studied here. The skill of the 1.5 km model maybe be improved as it does not contain a convection parameterisation. Finally, the most common daily boundary-layer type transitions have been compared. The top twenty sequences are similar in both the model and observations. The most common transition pattern is Stable → Well mixed → Well mixed → Well mixed → Stable. The observed transition patterns are much more diverse than that of the model. Also, cumulus cloud is more persistent in the observational transitions.

A possible reason for the low verification scores for decisions involving clouds maybe that it is difficult to predict gradients in smoothly varying fields (e.g. temperature and humidity) which are used to determine the presence of cloud. Also there are biases in the forecasts of temperature and relative humidity in the NAE 12 km, UK 4 km and UKV (1.5 km resolution model). The diurnal cycle of temperature is under predicted. In the winter there is a general warm bias but during the summer there is a warm bias at night and cold bias during the day. This pattern of biases can be seen in all forecast lead times (A. Lock, per. comm). The model also fails to capture the high values of relative

humidity at night.

The results presented here suggest that to improve the prediction of boundary-layer type then the focus should be placed on improving the forecast of boundary-layer cloud type. Cloud type should be focussed on as the skill of the model predicting cloud presence high compared to the decisions related to cloud type. A particular focus should be put on the diagnosis of cumulus cloud and the depth constraint that is currently applied. The 400 m constraint that is currently applied is potentially missing up to 69% of cumulus cloud which maybe partly causing the low SEDI score for the presence of cumulus cloud. Improving the representation of cumulus cloud should also have an impact on the skill of predicting more than one layer of cloud when cumulus cloud is present.

This evaluation could be extended to other models in the UK Met Office operational suite e.g. UKV (1.5 km resolution regional model) to further assess the impact of resolution on the forecast of boundary layer type. A further extension would be evaluate the skill at a different site. As Chilbolton is situated in a rural environment it would be interesting to compare the skill and climatology of boundary-layer type over an urban surface. An opportunity to do this may arise through the Advanced Climate Technology:Urban Atmospheric Laboratory (ACTUAL) project which has a Doppler lidar situated in central London.

The UK Met Office are the only model to use the Met Office boundary-layer scheme but many other models have a similar "tree" of decisions that is used to determine which parameterisation schemes are applied i.e. whether to apply a local or non-local mixing scheme. An example of this is the ECMWF model that uses an eddy-diffusivity mass-flux framework (Kohler et al., 2011). With this in mind it would be possible to extend this type of comparison to models from other forecast centres around the world. Although the verification scores for the processes that determine boundary-layer type forecast in the Met Office Unified Model are low a study by Barrett et al. (2009) found that the UK Met Office Models (global and NAE) had the highest skill of forecasting the presence of boundary layer cloud. Also, a two year, three site, study by (Hogan et al., 2009b) found that Met Office mesoscale model gave the best representation of the vertical distribution of cloud, with the ECMWF model coming second. Thus one may expect that the verification measures for other modelling centres to be lower than those presented here.

Chapter 4

Does boundary-layer type diagnosis affect the vertical distribution of pollutants?

In this chapter the potential impact that an incorrect boundary-layer type forecast can have on the vertical distribution of pollutants is investigated using the single column (SCM) configuration of the Met Office Unified Model. First the model and model set up are described, then simple cloud free experiments are used to show the impact of correctly predicting the diurnal cycle of sensible heat flux. These simple experiments give insight into the impact of correctly diagnosing a stable or unstable surface layer. The affect of the incorrectly diagnosing the presence and type of cloud on the vertical distribution of tracer are investigated. The influence of entrainment on the evolution of the boundary-layer is also explored.

4.1   Why investigate the vertical distribution of tracer?

The majority of pollutants in the troposphere originate in the atmospheric boundary layer, at or very near the surface, which is where their influence on air quality is most important. A capping inversion often separates the boundary layer from the free troposphere which inhibits the transport of air, and therefore pollutants, into the free troposphere. This can result in localised air pollution problems due to their accumulation over time. If pollutants are ventilated into the free troposphere they tend to have longer lifetimes than in the boundary layer, due to the lack of dry deposition and lower de-

composition rates at cooler temperatures. This, together with higher wind speeds in the free troposphere, can result in a localised air pollution source having regional-scale, or even global-scale impacts. Therefore incorrectly predicting boundary layer ventilation has both local and large scale impacts.

Observational and modelling studies have identified a number of processes that contribute to boundary-layer ventilation. Donnell et al. (2001), Agusti-Panareda et al. (2005), Dacre et al. (2007) and Sinclair et al. (2008) have classified these processes into three categories: convection, boundary-layer turbulent mixing and advection by synoptic scale motions. Here we focus on the impact of boundary-layer turbulent mixing, or more specifically the impact of the incorrect boundary-layer mixing parameterisation being applied.

Depending on the altitude of a pollutant in the atmosphere it can have very different effects. One such example of this is ozone. Within the boundary-layer it contributes to photochemical smog and is toxic to both animals and plants (World Health Organisation, 2006). In the upper troposphere it acts as a greenhouse gas and contributes to global warming (Hobbs, 2000). However, in the lower troposphere it can react with hydrocarbons and thus remove them from the air. It also acts indirectly controls the lifetime of other greenhouse gases. In the stratosphere the ozone layer filters out harmful ultra-violet (UV) rays (Ahrens et al., 2011).

As discussed in Chapter 3, the skill of the Met Office 4km and 12km models at predicting the correct boundary-layer type at exactly the right time in a particular model column is low. This misdiagnosis of boundary-layer type has an impact on the vertical mixing schemes that are applied and thus may have an impact on the vertical distribution of pollutants. The vertical distribution of pollutants, especially local surface concentrations, can have serious implications for human health. Impacts range from eye irritation, due to exposure to sulphur dioxide, to cardiovascular disease and lung cancer from chronic exposure to particulate matter (World Health Organisation, 2006). During blocking episodes pollutants such as nitrogen oxides and particulate matter can accumulate in the boundary layer and can cause photochemical smog and ozone production. During August 2003, it is estimated that 400-800 deaths were brought forward in the UK due to a elevated levels of ozone and volatile organic compounds during the heat wave (Stedman, 2003). It is also estimated that the same event brought forward in excess of 1000 deaths in the Netherlands (Fischer et al., 2003).

4.2   Model description

All experiments in this chapter are performed using the UK Met Office Single Column Model (SCM), version 7.8. An SCM represents a single atmospheric column at a grid point in a general circulation model (GCM). All physical processes in the UM SCM are treated identically to those found in the global UM, however the large-scale horizontal and vertical motions are taken from observations or prescribed by the user. This allows the column to be forced with time-varying atmospheric conditions. There are two main advantages of running an SCM rather than a GCM. When developing parameterisation schemes to represent physical processes it is useful to assess their impact on local climate without the complication of 3-D advection effects and it is much less computationally expensive as it takes much less time to run and uses less computer storage. Appendix A contains instructions on how to run version 7.8 of the Met Office Single Column Model locally at The University of Reading.

SCMs are tools used mainly by researchers and operational weather forecast centres to develop parameterisation schemes (e.g. boundary layer: Lock et al., 2000; cloud microphysics: Petch et al., 1997, Morrison et al., 2005; convection: Betts & Miller, 1986, Petch et al., 2007, Wood et al., 2010). They have also been used to study drizzling stratocumulus clouds (Wyant et al., 2007, Zhu et al., 2005), the diurnal transition of cumulus clouds (Lenderink et al., 2004) and ice clouds (Lohmann et al., 2001). SCMs have also been used extensively in the GEWEX Atmospheric Boundary Layer Study (GABLS) inter-comparison projects. The overarching aim of GABLS is to enhance understanding and to improve the representation of boundary-layer processes in weather forecast and climate models. As well as inter-comparing different boundary-layer schemes GABLS aims to improve SCMs by comparison to large-eddy simulations (LES) and observations (**?**).

An academic set-up of a stably stratified boundary layer was studied in GABLS1 (Beare et al., 2006; Cuxart et al., 2006). Here it was found, in general, that the operational SCMs had night-time mixing that is too deep compared to the LES models and too small near-surface wind direction. GABLS2 investigated the diurnal cycle over land (Svensson et al., 2011) using idealised forcings and prescribed surface temperatures. It was found in this comparison that the diurnal cycle of wind was too weak in SCMs and that the diurnal temperature amplitude was larger than observed. The best agreement between LES and SCMs was late afternoon when near-surface turbulence was at its strongest, however

there were still significant differences in the shape and magnitude of temperature and winds. It was also found that TKE schemes were the best at modelling the capping inversion but non-local first order schemes performed better at simulating the stably stratified part of the mixed layer.

GABLS3 considered the nocturnal low level jet and transitions (Baas et al., 2010). In this experiment observed large-scale forcings were applied and SCMs were coupled to the surface. All SCMs used in this comparison produced a low-level jet however, in general, the magnitude of the jet was under-predicted by up to $5 \, \mathrm{ms^{-1}}$. The same is true for night-time temperatures, with some models under-predicting 2 m temperature by up to 6 K. It was found that the models with a skin layer performed better due to better coupling to the surface (Bosveld et al., 2012; Holtslag et al., 2012). GABLS4 is expected to explore very stable conditions over an Antarctic ice shelf (Vihma et al., 2012).

The scenario considered in the GABLS2 project (Svensson et al., 2011), a cloud-free diurnal cycle, acts as a precursor for the modelling described in this chapter. However, the GABLS experiment did not have any cloud present thus the only boundary-layer types diagnosed were type I (stable) and type III (well mixed). The modelling presented in the following sections investigates the diagnosis types II, IV and VI as well as types I and III.

4.3   Experimental design

The diurnal cycle of boundary layer evolution can be investigated using the SCM by forcing it either with a time-varying surface temperature or forcing it with time-varying latent and sensible heat fluxes. In the *control* experiment the following form for a time-varying heat flux is used

$$H = \begin{cases} H_{night} & \text{for } t < 6 \text{ and } t > 18 \\ H_{night} + (100 - H_{night}) \sin\left(2\pi \frac{t-6}{12}\right) & \text{otherwise,} \end{cases} \tag{4.1}$$

where the units are $\mathrm{Wm^{-2}}$ and t is the time in hours and runs from 0 to 24 each day. Latent heat flux is forced in the same way with a night-time value of $-2 \, \mathrm{Wm^{-2}}$ and a day-time maximum value of $50 \, \mathrm{Wm^{-2}}$. These values are representative of an urban canyon (Stull, 1988). The small value of latent heat flux has been chosen to ensure fog does not form in the simulations. This idealised forcing is used to ensure that the impact of boundary-layer type can be separated easily from surface forcing effects. Here, a 15-

minute time step is used with surface latent and sensible heat flux prescribed every hour.

Other forcings can be applied to mimic large-scale atmospheric circulations. These can either be observational, and represented through tendencies of the wind velocity components, humidity and temperature. The geostrophic wind is held constant in time at each level throughout the simulation with a value of (1.75,1.75) ms^{-1} in the first model level, 10 m, increasing linearly to (14.5,14.5) ms^{-1} at the tropopause. The initial profiles of potential temperature and humidity (for both the cloud-free and cloudy cases) are shown in Figure 4.1. The initial potential temperature profile is taken from the midnight timestep of the GABLS2 simulation described in Svensson et al. (2011). This profile is used as it provides realistic representation of a stable boundary-layer. The experiment is initialised at 00 UTC. Note that there are 20 pressure levels in the first 3 km.
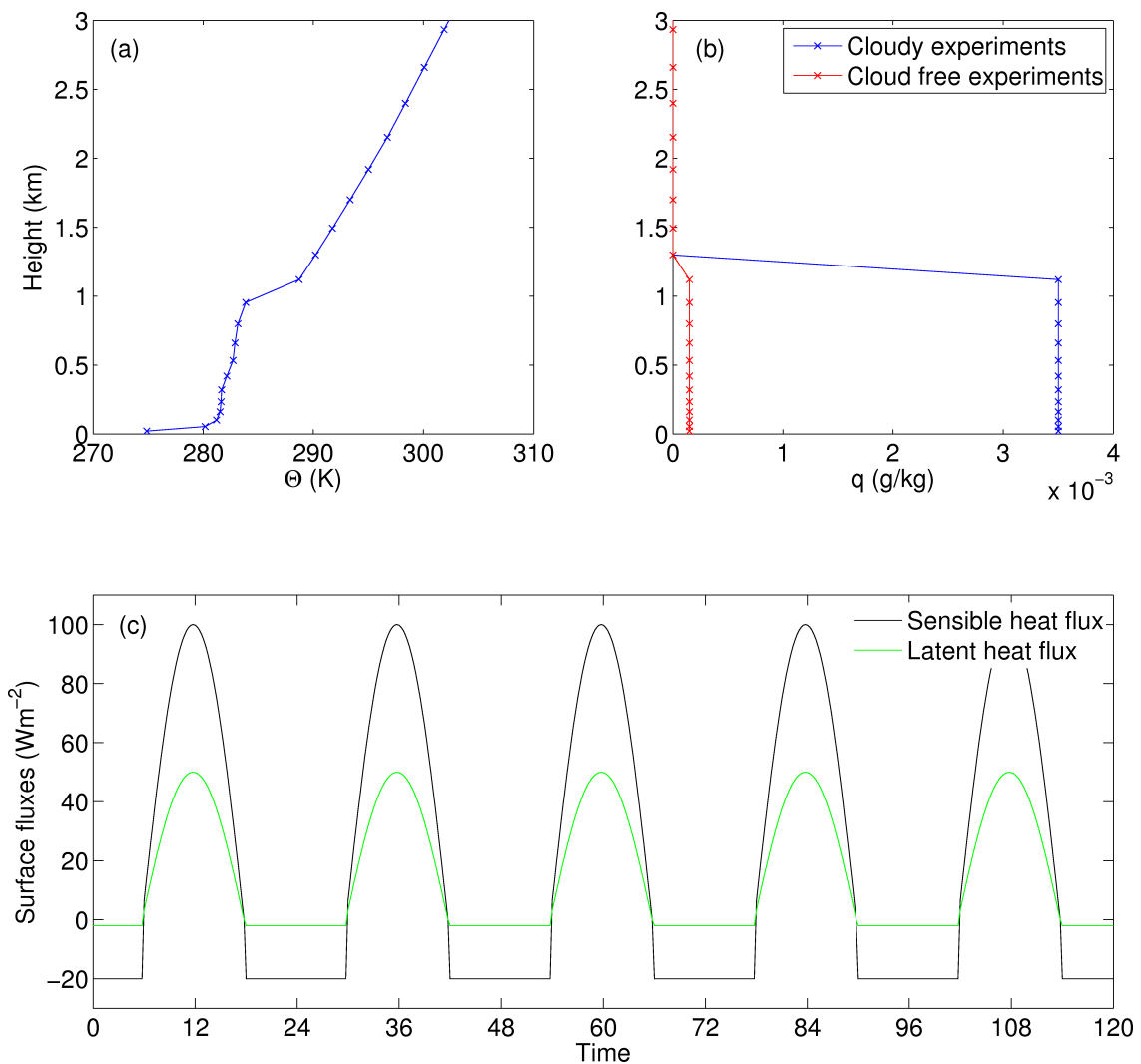
Figure 4.1: Initial profiles of (a) potential temperature and (b) specific humidity for all simulations in this chapter. Panel (c) shows the surface flux forcing applied throughout the simulations.

A passive tracer is released in the first theta model level (approximately 10 m) at a rate of 1×10^{-4} kg s^{-1} for the length of the simulation. The tracer is given an e-folding decay time. The decay time represents the chemical break down of a pollutant, either by decay or reaction with another chemical, with respect time. It also enables the integrated column mass to come to equilibrium. This means quantitative comparisons of tracer amounts can be made. The impact of the choice of decay time is investigated in each of the experiments detailed below. The tracer lifetimes used are 15 minutes (comparable to ozone reacting with NO), 1 hour (comparable to sulphur dioxide oxidation in clouds), 3 hours, 6 hours, 12 hours. Longer decay times of days and weeks have not been investigated here due to the long spin up time required. All experiments shown are run for 5 days. Figure 4.2 shows the integrated column mass as a function of time for each decay time. It can be seen that an equilibrium integrated column mass value is reached for all decay times by the start of day 3. For this reason only days 3–5 will be considered in the analysis below.
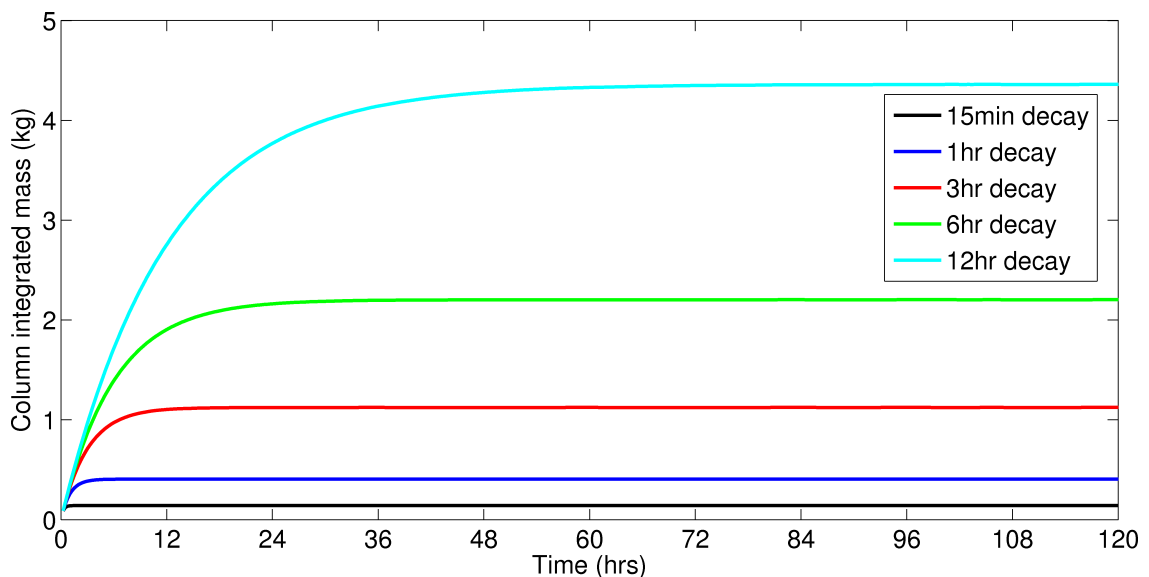
Figure 4.2: The evolution of integrated column mass as a function of time for decay times 15 minute, 1 hour, 3 hour, 6 hour and 12 hours.

4.4   Mixing in low shear environments

Preliminary experiments were conducted to investigate the sensitivity of the simulation of the boundary layer to different initial conditions and forcings. It was found whilst conducting these experiments that the local mixing scheme is sensitive to the amount of vertical wind shear, with experiments forced by low wind shear values having unrealisti-

cally large local diffusivity values. This can be seen by comparing Figures 4.3 (no vertical wind shear) and 4.4 (with vertical wind shear). The top panel in each figure shows the wind speed. Panel (b) shows the total diffusivity, K_h, in the simulation and panels (c), (d) and (e) show the constituent components of the total diffusivity profile seen in (b). For the no-shear case (shear = 0.0001 ms^{-1} km^{-1}) the diffusivity has very large values during the day, greater than 3000 kg ms^{-1}, and is dominated by the local mixing scheme $K_h(Ri)$. The converse can be seen in the experiment with wind shear (4 ms^{-1} km^{-1}), where the applied diffusivity values are much lower; the maximum value is approximately 600 kg ms^{-1} and is dominated by surface driven non-local mixing, K_h^{surf} (panel (d)) and non-local mixing due to cloud-top cooling, K_h^{Sc} (panel (e)). Note that the three components of diffusivity are combined in the following way (Lock & Edwards, 2011)

$$K_h = \max[(K_h^{surf} + K_h^{Sc}), K_h(Ri)]. \tag{4.2}$$

The philosophy behind this formulation is that local mixing will dominate in stable conditions and non-local mixing will dominate in unstable conditions. However, this assumption is erroneous as in certain conditions the non-local mixing does not dominate the mixing predicted by the local scheme. An example situation is the no-shear example shown in Figure 4.3.

This order of magnitude difference in the local mixing is due to the formulation of the stability function used in unstable situations (where the moist Richardson number, Ri, is less than zero). In the UM the diffusivity of heat is calculated in the following way

$$K_h = \mathcal{L}_h \mathcal{L}_m \left| \frac{\partial \mathbf{u}}{\partial z} \right| f_h(Ri) \tag{4.3}$$

where $\mathcal{L}_h$ and $\mathcal{L}_m$ are neutral mixing lengths, and the standard UM stability function, $f_h(Ri)$, for unstable conditions is

$$f_h = 1 - \frac{g_0 Ri}{1 + \mathcal{D}_h(\mathcal{L}_m/\mathcal{L}_h)|Ri|^{1/2}}. \tag{4.4}$$

In very low shear situations Ri becomes very large and negative. In this regime the stability function asymptotes to infinity giving values of K_h that are much larger than that calculated using the non-local mixing scheme and therefore dominate in Equation (4.2). This leads to unrealistically large boundary-layer mixing which could impact the vertical distribution of pollutants and surface temperature. Thus when designing the
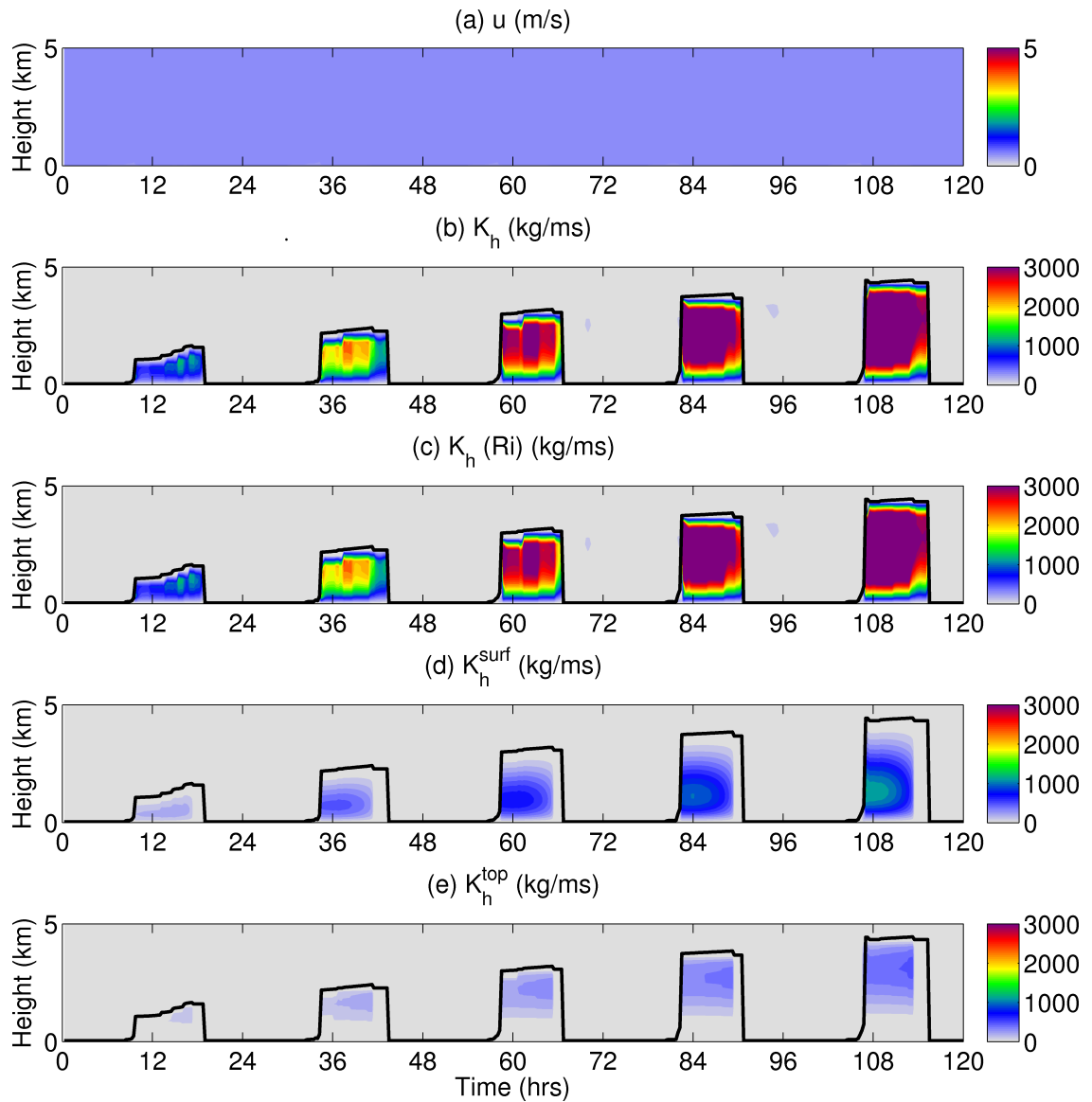
Figure 4.3: The evolution of the diffusivity variables for the no-wind-shear experiment: (a) wind speed, (b) total scalar eddy-diffusivity, (c) local scalar eddy-diffusivity, (d) surface-driven non-local scalar eddy-diffusivity, (e) top-down scalar eddy-diffusivity.

experiments presented in the remaining part of this chapter the inclusion of vertical wind shear was an important factor to consider, and has been adopted in all experiments.

It is also noted that in very unstable conditions, when all the turbulence is buoyancy driven, the mixing is independent of shear and therefore Richardson number. Thus Equation 4.4 is not valid. One possible solution to this problem is to treat the strongly-skewed local updrafts using a separate mass-flux scheme. This method is used in the ECMWF boundary-layer scheme (Kohler et al., 2011).

The growth of the boundary layer is controlled by two separate mechanisms, encroachment and entrainment. Encroachment is a purely thermodynamic process and results
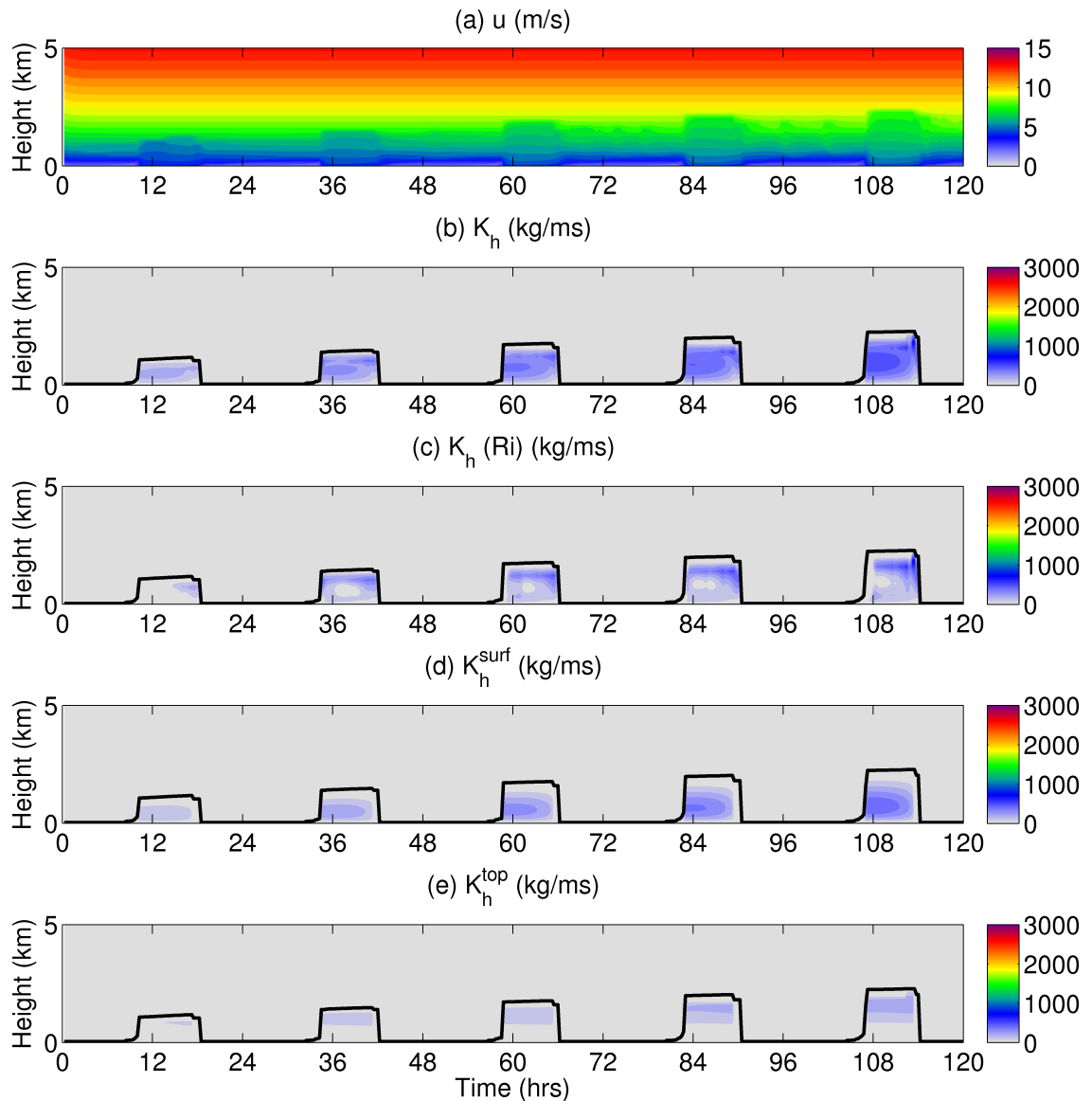
Figure 4.4: As Figure 4.3 but for the experiment with shear.

from the warming of the boundary layer from the surface below. Entrainment is the mechanism by which warm, dry air is carried from the free troposphere into the boundary layer by convective plumes that overshoot their level of neutral buoyancy. As this air sinks back into the mixed layer, it carries with it some of the warmer air from above. The volume of air entrained per unit area, per unit time is known as the entrainment velocity, w_e, and typically varies between 0.01 and 0.2 ms^{-1}. It is generally assumed in a cloud-free convective boundary layer (e.g. Carson, 1973) that the heat flux associated with the entrained air is a fixed fraction of the surface sensible heat flux. Estimates from observations suggest that this fraction is approximately 0.2 (e.g. Stull, 1976). However, this needs to be modified in the presence of cloud. The value used for entrainment is one

of the most uncertain parts of NWP and climate models. Sanderson et al. (2008) found that the entrainment coefficient had the largest impact on climate sensitivity in the climateprediction.net ensemble. Although this process is incredibly important for weather and climate predictions there are very few observations to compare parameterisations with (e.g. Nicholls & Turton, 1986; Wang & Albrecht, 1994).

There are many formulations in the literature for entrainment velocity, w_e. One such example is that of Rogers et al. (1985):

$$w_e \cong \left[\frac{g}{\theta} |\Delta_{EZ}\theta_e| l_c \right], \tag{4.5}$$

where $|\Delta_{EZ}\theta_e|$ is the difference in equivalent potential temperature between just above cloud top and just below, and l_c is the distance travelled by negatively buoyant entrained elements. When cloud-top cooling dominates this reduces to

$$w_e \cong \frac{\Delta I^*}{\Delta_{EZ}\theta_e}, \tag{4.6}$$

where ΔI^* is the net long wave radiative flux step near cloud top. Other entrainment relationships have been proposed based on the inverse of the convective Richardson number, Ri^*. The entrainment rate parameterisation used in the Met Office Unified Model is an extended version of Equation 4.5 based on LES experiments (Lock (1998)) and is described in full in Lock & Edwards (2011).

Entrainment is also considered to play a role in the development of boundary-layer clouds. It has long been suggested that entrainment of relatively warm and dry air into stratocumulus clouds may affect their break up and dissipation (e.g. Lilly, 1968; Deardorff, 1980; Randall, 1980; Stevens et al., 2005; Yamaguchi & Randall, 2008). As stratocumulus clouds strongly reflect incoming solar radiation but have little effect on outgoing longwave radiation they have a net cooling effect on the surface, and thus only small changes in the thickness and amount produce a radiative effect comparable to those associated with increases in greenhouse gases (e.g. Hartmann & Short, 1980). Lilly (1968), Burnet & Brenguier (2007) and Deardorff (1980) suggested that the evaporative cooling associated with the entrainment of the dry, warm air would lead to the break up of the stratocumulus sheet due to enhanced entrainment warming. Deardorff (1980) also suggested that there is a critical value of w_e that can be related to stratocumulus break up. Although this is a popular hypothesis there is yet to be any conclusive observational evidence to confirm it (e.g Wang & Albrecht, 1994 and Gerber et al., 2005). This lack of

evidence of cloud break-up has lead to a number of theories of competing mechanisms to be proposed. Moeng et al. (1995), Gerber et al. (2005) and Yamaguchi & Randall (2008) suggested that the evaporation caused by entrainment is balanced by cloud-top radiative cooling and efficient vertical transport of moisture evaporated from the surface, thus preventing cloud break-up. This mechanism could be particularly important over the ocean where there is a large moisture source. However, a study by MacVean & Mason (1990) developed a more stringent criterion for stratocumulus break-up that is more restrictive than the one proposed by Deardorff (1980) and Randall (1980). This criterion is based on the net conversion of potential energy and kinetic energy in a system consisting of two layers of fluid straddling cloud-top. MacVean & Mason (1990) also found that observational data is more consistent with their modified criterion. Also, Randall (1984) found that entrainment might deepen an existing cloud layer, not disperse it. He found that in many realistic situations the net effect of entrainment is that the cloud top tends to rise more quickly than the cloud base, thus the cloud depth increases with time.

4.5   Cloud-free experiments

In this section a set of cloud-free experiments have been performed to investigate the effect of having a positive sensible heat flux at night on the vertical tracer distribution. To ensure that the experiments remain cloud free the experiments are initialised with a uniform value of specific humidity, 0.00015 g kg^{-1}, from the surface to approximately 1km (Figure 4.1 (b)).

In Chapter 3, the skill of the Met Office 4km and 12km model at predicting the correct surface stability was assessed. It was found that although the skill of this decision was very high (SEDI score of 0.933) it was not perfect.

As an example of why the sign of the sensible heat flux may be wrong it has been observed that urban areas (see Figure 4.5) often have positive surface sensible heat fluxes at night (Grimmond & Oke, 2002). Typically this acts to increase the depth of the nocturnal boundary layer and therefore we would expect the pollutants to mix over a greater volume of air. Thus, for the same emissions, smaller surface concentrations of tracer may be observed in an urban area compared to a rural area (which is more likely to have negative sensible heat flux at night). A poor urban representation may result therefore result in the misdiagnosis of boundary-layer types I (stable with no turbulent cloud) and III (unstable, single well mixed layer) or type II (decoupled stratocumulus over a stable

layer) and type IV (decoupled stratocumulus) in cloudy conditions. Positive sensible
heat fluxes at night are also predicted in models which include an urban representation.
For example, Figure 4.6, shows the probability distribution function of night-time (1800
- 0600 UTC) sensible heat flux values from the Met Office 4km model for the grid points
closest to Chilbolton and King's College London (central London), indicating many more
instances of positive sensible heat flux at night at the urban grid point than the rural grid
point.
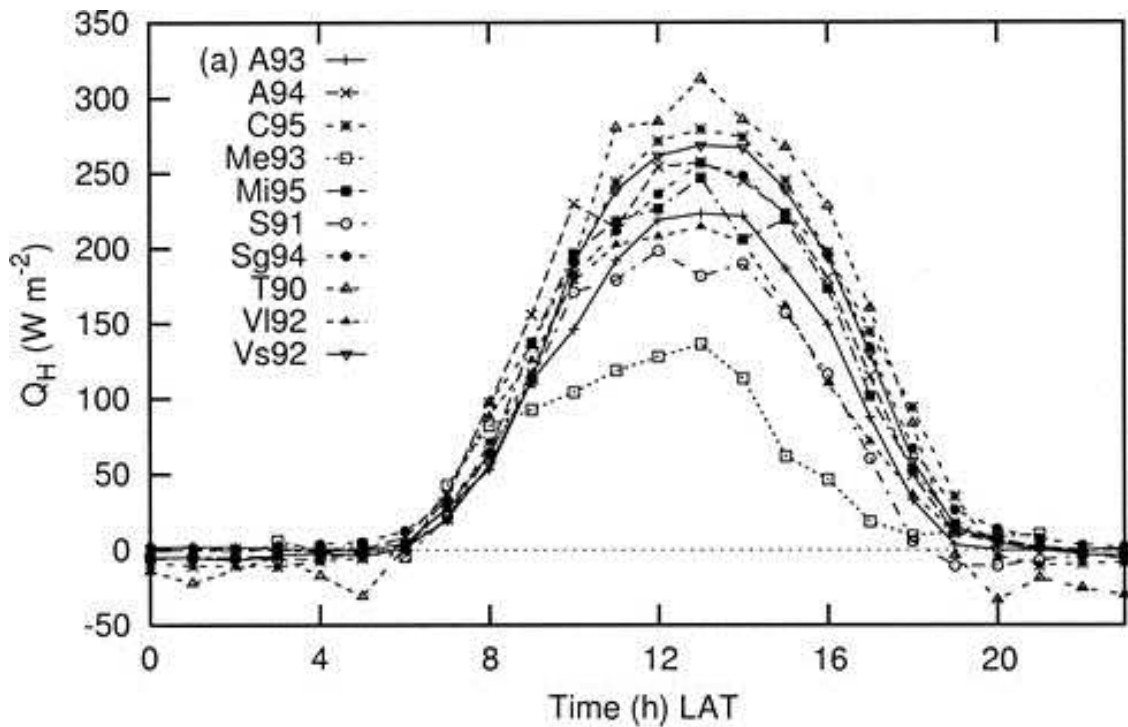
Figure 4.5: Composite diurnal patterns of sensible heat flux, Q_h, collected in seven North American cities (Mexico City, Mexico; Miami, Florida; Tucson, Arizona; Los Angeles and Sacramento, California; Vancouver, British Columbia; Chicago, Illinois), taken from Grimmond & Oke (2002).

Figure 4.7 shows the surface forcing applied for the experiments in this section. Three
different surface sensible heat flux forcings are used, all of which have the same day-time
values as Equation 4.1, with a peak value of 100 Wm^{-2}. During the night three different
values of sensible heat flux are applied, $H_{night} = -20, 0$ and 10 Wm^{-2}. The latent heat
flux forcing is unchanged in these runs.

Figure 4.8 shows the evolution of the boundary-layer top for the three forcings shown in
Figure 4.7. When H_{night} is increased from -20 Wm^{-2} to 0 Wm^{-2} the model diagnosed
boundary-layer top no longer collapses during the night and therefore the tracer does
not accumulate in the lowest model level as there is mixing over a greater depth. There
is little difference in boundary-layer top height between the experiments with H_{night} =
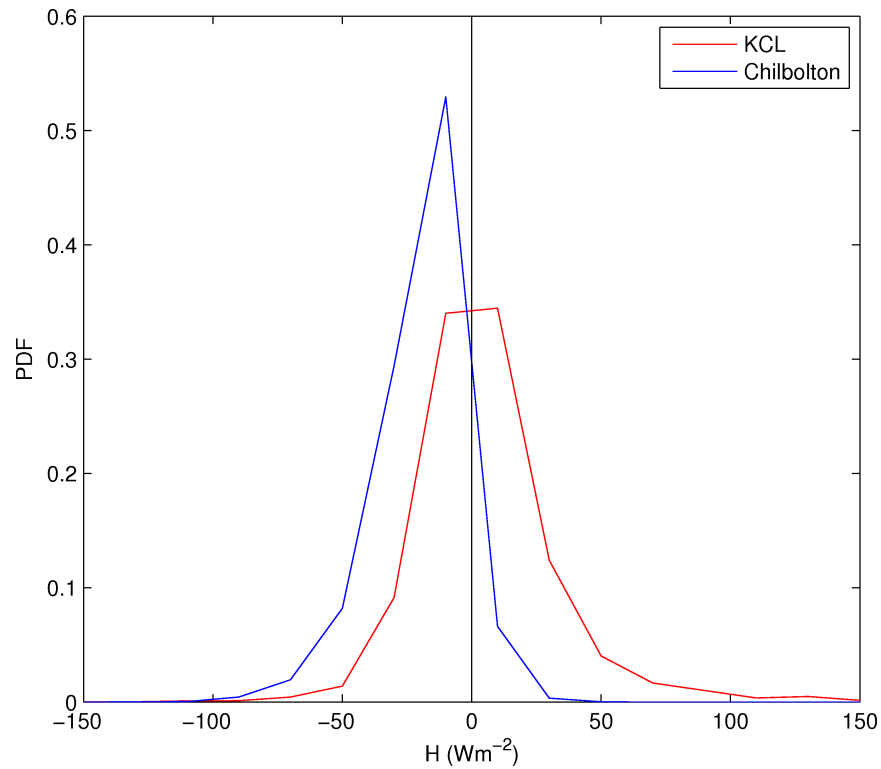
Figure 4.6: The probability distribution function (PDF) of night-time (1800–0600 UTC) sensible heat flux values from the Met Office 4 km model for the grid point closest to Chilbolton and the grid point closest to King's College London (based on hourly data from the period 01/03/2011 - 28/02/2012).
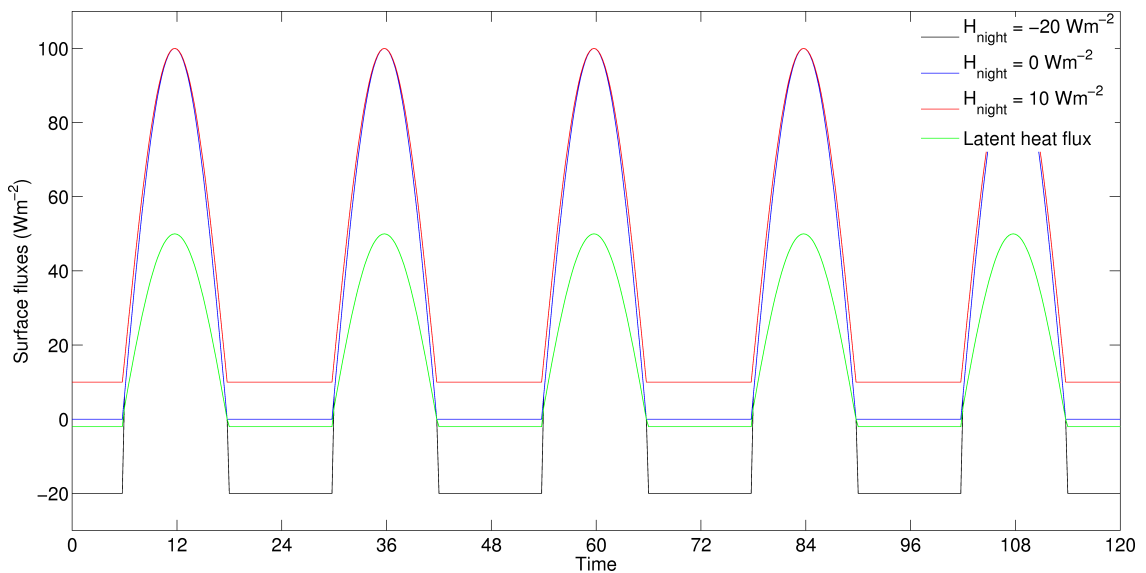
Figure 4.7: The surface flux forcing applied in experiments used to investigate the impact of varying the magnitude of the night-time sensible heat flux.

$0 \, \mathrm{Wm}^{-2}$ and $H_{night} = 10 \, \mathrm{Wm}^{-2}$. This is not unexpected as Carson's model of the growth

of the convective boundary layer (Carson, 1973) predicts the boundary-layer depth, h, in

the absence of anti-cyclonic subsidence to have the following form

$$h = \sqrt{\frac{2(1+2E)W}{\rho C_p \gamma}} \tag{4.7}$$

where W is the total sensible heat accumulated in the atmosphere during the day, E is the entrainment fraction, ρ is the density of the air, C_p is the specific heat capacity of the air and γ is the lapse rate (e.g. $\theta = \theta_o + \gamma z$). Therefore the boundary-layer depth is proportional to the square-root of the integral of the sensible heat flux, W and thus for a doubling of W the boundary-layer depth increases by a factor of $\sqrt{2}$.
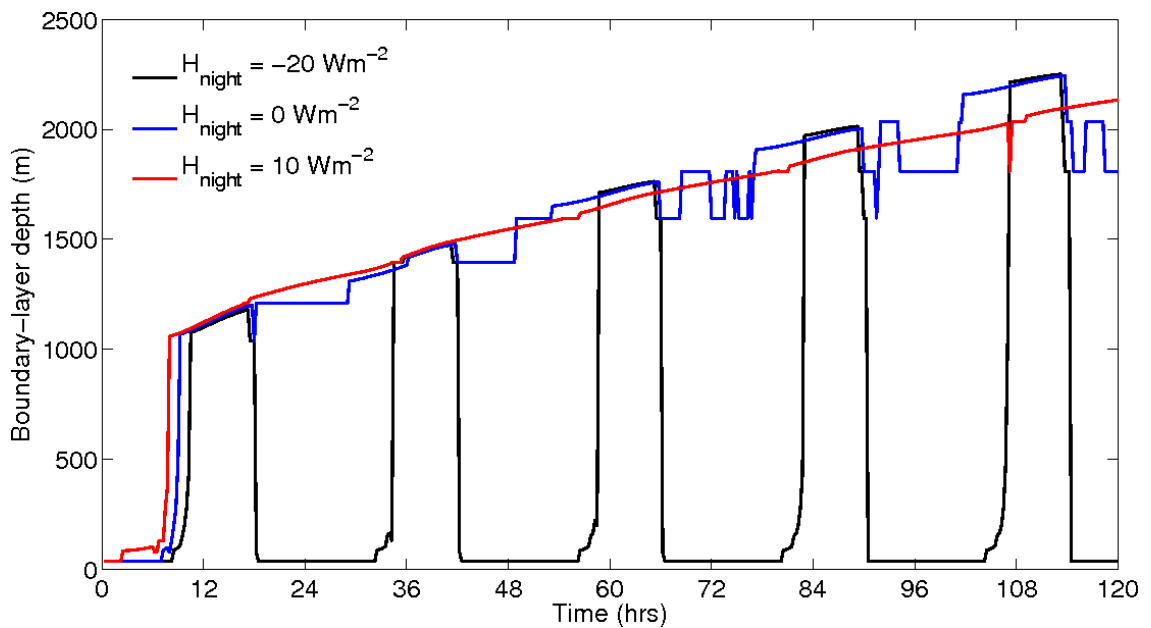
Figure 4.8: The evolution of boundary-layer top height for H_{night} = -20 Wm^{-2} (black line), H_{night} = 0 Wm^{-2} (blue line) and H_{night} = 10 Wm^{-2} (red line).

Focusing on the evolution of the tracer concentration in the lowest model level, Figure 4.9 shows that as H_{night} is increased the diurnal cycle collapses and there is no longer any night-time accumulation. The peak concentration values for the H_{night} = 0 Wm^{-2} experiments and the H_{night} = 10 Wm^{-2} experiments are up to an order of magnitude smaller than the H_{night} = -20 Wm^{-2} experiments for the longer decay times (3hr, 6hr, 12hr). Using 0200 UTC as a time that is representative of night, increasing decay time from 1hr to 12hr increases the level 1 concentrations by a factor of 2.5 - 5.5 depending on the H_{night} value. Changing the H_{night} forcing from -20 Wm^{-2} to 0 Wm^{-2} reduces the level 1 concentration by a factor of 10 for decay times longer than 3hr. Increasing H_{night} forcing further to 10 Wm^{-2} only reduces the concentrations by a further 30 - 40% depending on the decay time. Thus changing the sign of the night-time sensible heat

flux has a larger impact than increasing the decay time of the tracer. Changing H_{night} has little impact on day-time concentration values. For example the values are the same at hour 52 and hour 66 for all decay times.
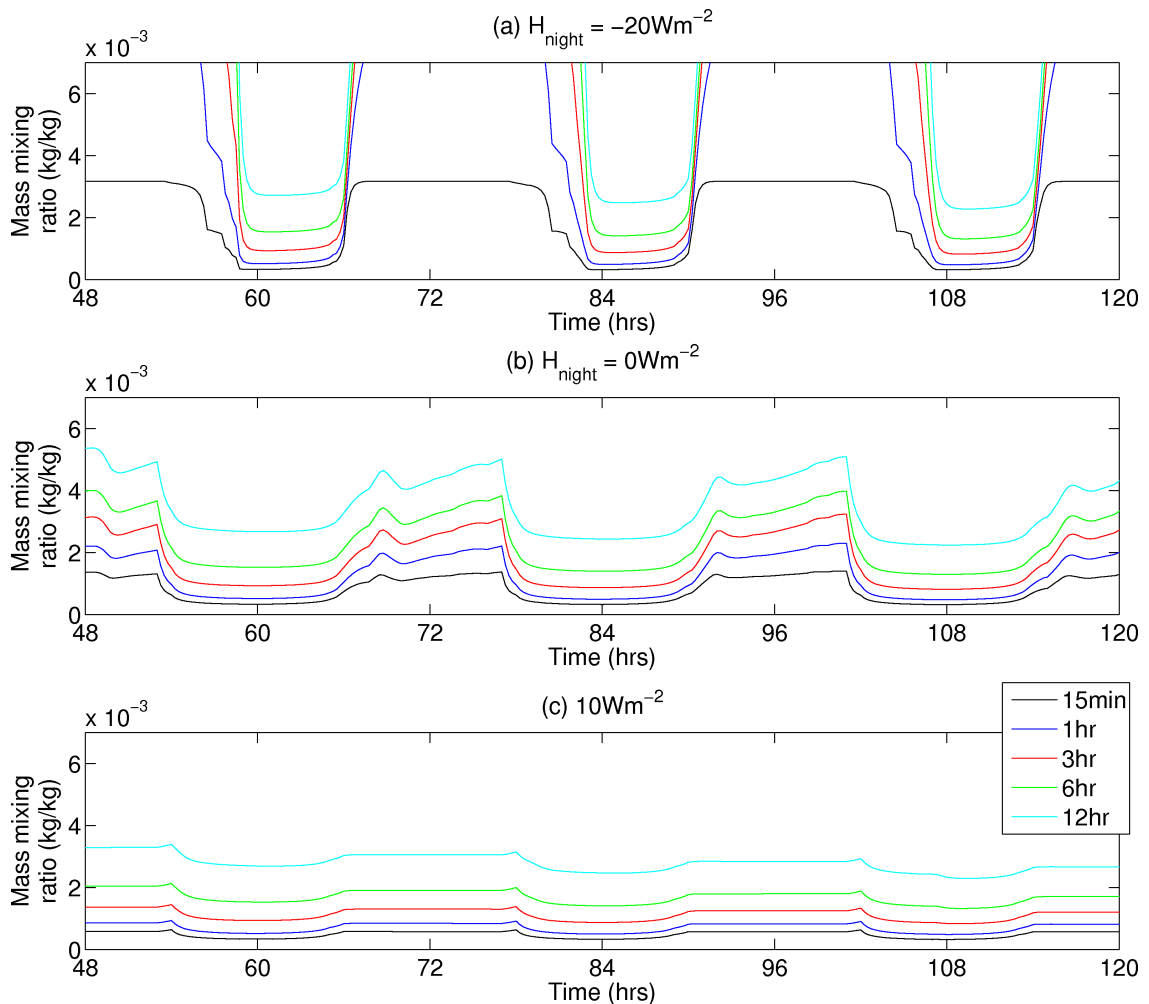
Figure 4.9: Diurnal evolution of tracer mass mixing ratio in model level 1 during days 3-5 for (a) $H_{night} = -20$ Wm^{-2}, (b) $H_{night} = 0$ Wm^{-2} and (c) $H_{night} = 10$ Wm^{-2}. Each panel shows each of the five different decay rates.

Finally, associated with the a reduction in night-time surface tracer mixing-ratios is a corresponding increase in tracer mixing ratios above. This is a result of the conservation of mass in the SCM. Figure 4.10 shows the vertical profiles of tracer concentration as a function of decay time and H_{night} at two representative times, 02 UTC (night) and 14 UTC (day), on day 3 of the simulations. As for the surface values, the full vertical profiles during the day are not sensitive to the value of H_{night} whereas the night-time mass is redistributed throughout the depth of the residual layer as H_{night} is increased. The non-zero mass mixing ratio seen above the surface in the $H_{night} = -20$ Wm^{-2} case is due to mixing from the previous day that has not yet decayed.
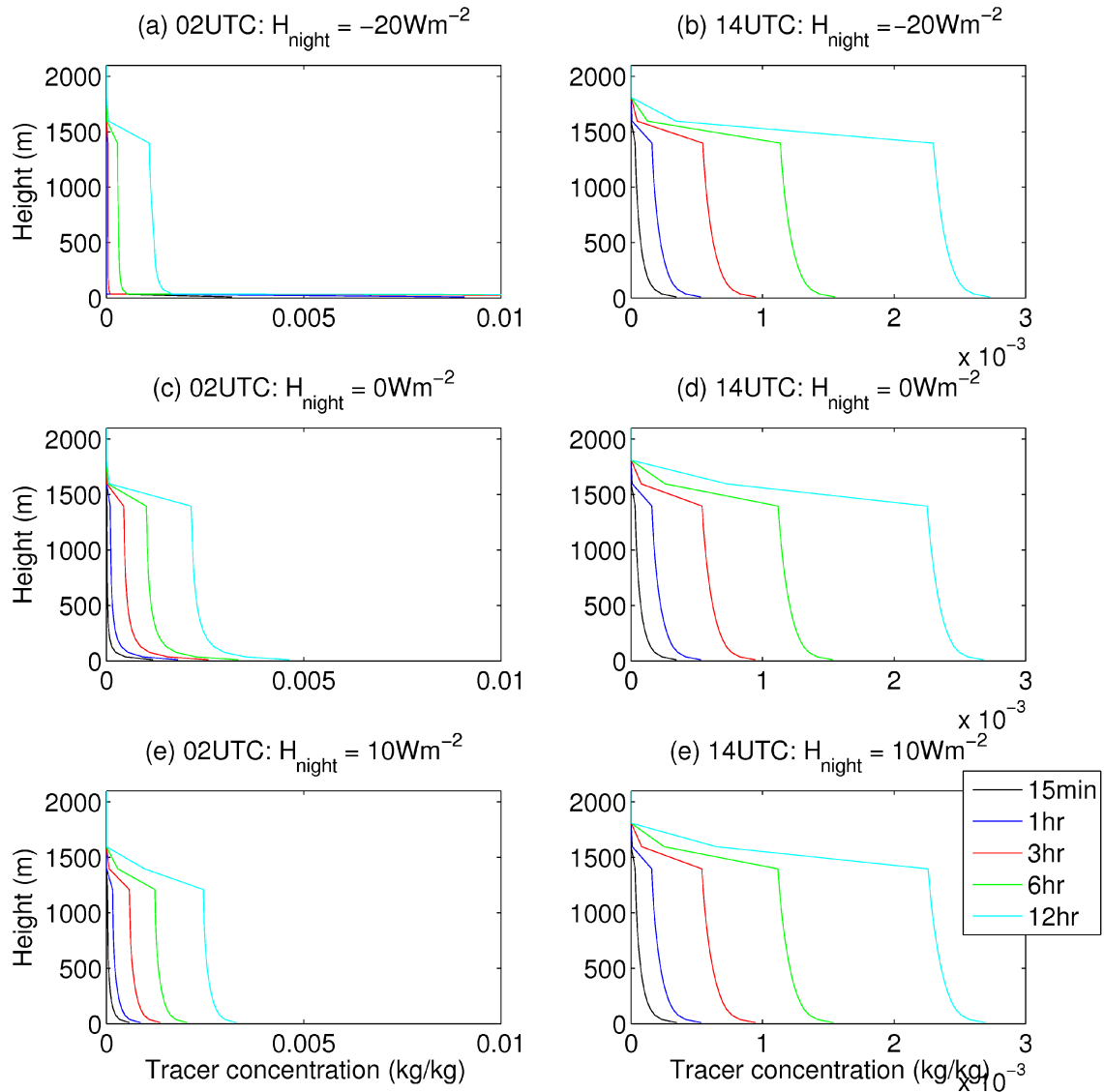
Figure 4.10: Vertical profiles of tracer mass mixing ratio for day 3 02 UTC and 14 UTC for H_{night} = −20, 0 and 10 Wm^{-2}.

In summary, the hypothesis that, for the same tracer emission and weather conditions, urban areas have a lower value of surface tracer concentrations is confirmed here using an idealised single column model. Changing the sign of the night-time surface sensible heat flux has a large impact on the surface concentrations, reducing them by at least a factor of 10. This is twice the impact of increasing the tracer decay time from 1hr to 12hr.

4.6 Effect of cloud type on vertical mixing

In this section, three sets of idealised experiments with cloud are run to test the impact of mixing associated with moist convection and cloud top radiative cooling, and thus

cloud type, on the vertical distribution of tracer. The surface forcing applied is the same as for the $H_{night} = -20 \, \text{Wm}^{-2}$ experiment in Section 4.5. Initial conditions used in this section are also the same as the experiments presented in Section 4.5 but with an initial moisture profile of 0.0035 g kg^{-1}, from the surface to approximately 1km (see Figure 4.1 (b)). Note that idealised simulations of all 9 boundary layer types in Figure 2.1 were not performed due as the model is highly sensitive to initial conditions and these types were not possible to model in this setup.

The experiments performed are summarised in Table 4.1.

1. The first experiment is a *control* experiment where there are no modifications to the boundary-layer scheme.

2. The second experiment is initialised and forced in the same way as the *control* experiment but with the SCM code modified such that cumulus cloud cannot be diagnosed, thus cumulus-capped boundary-layer types (V and VI) cannot be diagnosed. Type VI will be diagnosed as type III (well mixed) and type V as type IV (decoupled stratocumulus). This experiment was conducted to identify the impact of misdiagnosing cumulus-capped boundary layers.

3. The final experiment is also forced and initialised in the same way as the *control* experiment but all top-down mixing has been switched off and therefore is equivalent to not diagnosing stratocumulus cloud. This experiment highlights the differences between type I (stable, no turbulent cloud) and type II (decoupled stratocumulus over a stable surface layer) in stable conditions and type III (well mixed) and type IV (decoupled stratocumulus) in unstable conditions.

4.6.1 Control simulation

Figure 4.11 shows the evolution of specific humidity, potential temperature, cloud fraction, diffusivity of heat, tracer distribution, boundary-layer depth and diagnosed

Table 4.1: Summary of cloudy experiments performed

Shorthand name	Mixing by cumulus clouds	Mixing by cloud-top radiative cooling	Boundary-layer types tested
control	✔	✔	-
no-cumulus	✘	✔	No types V or VI
no-top-down	✔	✘	No types II or IV

boundary-layer type for days 2–5 of the *control* simulation. As time evolves the specific humidity decreases (panel (a)) and the potential temperature increases slightly (panel (b)). The inversion capping the boundary layer rises due to the input of sensible heat from the surface forcings. Each day a boundary layer grows to a depth of approximately 2 km, as indicated by the white line. This is not always at the same height as the potential temperature inversion as the model definition of boundary-layer top in cumulus capped conditions is the height of the lifting condensation level (LCL). The cloud-top heights are instead limited by the temperature inversion, which is generally above the LCL.

Throughout the run there is cloud present (panel (c)). This takes the form of a layer of stratocumulus cloud at night which breaks up during the day to give a cumulus capped boundary layer. This transition from stratocumulus to cumulus cloud is reflected in the day-time boundary-layer type transition from type IV to type VI (panel (f)). The decoupled stratocumulus boundary-layer type is diagnosed consistently during the morning transition. This persistent diagnosis of type IV during the morning transition could be the reason for the peak in the frequency of type IV seen in Figure 3.4 panels (f) and (g). As described in Section 4.4, the boundary-layer mixing is represented by a diffusion coefficient, K_h (shown in panel (d)). For the *control* simulation, the diffusivity is dominated by non-local surface-driven mixing during the day and non-local top-down mixing associated with cloud top radiative cooling during the night. Note that the model considers stratocumulus cloud to be present only when cloud fraction is greater than 0.1 (Lock & Edwards, 2011).

Panel (e) shows the evolution of continuously-released passive tracer as in the previous section, with a decay time of 6 hours. As for the cloud free experiments there is an accumulation of tracer in the lowest model level during the night whilst the tracer in the residual layer above decays. The accumulated tracer is then mixed throughout the depth of the boundary layer during the day-time. As there are convective clouds present in this simulation, tracer is lofted above the model diagnosed boundary-layer top during days 3, 4 and 5 to give a bimodal vertical distribution of tracer. This vertical transport of tracer is done by the convection scheme. It essentially displaces some tracer from the model level below the boundary-layer top and redistributes it, in this case, in the two model levels above the boundary-layer top. As this mixing is performed by the convection scheme, and not the boundary-layer scheme, there is no associated mixing shown in the K_h plot in panel (d), which represents the mixing done by the boundary-layer scheme only. It is interesting to note that no tracer is vented above the potential temperature

inversion into the free troposphere in this simulation.
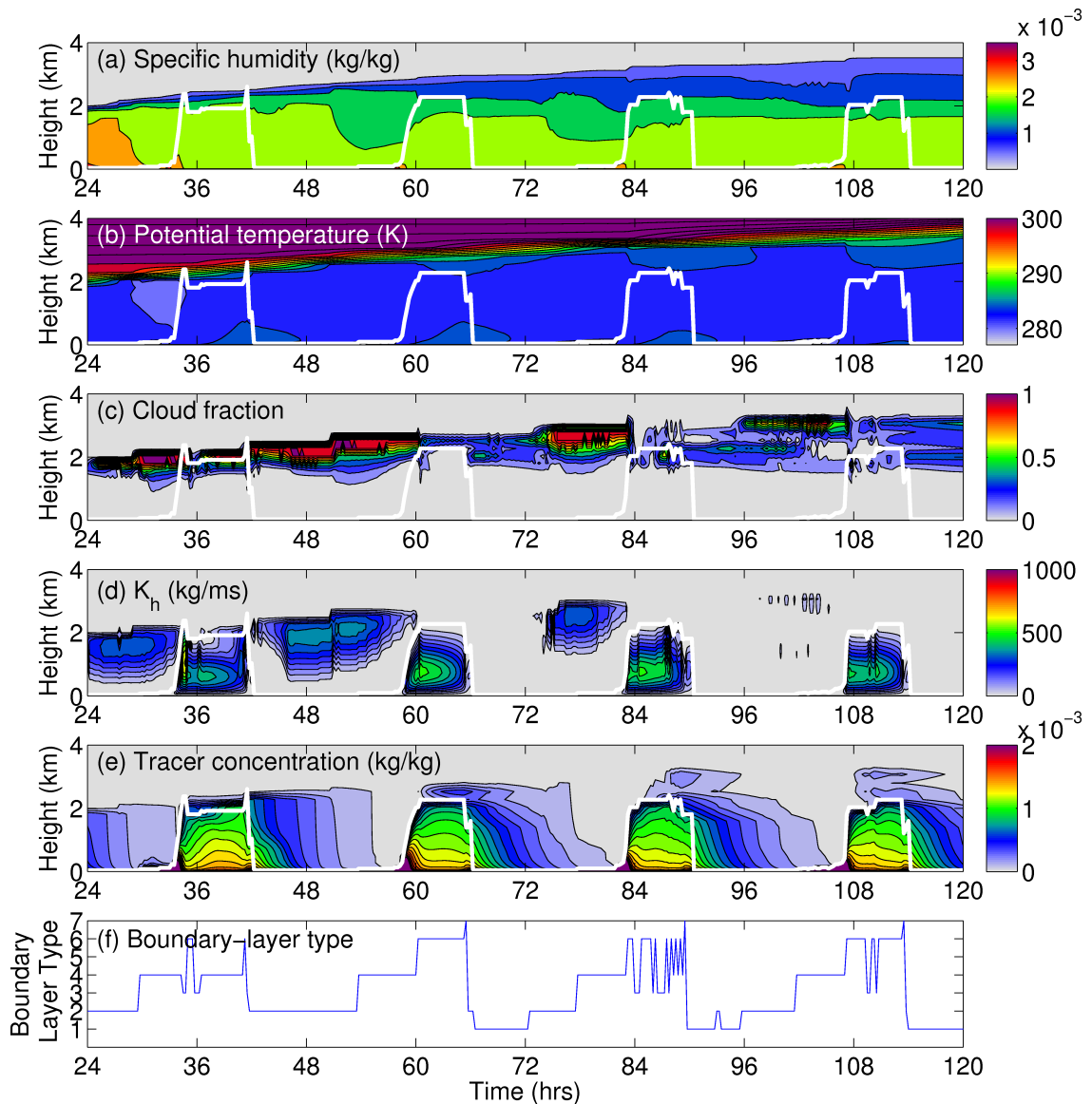
Figure 4.11: The evolution for days 2–5 of the cloudy *control* run. (a) specific humidity, (b) potential temperature, (c) cloud fraction, (d) diffusivity, (e) tracer distribution (decay rate *6hr*) and (f) boundary-layer type. In all panels the white line indicates the model-diagnosed boundary-layer top.

The effect of decay time on the vertical distribution of tracer has also been investigated in this cloudy situation. Figure 4.12 shows the distribution of tracer for five decay times ranging from 15 minutes to 12 hours. As expected from Section 4.5, the largest mass mixing ratios accumulated in the surface layer and vented above the boundary-layer top are by the tracer with the longest decay time, 12 hours. For significant amounts of tracer mixed up into the residual layer to persist to the next day a decay time of 12 hours is needed (panel (e)).

The venting-above the model diagnosed boundary layer occurs for all decay times (this
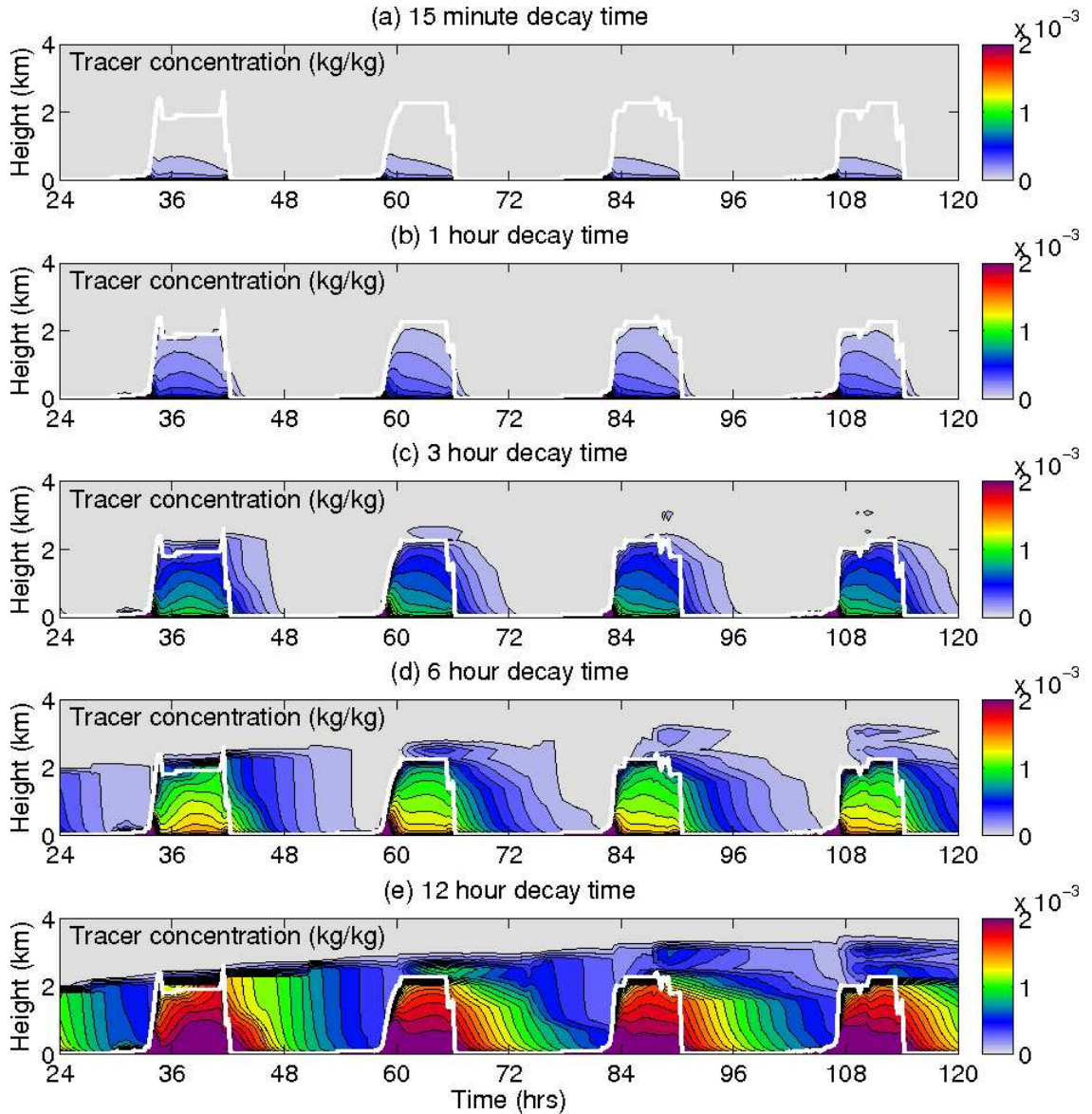
Figure 4.12: The tracer distribution evolution for days 2–5 of the 5 day cloudy run for decay time (a) 15 minutes, (b) 1 hour, (c) 3 hours, (d) 6 hours and (e) 12 hours.

is not visible in panels (a) and (b) due to the contour intervals used). Figure 4.13 shows the tracer concentration for all decay times at the height of the first model level above the diagnosed boundary-layer height for hour 60 of the *control* simulation. This hour was chosen as it is the first hour that transitions to type VI after the integrated column mass has reached equilibrium for all decay times. It shows that venting does occur for all decay times and it occurs in the timestep after the boundary layer has been diagnosed as cumulus capped. The typical mixing time due to convection, T, can be approximated by $T \approx \frac{h}{w_*}$ (Stull, 1988) where h is the depth of the boundary layer and w_* is the convective velocity scale, representing the strength of the updrafts of the largest eddies, which can be estimated, on dimensional grounds, as $w_* = \left(\frac{g}{\theta} \frac{H}{\rho C_p} h \right)^{\frac{1}{3}}$ (Stull, 1988). In this simula-

tion at time 60.25 hours, w_* is approximately 1.9 ms^{-1}, which gives a convective time scale of approximately 17 minutes, which is comparable to the timestep of 15 minutes used here, and is therefore in agreement with the appearance of the bimodal vertical structure after a single timestep.
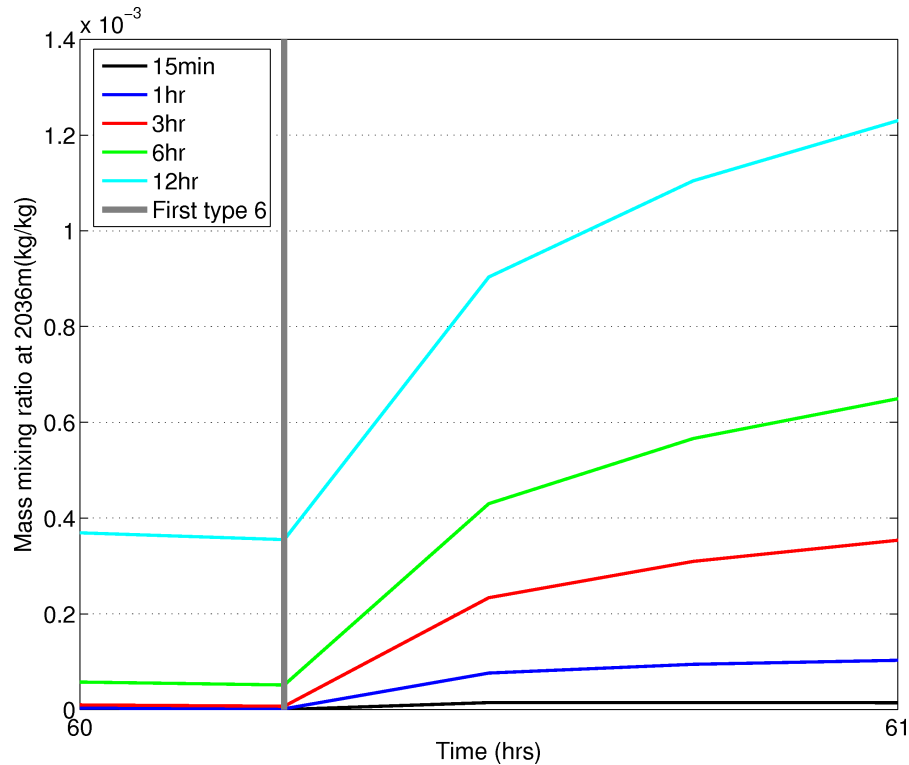
Figure 4.13: The evolution of tracer concentration at 2036m (model level above boundary-layer top) for hour 60 of the *no-cumulus* run for decay times 15 minutes (black line), 1 hour (blue line), 3 hours (red line), 6 hours (green line) and (e) 12 hours (cyan line). The thick grey line indicates the time at which the boundary layer is first diagnosed as cumulus capped (type VI).

4.6.2   No-cumulus experiment

In this section the impact that cumulus convection has on the vertical distribution of tracer is investigated. This is achieved by modifying a condition in convection scheme in the SCM so that cumulus cloud cannot be diagnosed. The result is that cumulus-capped boundary layers (type VI) diagnosed in the *control* simulation of Section 4.6.1 are diagnosed instead as being well mixed in this experiment. This effectively switches off all cumulus-linked convection and therefore should highlight the differences expected if a cumulus-capped boundary layer (type V or VI) was misdiagnosed as a well-mixed boundary layer (type III) or decoupled stratocumulus (type IV). All forcings and initial conditions applied are as outlined in 4.6.1.

Figure 4.14 shows the evolution of specific humidity, potential temperature, cloud fraction, diffusivity of heat, tracer distribution, boundary-layer depth and diagnosed boundary-layer type for days 2–5 of the *no-cumulus* experiment. As in the *control* run with cumulus cloud there is a strong temperature inversion that caps the boundary layer (panel (b)) and limits the vertical extent of the boundary-layer cloud. The cloud present in this run is a thick layer of stratocumulus that increases in cloud fraction throughout the simulation (panel (c)). This increased cloud fraction is not seen in the *control* run as the stratocumulus cloud breaks up to give cumulus cloud during the day, thus the stratocumulus cloud layer has to build-up again each night. Associated with this thicker stratocumulus cloud there is enhanced top-down vertical mixing during each night (panel (d)). The day-time mixing is also enhanced.

The boundary-layer type diagnosed is shown in panel (f). As expected, there are no occurrences of the cumulus-capped boundary-layer type (type VI). The model-diagnosed boundary-layer top in this experiment is higher than that diagnosed in the *control* run, by as much as 40%, as the definition of boundary-layer top is different depending on the boundary-layer type diagnosed. If a well-mixed (type III) or a decoupled stratocumulus (type 4) boundary-layer type is diagnosed then the boundary-layer top is calculated using a parcel ascent method. However, if a cumulus-capped (type VI) boundary layer is diagnosed then the boundary-layer top is taken as the LCL.

The evolution of tracer concentration with 6 hour decay shown in Figure 4.14 (e) lacks the bimodal structure present in the *control* run, consistent with the fact that all mixing is performed by the boundary-layer scheme and not a combination of the boundary layer and convection scheme. However, as the boundary-layer top is higher in this simulation there is still tracer present at the same height that the tracer is elevated to in the *control* experiment. As the simulation progresses a shoulder appears in the night-time distribution of tracer. This is most pronounced during the night of day 4 and is due to the enhanced top-down mixing compared to the *control* run.

Figure 4.15 shows tracer concentration as a function of time for both the *control* run (solid lines) and the *no-cumulus* simulation for all decay times at specified model levels. Panel (a) shows near surface (10 m) concentrations. As expected, the largest surface concentrations are seen for the largest decay time (12 hours). During the day the concentrations for the non-cumulus experiment are lower than the *control* experiment by 10% due to the tracer being mixed over a larger depth as the boundary-layer top is higher. At night the boundary-layer top collapses to the lowest model level and the concentrations in both
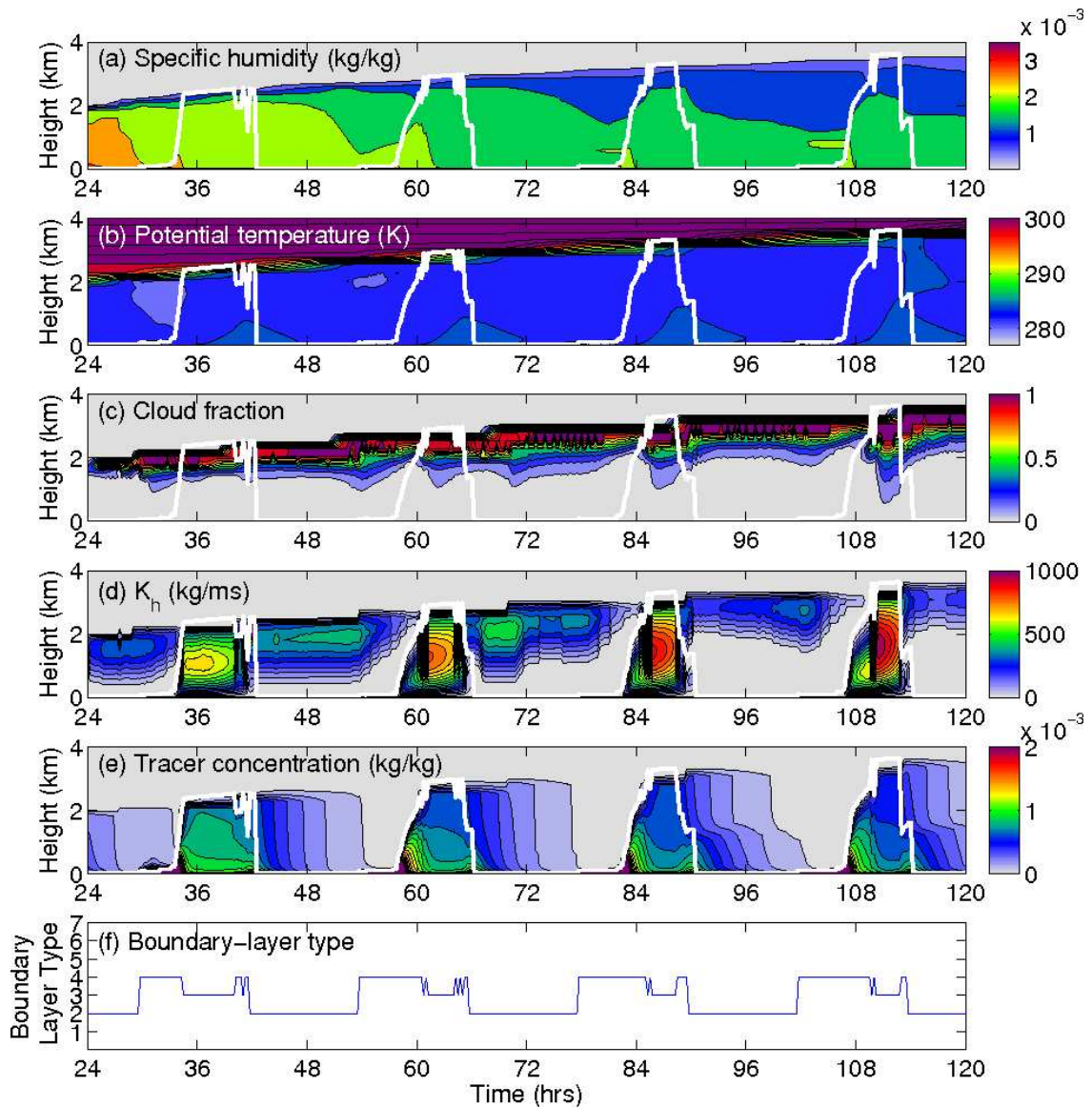
Figure 4.14: As Figure 4.11 but for the *no-cumulus* experiment.

runs are the same until the boundary layer starts to grow in the morning transition. Once tracer has reached 730 m (panel(b)) day-time concentrations stay relatively constant. At night the tracer amount decays exponentially. The same behaviour can been seen at 1597 m (panel (c)). The evolution of the tracer concentration at 2797 m are more complicated as it takes time for the boundary layer to grow to this height. There is much more tracer at this level in the convection-turned off experiment than the *control* experiment, suggesting that boundary-layer mixing is more efficient than convection. This is true for all decay times. During days 3 and 4 the peak in tracer concentration in the *control* run lags the peak in the convection-off run by up to 6 hours.

The impact of convection on the vertical profile of tracer concentration can be seen in
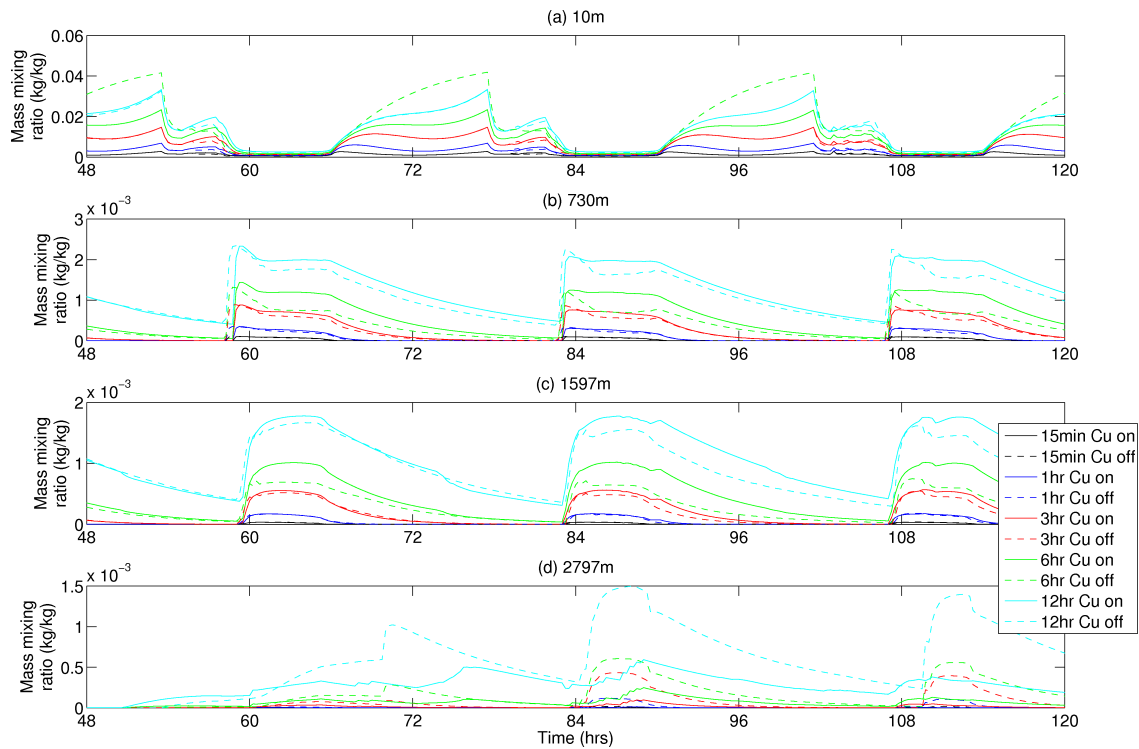
Figure 4.15: The evolution of tracer concentration for days 2–5 of the *control* run (solid lines) and *no-cumulus* run (dashed lines) at (a) 10 m, (b) 730 m, (c) 1597 m and (d) 2797 m. The colours indicate the different decay timescales.

Figure 4.16. During the afternoon, once the boundary layer has reached its maximum depth, the vertical profiles in the *no-cumulus* case becomes well mixed due to K_h^{surf} being twice as large than in the *control* run. The *no-cumulus* case has lower concentrations at 1500 m due to the boundary-layer top being higher than in the *control* experiment. The tracer with the longest decay time has the highest concentrations throughout the depth of the boundary layer in all cases. The convective case has lower concentrations at boundary-layer top than the non-convective case. Panels (b)–(e) highlight the non-smooth nature of convective venting out of the boundary-layer. Again, the largest effects can been seen for the longest decay times. For decay times 3 hours and greater the effect of convection on the vertical profile can been seen well after convection has stopped (panel (f)). For a tracer with a decay time of 12 hours this effect persists throughout the day and can be seen for up to 8 hours in to the night.

In summary, the effect of misdiagnosing a cumulus-capped boundary layer as a well mixed boundary layer causes a slight decrease in near-surface tracer concentrations due to the tracer being mixed over a larger depth as the model diagnosed boundary-layer top is deeper in the *no-cumulus* case. The vertical profiles of tracer are more well-mixed in the no-convection case and have larger tracer mass mixing ratios above 2 km. Al-
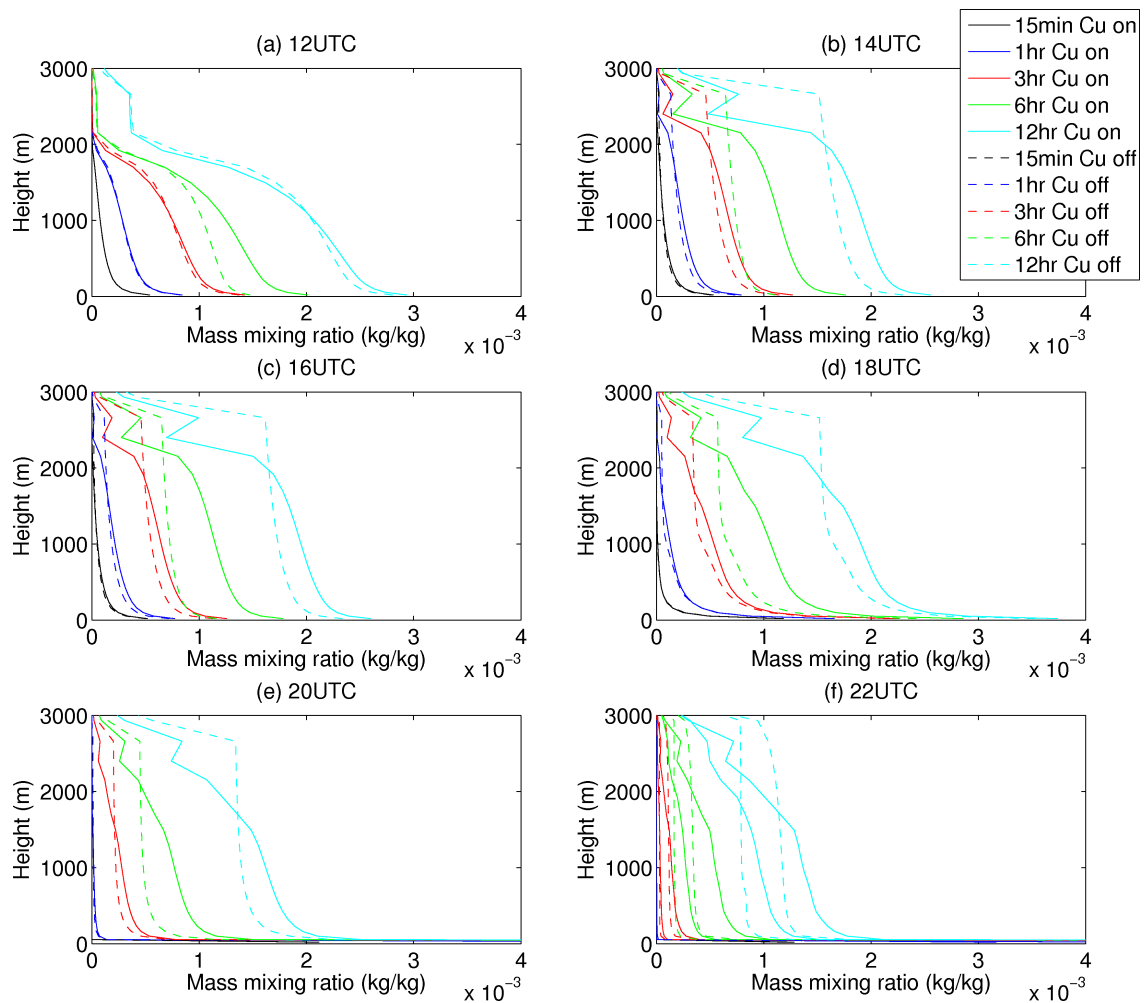
Figure 4.16: The vertical profile of tracer concentration at (a) 12 UTC, (b) 14 UTC, (c) 16 UTC, (d) 18 UTC, (e) 20 UTC, and (f) 22 UTC on day three of the *control* run (solid lines) and *no-cumulus* (dashed lines) for all decay times. The colours indicate the different decay timescales.

though the tracer considered here is passive, the difference in vertical profile could have implications for chemistry within the boundary layer.

This is a counter intuitive result as in the *no-cumulus* case a source of mixing has been removed (i.e. convection) but the total mixing has increased. This is because the mixing associated with the cumulus slightly stabilises the potential temperature profile so that the cumulus cloud layer is stable to dry ascent but unstable to moist ascent. This prevents the boundary-layer scheme mixing into the cumulus layer. When the cumulus cloud is not permitted, as is in the *no-cumulus* experiment, the top part of the boundary layer is now as unstable as the rest of the boundary layer and boundary layer mixing acts strongly throughout the entire depth. It is important to note here that this is a model result and therefore depends on the model simulating the action of cumulus cloud correctly.

4.6.3 Top-down mixing turned off

Next, the impact that top-down mixing has on the vertical distribution of tracer is investigated. This is achieved by setting the K_h^{Sc} term in the non-local mixing scheme to zero (Equation 4.2). This is intended to highlight the differences expected if a type II (decoupled stratocumulus over a stable layer) were misdiagnosed as a type I, as well as highlighting and the impact top-down mixing has in type III and type IV situations. Another motivation for this experiment is that not all models include a top-down mixing in their boundary-layer parameterisation scheme (e.g. Meteo-France which use a vertical mixing scheme based on a prognostic turbulence scheme derived from the Cuxart-Bougeault-Redelsperger proposal (Cuxart et al., 2000)). All forcings and initial conditions applied are as outlined in 4.6.1. As it is the effect of top-down mixing that is is being investigated here, significant differences in the surface concentrations are not expected; however, it is expected that the top-down mixing will modify the vertical profile of tracer. It is also expected that differences seen will be larger at night in this comparison as this is the time that the top-down mixing from the stratocumulus dominates in the *control* experiment.

Figure 4.17 shows the evolution of specific humidity, potential temperature, cloud fraction, diffusivity of heat, tracer distribution, boundary-layer depth and diagnosed boundary-layer type for days 2–5 of the *no-top-down* experiment. As in the previous experiments presented there is a temperature inversion (panel (b)); however, in this case at night it is not as strong as in the *control* or *no-cumulus* simulations. Cloud (panel (c)) is present through out the simulation but the cloud fractions are much less than those in previous experiments with the largest differences being during the night. Panel (d) shows the K_h evolution, and as designed there is only a small amount of elevated mixing, but this is from the local scheme. The tracer evolution is similar to that that in the *control* experiment. The boundary-layer type evolution is also similar to that in the *control* experiment (panel (f)). The type seems more transient on days 3 and 5 than the *control* experiment. It is this vacillation between cumulus-capped and well-mixed diagnosis that is responsible for the "bumpy" nature of the boundary-layer top on those days due to the change in boundary-layer top definition.

As predicted there is little difference in the near-surface concentrations of tracer between this experiment and the *control* during the night (1800–0600 UTC) and during the afternoon (1200–1800 UTC) (Figure 4.18 (a)). This is true for all tracer decay times. However, there are some large differences during the morning transition period, up to a factor of
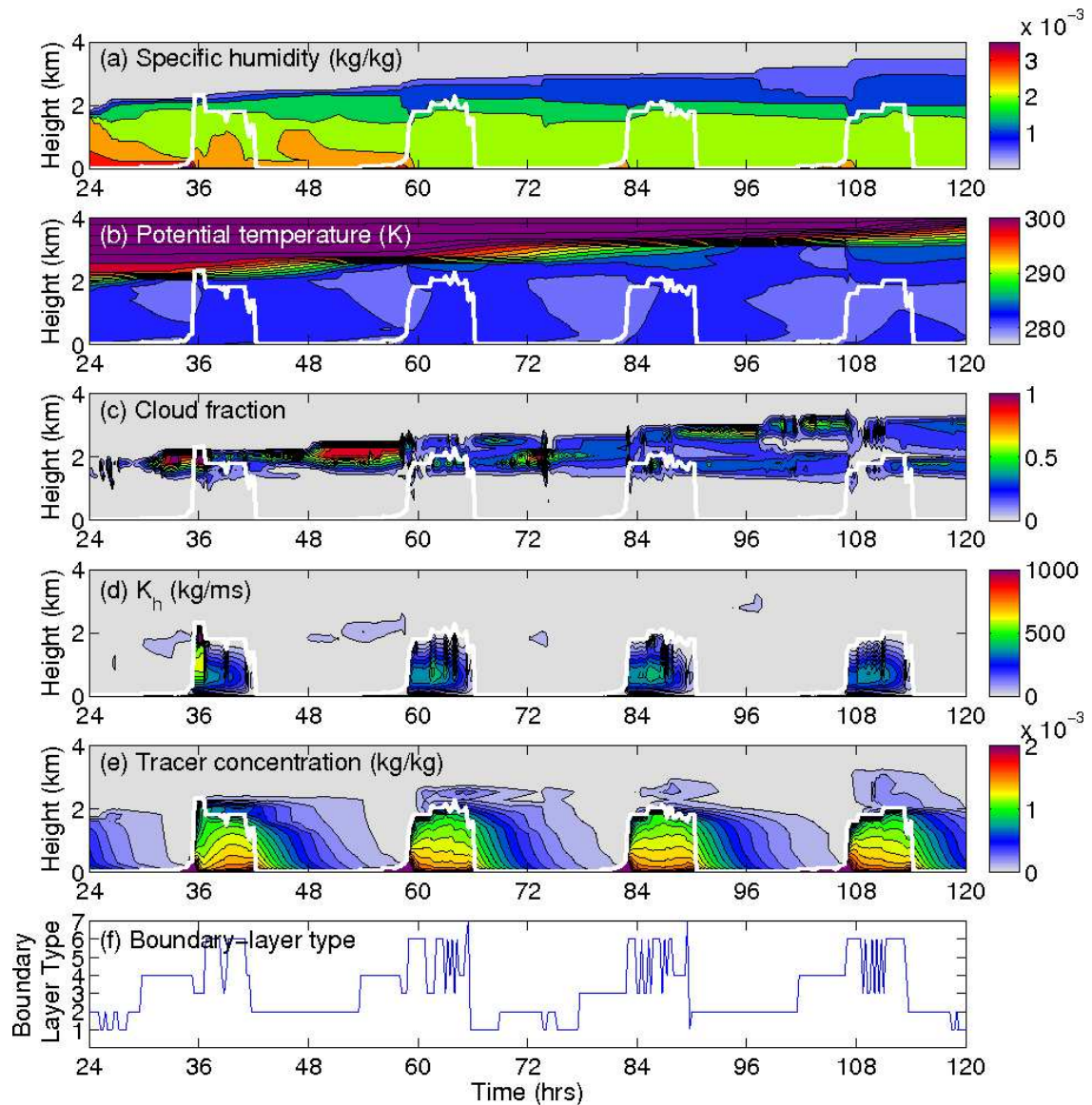
Figure 4.17: As Figure 4.11 but for the *no-top-down* experiment.

2.5 on day 4, due to differences in the timing of boundary layer growth (the boundary layer in the *no-top-down* experiment starts to deepen later due to the diagnosis of a coupled boundary layer (III) rather than a decoupled (IV) one as in the *control* experiment). Higher up in the boundary layer (panels (b) and (c)) tracer concentrations in this experiment are slightly higher than the *control* run. The largest difference is seen for the longest decay time which is approximately a factor of 1.4 greater at 730 m. At 2797 m, there are smaller concentrations in this experiment until day 5 (panel (d)).

Throughout the night the top-down mixing grows and maintains a well-mixed residual layer in the *control* experiment. This is shown by the solid lines in Figure 4.19. When the top-down mixing is turned off the well-mixed layer does not develop so quickly.
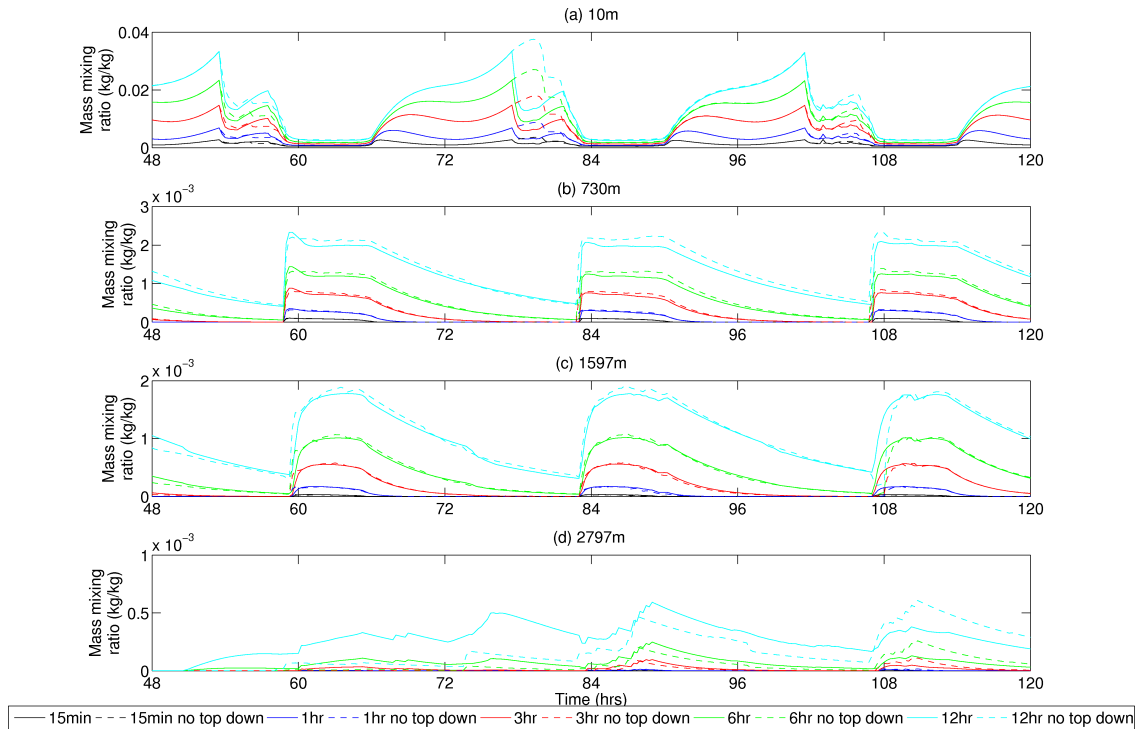
Figure 4.18: The evolution of tracer concentration for days 2–5 of the *control* run (solid lines) and *no-top-down* run(dashed lines) at (a) 10 m, (b) 730 m, (c) 1597 m and (d) 2797 m. The colours indicate the different decay timescales.

Instead, the small amount of elevated shear mixing evolves a much shallower layer of well-mixed tracer, thus giving a pronounced "shoulder" in the vertical profile between the elevated mixed layer and the residual layer. Therefore, concentrations in the lower half of the boundary layer are higher than the *control* experiment by up to a factor of 1.25.

Figure 4.20 shows two day-time vertical profiles of tracer. The shape of the profile is not modified as much as in the night-time case as the day-time is dominated by surface-driven mixing. There are small differences in the magnitude of the tracer concentration that is linked to the difference in boundary-layer top due to the *no-top-down* simulation vacillation between type VI and type III.

To summarise the work in this section, the impact of turning off top-down mixing has little effect on near surface concentrations both in the day and night. However, significant differences in the vertical profile of tracer, up to a factor of 1.25 for 12 hour decay time, can be seen at night when top-down mixing is turned off, which may have implications for boundary-layer chemistry. As expected the differences seen were larger for tracers with longer decay times. Another interesting feature to note is that the lack of top-down mixing reduces boundary-layer temperatures by up to 2 K, which may be due to warm entrained air from the free troposphere not being mixed throughout the depth
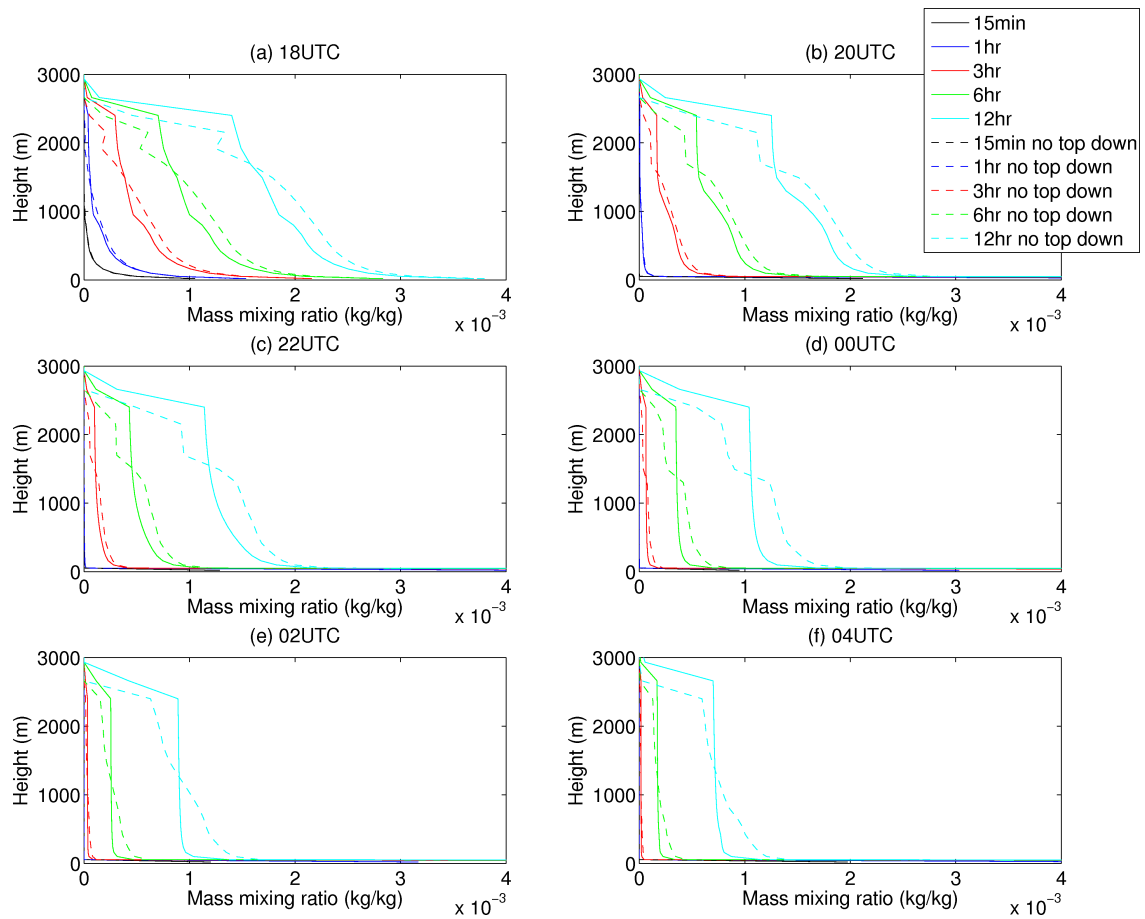
Figure 4.19: The vertical profile of tracer concentration at (a) 18 UTC, (b) 20 UTC, (c) 22 UTC, (d) 00 UTC, (e) 02 UTC, and (f) 04 UTC on day two of the *control* run (solid lines) and *no-top-down* run (dashed lines) for all decay times. The colours indicate the different decay timescales.

of the boundary layer. The turning off of top-down mixing also impacts cloud presence during both the day and night.

4.7 The impact of entrainment on the vertical distribution of tracer

In the remaining part of this chapter a comparison between a SCM run with boundary-layer top entrainment turned off will be compared to the *control* simulation. Turning off the boundary-layer top entrainment is achieved by setting $w_e = 0 \, \mathrm{ms}^{-1}$. Figure 4.21 shows w_e as a function of time for the *control* experiment and the no-entrainment experiment. All initial conditions and forcings applied are the same as the cloudy experiments presented in Section 4.6.

Figure 4.22 shows the evolution of specific humidity, potential temperature, cloud frac-
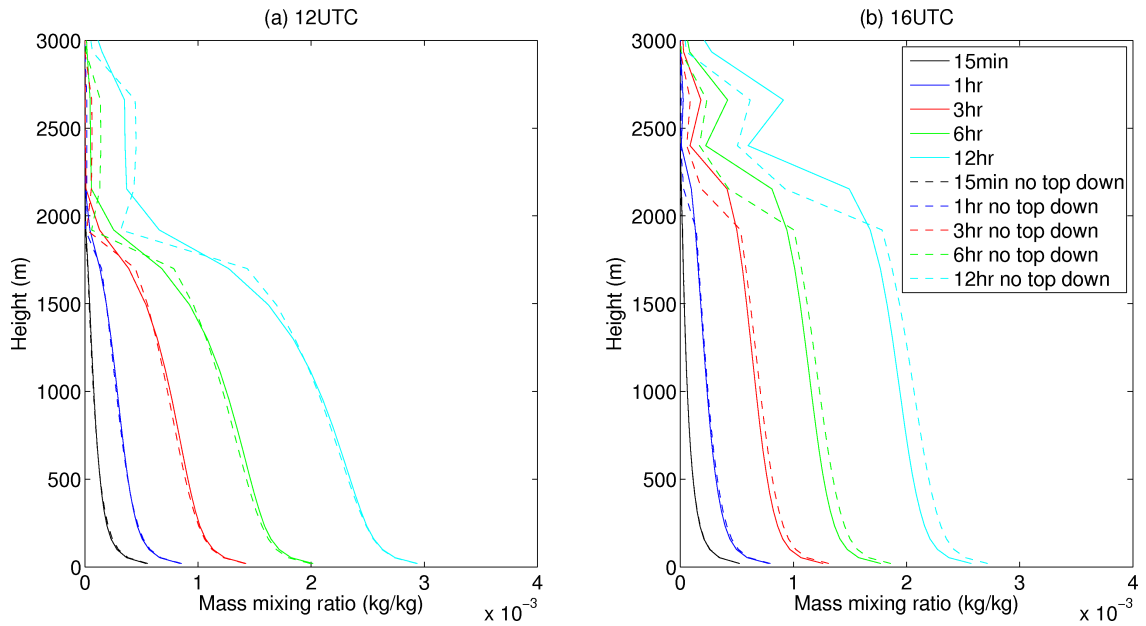
Figure 4.20: The vertical profile of tracer concentration at (a) 12 UTC, (b) 16 UTC on day three of the *control* simulation (solid lines) and *no-top-down* run (dashed lines) for all decay times. The colours indicate the different decay timescales.

tion, diffusivity of heat, tracer distribution and diagnosed boundary-layer type. As the run progresses the boundary layer cools down, which may be attributed to warm tropospheric air not being entrained into the boundary layer in this simulation. As expected (Carson, 1973), the model-diagnosed boundary-layer top is, in general, lower in the *entrainment-off* experiment than the *control* cloudy experiment (see Figure 4.23). The
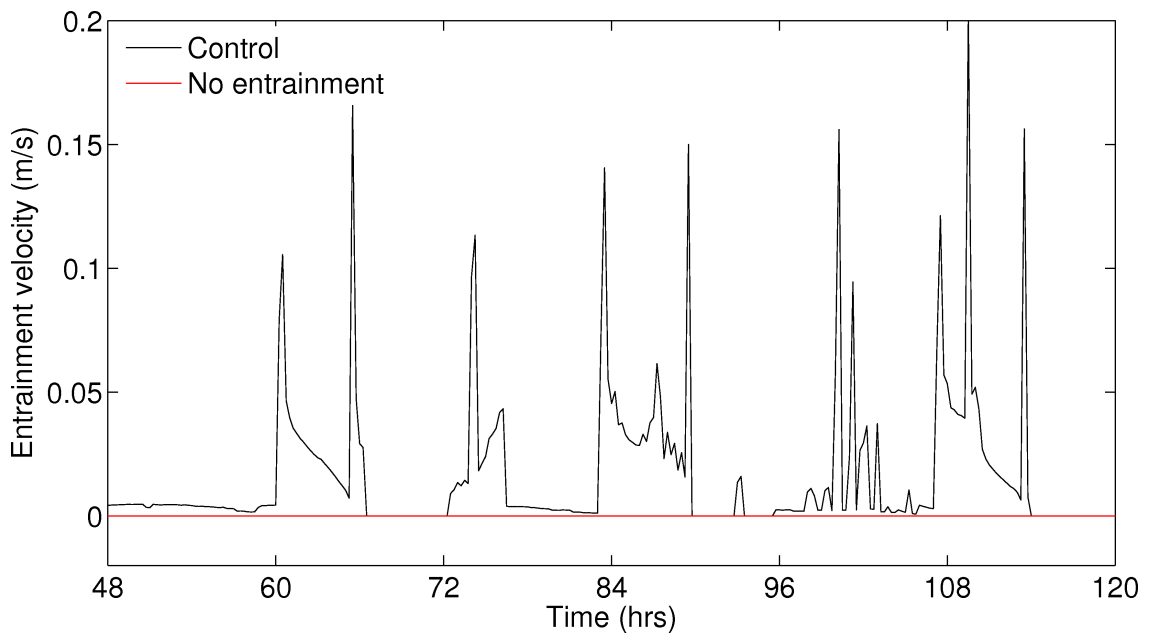
Figure 4.21: Entrainment velocity for days 2–5 of the *control* and *entrainment-off runs*.
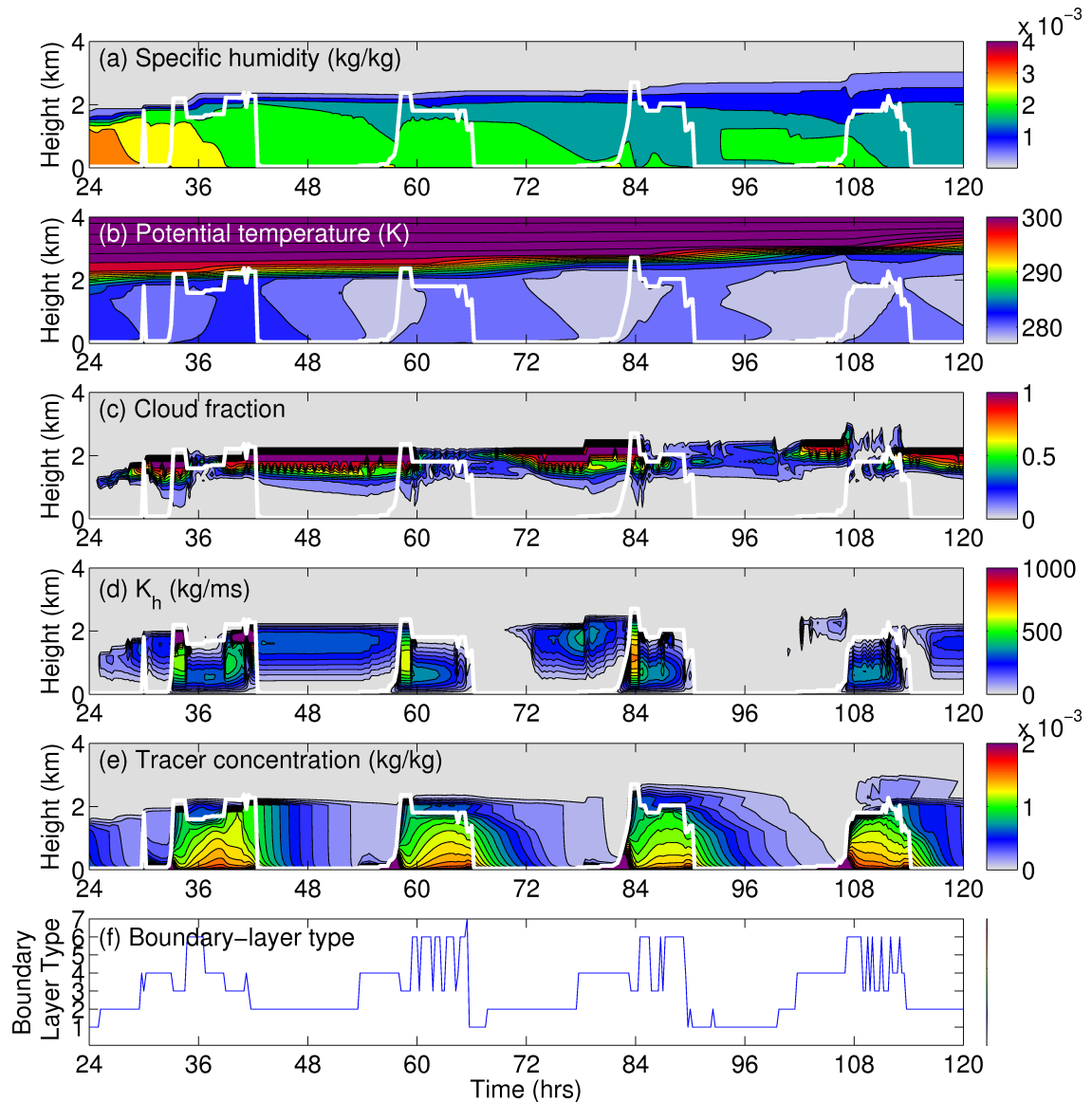
Figure 4.22: As Figure 4.11 but for the *entrainment-off* experiment.

maximum difference in boundary-layer top is over 2 km and this occurs on day 3 where there is a spike in the *entrainment-off* boundary-layer top at approximately 10 UTC before it settles down to a value lower than the *control* experiment. Similar behaviour is seen on day 2 and 4. This is due to the boundary-layer top definition used being different for different boundary-layer types. There does not appear to be a relationship between the magnitude of the difference in entrainment velocity between the two experiments considered here and the difference in boundary-layer top.

The difference in boundary-layer top height leads to a difference in cloud-top height, with the *entrainment-off* experiment having lower cloud top heights. In general, the column-integrated cloud fraction in the *entrainment-off* run is higher than in the *con-*
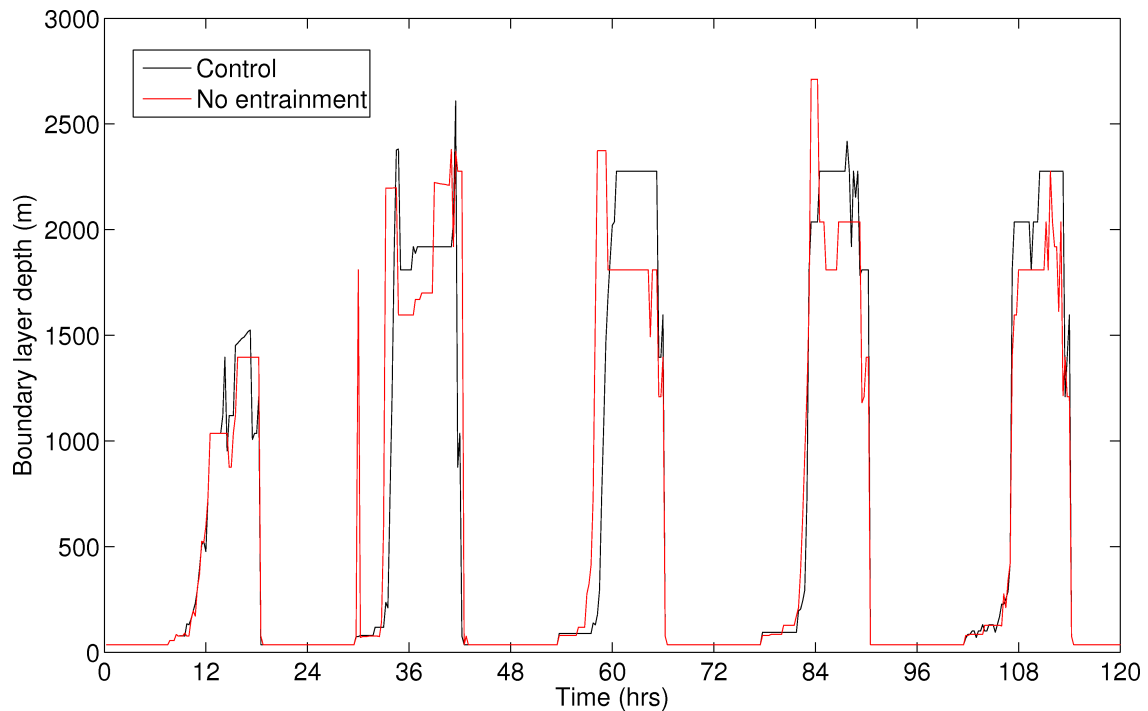
Figure 4.23: The evolution of boundary-layer depth for days 3–5 of the *control* and *entrainment-off* runs.

trol experiment with the largest differences seen at night (1800 UTC–0600 UTC). This supports the theory of Lilly (1968) that entrainment acts to break-up stratocumulus. However, even though the column-integrated cloud fraction is larger in the *entrainment-off* run, the vertical extent of the clouds at night is similar in both runs, and therefore contradicting the theory of stratocumulus deepening by entrainment proposed by Randall (1984). During the day the vertical extent of the cumulus cloud is larger in the *entrainment-off* simulation.

The night-time (1800 UTC–0600 UTC) boundary-layer types diagnosed are similar between the two experiments (mainly type II, stratocumulus over a stable surface layer). The type diagnosed during the morning transition is also the same, type IV (decoupled stratocumulus). The largest differences in type are the timing and frequency of the transition from decoupled stratocumulus (type IV) and well mixed (type III) to cumulus capped (type VI). The during days 3 and 5 the *entrainment-off* simulation flips between type III/IV and VI frequently (time step by time step in some cases) throughout the afternoon (1200 UTC–1800 UTC). However the converse is true on day 4. These differences in boundary-layer type may be due to differences in the boundary-layer cloud highlighted above.

Figure 4.24 panels (a) and (b) show the total diffusivity, K_h in the *entrainment-off* and

control experiment. There are differences between the two diffusivity profiles. During the day-time the *entrainment-off* case has larger values of diffusivity throughout the depth of the boundary layer coinciding with the spikes in boundary-layer height in the morning transition periods. This difference is due to increased diffusivity calculated using the local scheme and non-local surface scheme (see Figure 4.24 panels (d) and (f)). During the night-time there is more diffusivity from the stratocumulus cloud in the *entrainment-off* case. This is true for the local and non-local top-down mixing scheme from day 2 onwards. Along with an increased magnitude the shape of the diffusivity profile is more uniform in time than in the *control* experiment. This is most clearly seen by comparing hours 36–60 in panels (g) and (h).

As discussed above there are differences in the cloud fraction, boundary-layer type and
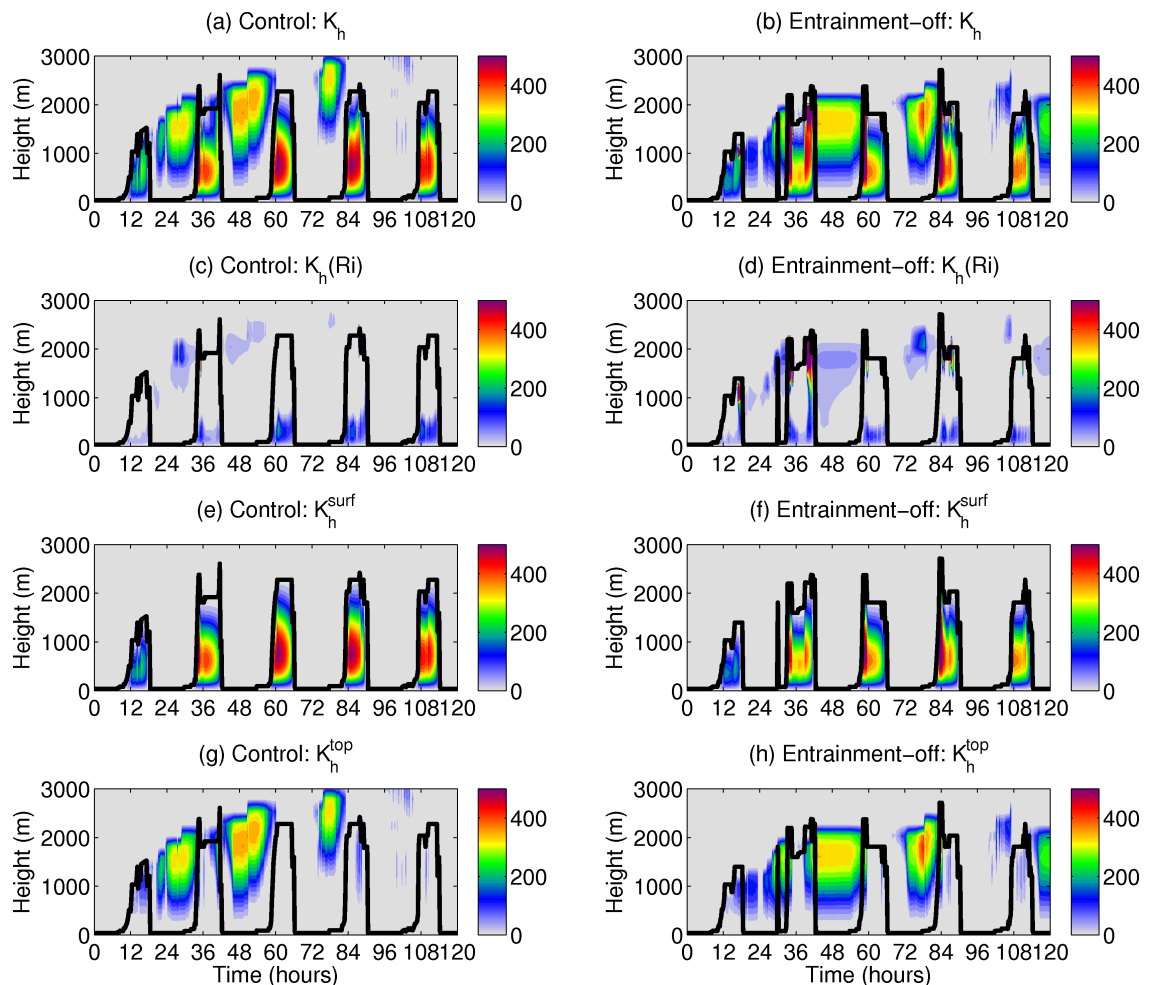
Figure 4.24: (a) Total diffusivity of heat for days 2–5 for the *control* experiment. (b) As (a) but for *entrainment-off*. (c) Local diffusivity of heat for for days 2–5 for the *control* experiment. (d) As (c) but for *entrainment-off*. (e) Non-local surface driven diffusivity of heat for for days 2–5 for the *control* experiment. (f) As (e) but for *entrainment-off*. (g) Non-local top-down diffusivity of heat for for days 2–5 for the *control* experiment. (h) As (g) but for *entrainment-off*.

diffusivity profiles, but do these differences translate into differences in the vertical distribution of tracer? Figure 4.25 shows the evolution of tracer concentration with time for days 2–5 of the experiment at four levels in the column for a 6 hour decay time only. This decay time was chosen as a representative decay time; it is assumed the differences seen with varying decay time are the same as in shown in Section 4.6. Due to the lower boundary-layer top in the entrainment off experiment the near-surface (10 m) tracer concentrations (Figure 4.25 panel (a)) during the day-time are slightly higher, a factor of approximately 1.12, than in the *control* cloudy experiment. The differences seen during the morning transition period are also due the differences in boundary-layer top (seen in Figure 4.23). Similar behaviour is seen in panels (b) and (c) which show the concentration evolution at 730 m and 1597 m respectively, although the night-time exponential decay of tracer concentration is not as smooth in the *entrainment-off* experiment. This could be related to the differences in top-down mixing between the two experiments. Tracer does not reach 2797 m until day 5 in the *entrainment-off* experiment, again this is due to the boundary-layer top being lower in this experiment.

Vertical profiles of tracer concentration for specified times on day 3 are shown in Figure 4.26. Although the effect of differing boundary-layer top height is again apparent, the profiles from both experiments qualitatively have the same shape although the effects of convection on the tracer distribution seems less apparent in *entrainment-off* case. The enhanced top-down mixing at 22 UTC in the entrainment off case has developed an elevated mixed layer that is not seen in the *control* cloud case. This mixed layer continues to deepen until tracer is well mixed throughout the depth of the boundary layer (approximately 0300 UTC).

To summarise entrainment has a small effect on near-surface concentrations due to the differences in boundary-layer top between the *control* and *entrainment-off* experiments. Qualitatively the shape of the vertical profile of tracer is the same in both the *control* and *entrainment-off* cases but the effect on convection is less prominent in the *entrainment-off* experiment. Although there is not a vast impact on tracer distribution, entrainment does impact the diffusivity profile, boundary-layer temperature and cloud fraction.

4.8   Impact on other variables

The experiments above have demonstrated that the misdiagnosis of unstable boundary-layer types (III, IV, V and VI) has little effect on near-surface concentrations of passive

tracer. However, boundary-layer mixing can also impact other near surface variables, namely temperature and humidity. Figure 4.27 shows the 100m temperature for the four experiments presented above. Note that surface temperature was not used as they are calculated by extrapolation from the first model level using surface layer approximations. All simulations have a diurnal cycle in temperature with a the maximum diurnal range of approximately 10 K. The maximum day-time temperature is reached at 1400 UTC for all simulations.

The largest temperature difference seen is between that of the *control* simulation and the *entrainment-off* simulation, with a maximum temperature difference of approximately -3 K. This is expected as entrainment acts to warm the boundary layer, although it is
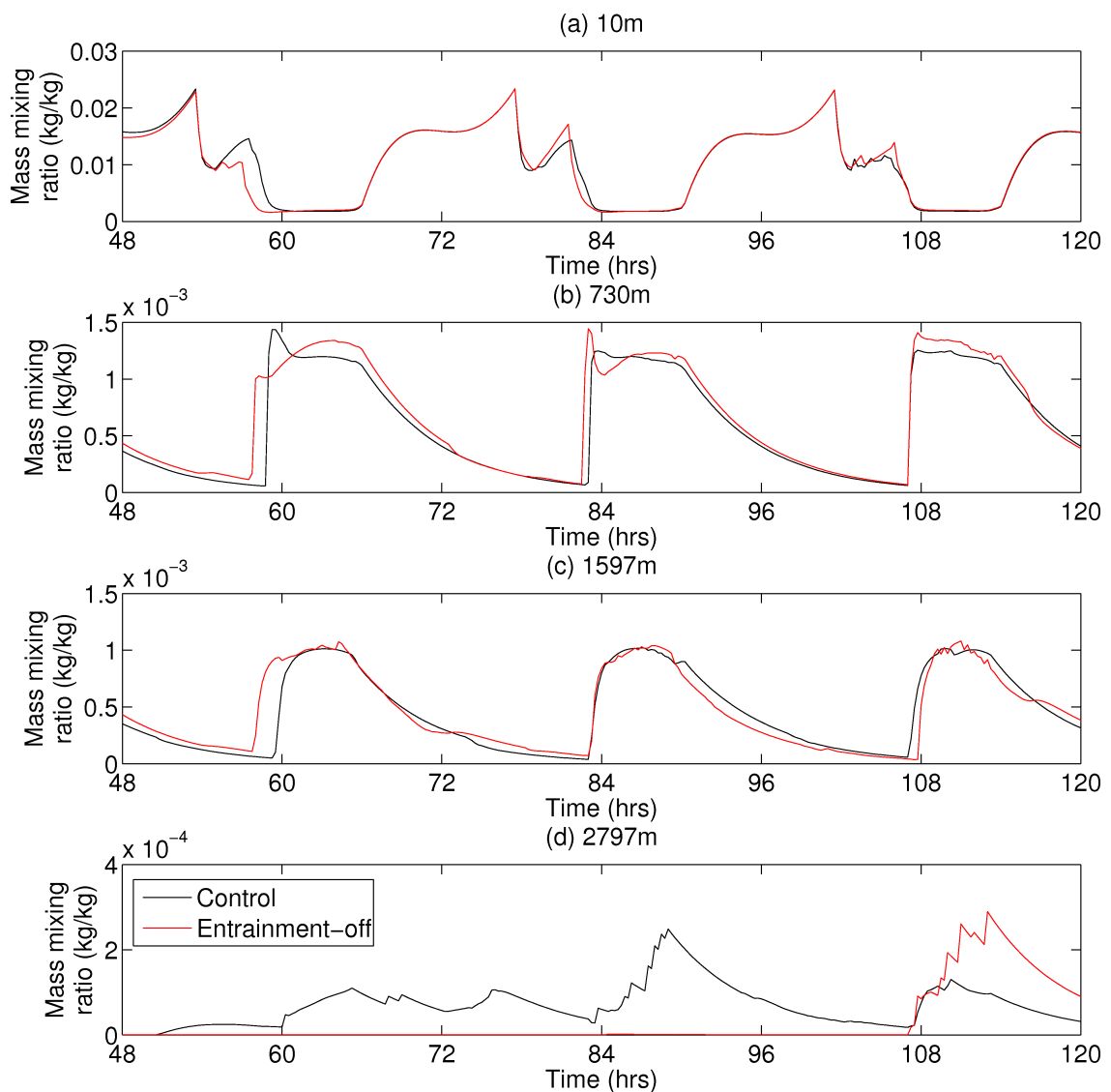
Figure 4.25: The evolution of tracer concentration for days 2–5 of the *control* and *entrainment-off* runs at (a) 10 m, (b) 730 m, (c) 1597 m and (d) 2797 m for the 6 hour decay time only.
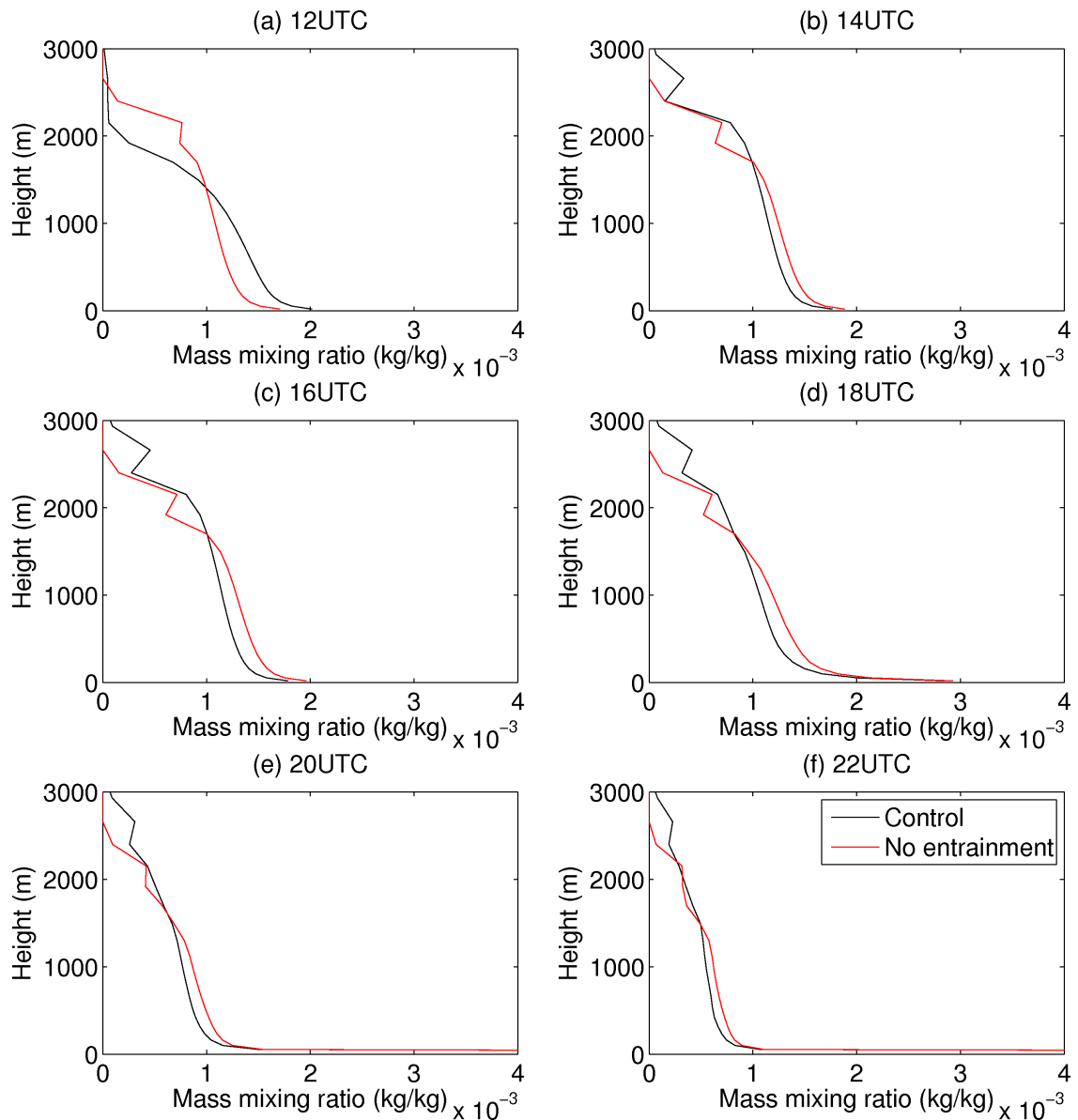
Figure 4.26: The vertical profile of tracer concentration at (a) 12 UTC, (b) 14 UTC, (c) 16 UTC, (d) 18 UTC, (e) 20 UTC, and (f) 22 UTC on day three of the *control* and *entrainment-off* runs for the 6 hour decay time only.

important to note that completely switching off entrainment is not a realistic situation this is an upper limit on the temperature difference due to the entrainment process.

There are also differences between the *control* experiment and the *no-cumulus* and *no-top-down* mixing, although they are not as large as the differences seen in the *entrainment-off* simulation. In the top-down mixing off experiment the temperature can be up to 1 K cooler than the *control* experiment. This is due to the boundary-layer not being as well mixed as in the *control* case. The temperature differences seen in the *no-cumulus* simulation are much smaller (up to 0.5 K on day 5). From this it can be concluded that misdiagnosing boundary-layer type can impact the forecasts of surface temperature. These
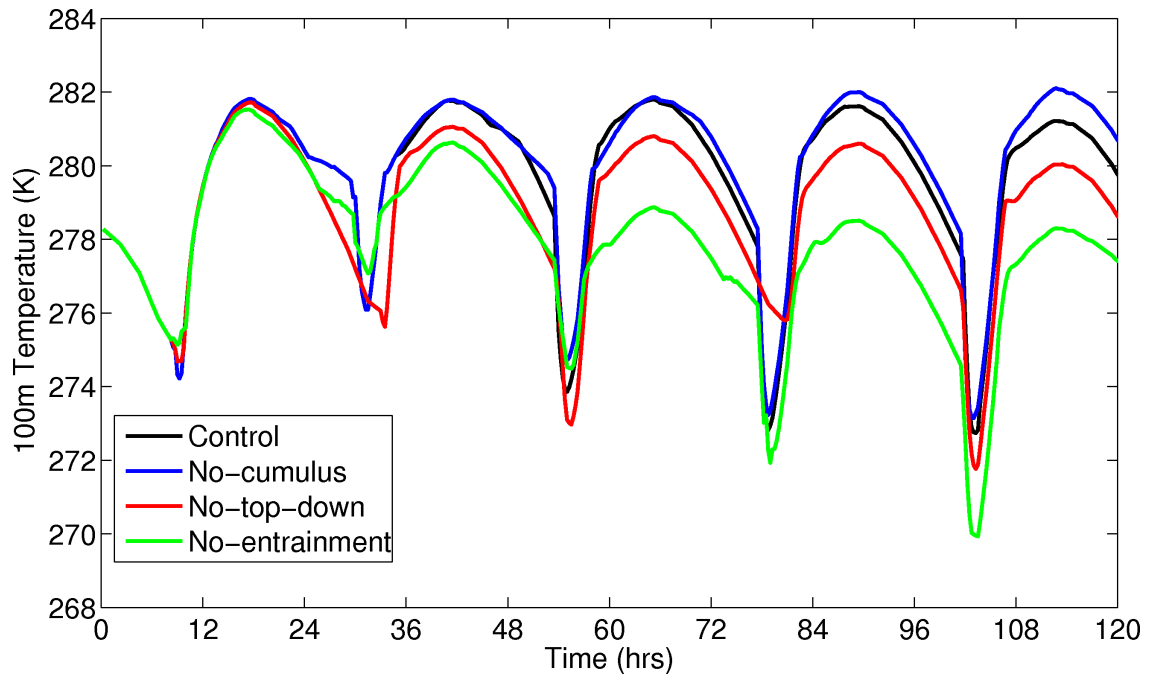
Figure 4.27: The evolution of the 100m temperature for the simulation for the *control*, *no-cumulus*, *no-top-down* and *entrainment-off* runs.

differences could be important for the prediction of frosts.

4.9 Conclusions and implications for air quality forecasting

To try and answer the question posed in the title of this chapter, whether boundary-layer type misdiagnosis affects the vertical distribution of pollutants, five sets of idealised single-column model experiments have been conducted. The experiments were run using the single-column set up of the Met Office Unified Model. Along with the impact of boundary-layer type the effect of tracer decay time on the vertical distribution of tracer was also investigated.

First, the simple clear skies case with the misdiagnosis of the sign of sensible heat flux was considered. It was found that if night-time sensible heat flux was increased from $-20\,\mathrm{Wm^{-2}}$ to $0\,\mathrm{Wm^{-2}}$ the surface concentration of tracer decreased by up to an order of magnitude due to the boundary-layer top collapsing at sunset. Increasing the sensible heat flux again to $10\,\mathrm{Wm^{-2}}$ only decreases the surface concentrations by a comparatively small amount. Having positive sensible heat flux at night is not uncommon in urban locations and this study suggests that for the same weather conditions and emissions, night-time tracer concentrations could be higher in rural areas than in cities. This effect

is greater for tracers with longer decay times. Nocturnal boundary layer behaviour also has a key role in determining the initial chemical conditions for photochemistry, e.g. ozone and NO_2 (Garland & Branson, 1976, Pisano et al., 1997, Doran et al., 2003 and Wang et al., 2006), thus the correct sensible heat flux diagnosis, and therefore the correct diagnosis of type I or type III, is important for pollution forecasts.

The inclusion of cloud in the idealised experiments gives the opportunity to investigate the impact of cumulus convection on the vertical distribution of pollutants. The mis-diagnosis of a cumulus-capped boundary layer as a well-mixed boundary layer results in slightly reduced surface concentrations due to the tracer being mixed over a greater depth. The vertical profile of tracer is also modified. As expected, the vertical profile is more well mixed and does not exhibit the distinct elevated tracer maximum that is seen in the cumulus-capped situation. For the longest decay time, 12 hours, the elevated tracer maximum can persist until the growth of the boundary layer on the next day. The differences in the vertical profiles of tracer could have implications for photochemistry as discussed above.

The impact of turning off top-down mixing, driven by cloud-top cooling, on the vertical distribution of tracer was also investigated. For stable conditions this is the difference between type I (stable surface layer) and type II (decoupled stratocumulus over a stable surface layer). During unstable conditions turning off top-down mixing is the difference between type IV (decoupled stratocumulus) and type III (well mixed). As this is a phe-nomena that takes place well above the surface, turning it off does not have an impact on surface level concentrations. However, it does have an impact on the vertical profile of tracer. At night the top-down mixing acts to keep the residual layer well mixed. This change in the vertical profile may affect the initial chemical conditions for photochem-istry the following day. The effect is not as great during the day, as in this regime surface driven mixing dominates.

Entrainment is another important boundary layer process that affects boundary-layer growth and boundary-layer cloud. When entrainment is switched off the boundary layer is shallower. This has a small effect on surface concentrations due to the dilution effect. The removal of entrainment also reduces the surface temperature by up to 4 K. This is due to the lack of entrainment of warm tropospheric air. Although removing en-trainment completely is not realistic, the entrainment parameterisation used in the Met Office UM is not easily verifiable by observations thus it is possible that the entrainment velocity could be significantly different to the values used in the model.

To summarise, the misdiagnosis of boundary-layer type does have an impact on the vertical profile of tracer, but the impact on surface concentrations is small when the misdiagnosis concerns only unstable boundary-layer types. Surface concentrations may differ by an order of magnitude if the boundary-layer stability is wrongly diagnosed. In a model with interactive chemistry, such as the one being developed as part of the UKCA project, the differences in the vertical profile of particular pollutants may have significant impacts on the initial chemical set up for photochemistry the following day. Also, a study by Lin & McElroy (2010) found that the satellite retrievals of ozone and nitrogen dioxide are affected by the mixing scheme that is applied in the chemistry transport model. Although the surface concentration differences are small they could be important to the health of vulnerable people. It has also been found that the misdiagnosis of type can impact the near surface temperature, thus this could have an impact on surface temperature forecasts and the temperature bias that the operation forecasts exhibit (A. Lock, personal communication).

Immediate further work could be to investigate the impact of the final boundary-layer type, cumulus under a decoupled stratocumulus layer, on the vertical profile of tracer. More realistic case studies could be performed using large scale tendencies and observed surface forcings. This could be extended further by running the cases studies on the full 3D setup of the UM. The single column model could be used to investigate the impact of boundary-layer type misdiagnosis over the ocean. Potentially the decoupling may impact the tracer more over the ocean. In all the experiments presented above no tracer was vented above the temperature inversion marking the boundary between the boundary layer and the free troposphere. Further work could be done to design and conduct experiments to investigate the impact of venting of tracer by convection out of the boundary layer has on surface concentrations. Potentially the single column model could be used to investigate the stability of stratocumulus cloud to entrainment by controlling the equivalent potential temperature jump across the cloud top.

Chapter 5

Summary, discussion and future work

This thesis set out to better understand the role of boundary-layer mixing on the vertical distribution of pollutants in the atmosphere. In particular it aimed to answer the following four questions:

1. How can the atmospheric boundary layer be classified into distinct types using remote sensing measurements?

2. How well does the Met Office model compare with the observationally based classification of boundary-layer type over Chilbolton?

3. To what extent does the skill of a forecast of boundary-layer type in the Met Office model vary with leadtime and model resolution?

4. How does the diagnosis of boundary-layer type in the Met Office model affect the vertical distribution of pollutants in the atmosphere?

These questions have been answered through the development of a new algorithm classifies the boundary layer into distinct types using data from a Doppler lidar and sonic anemometer. This new algorithm was applied to 3 years of observational data from the Chilbolton Facility for Atmospheric and Radio Research (CFARR) and the first ever climatology of boundary-layer type was created. This observational classification of boundary-layer type was then used to assess forecasts of boundary-layer type by the Met Office numerical weather prediction model. The impact of boundary-layer type diagnosis on the vertical distribution of pollutants was assessed using idealised single column model experiments.

5.1 Discussion of results

In Chapter 2 it was demonstrated that it is possible to classify the boundary layer into 9 different types using variables obtained from a continually operating vertically pointing Doppler lidar combined with surface sensible heat flux measurements. This new method has been applied to 3 years of data and the first climatology of boundary-layer type has been produced. This climatology exhibits clear diurnal and seasonal cycles which are dominated by variations in the surface sensible heat flux. The most common boundary-layer type is cloud-free stable boundary layer (30.0%). The most common unstable boundary-layer type is unstable cloud free (15.4%). Decoupled stratocumulus-capped boundary layers, which are little studied over land, occur 10.3% of the time. More cumulus capped boundary layers are diagnosed in spring and summer than in the winter. The most probable diurnal sequence of boundary-layer type has also been investigated. The most probable evolution is that of a cloud free boundary layer evolution , transitioning from stable to unstable depending on the sign of the sensible heat flux (6.4% of the period studied). The "textbook" continental boundary layer evolution of stable, well mixed, cumulus-capped, stable, occurring only 0.9% of the days studied over Chilbolton.

The skill of the UK Met Office 4 km and 12 km models at predicting boundary-layer type has been assessed using the observational time-series of boundary-layer type. There are some differences when the model and observational climatologies are compared, most notable is the prevalence of decoupled stratocumulus cloud and lack of cumulus cloud in the model. However, the seasonal and diurnal cycles seen in both the model and observations are not dissimilar. The most common boundary-layer type in both model and observations is a stable boundary layer. Contingency tables have been used to assess the model's ability to forecast the correct boundary-layer type at the correct time. These tables have been used to assess the following decisions that are made in both the observed and modelled boundary-layer type diagnosis: stability, presence of cumulus cloud, presence of decoupled stratocumulus, presence of more than one layer of cloud and presence of decoupled stratocumulus cloud over a stable surface. The skill score used here was the Symmetric Extremal Dependence Index (SEDI) verification measure (Ferro & Stephenson, 2011). It was found that in the model the decision with the highest skill is stability. This means that the model correctly predicts the stable/unstable transitions. Predicting the presence of more than one layer of cloud given that cumulus is

present has the lowest SEDI value. The three remaining decisions are not significantly more skillful than persistence.

The skill of predicting boundary-layer type is not affected by changing model resolution. This is presumably due to the same parameterisation schemes being applied in both of the model resolutions considered here. The top twenty diurnal evolution sequences were computed for the model and observations. The most common transition pattern in both the model and observations is a stable boundary layer transitioning to a well mixed boundary layer when the sensible heat flux changes sign and then back to stable at night.

A set of idealised single column model experiments with surface emissions of passive tracer were performed to assess the impact of boundary-layer type on the vertical distribution of pollutants. It was found that the largest impact on surface concentrations of tracer was the correct prediction of night-time sensible heat flux. Incorrectly predicting this as stable instead of unstable can lead to surface tracer concentrations being increased by an order of magnitude. Positive sensible heat flux at night is often observed in cities (Grimmond & Oke, 2002). The incorrect prediction of the sign of the city sensible heat flux would result in the over or under prediction of concentrations of pollutants that are harmful to human health. Also, several studies (Garland & Branson, 1976; Pisano et al., 1997; Doran et al., 2003; Wang et al., 2006) have found that the nocturnal boundary layer mixing can influence the initial chemical conditions for photochemistry and therefore influence the ozone and nitrogen oxide concentrations the following day.

Surprisingly, diagnosing cumulus-capped boundary layers instead of well-mixed boundary layers or stratocumulus-topped boundary layers results in slightly higher surface concentrations due to the model diagnosed boundary-layer top being lower in the cumulus-capped case. In the model the vertical transport by convection is less efficient than that achieved by the boundary layer mixing scheme for an equivalent depth of the atmosphere. Cumulus-capped layers also have a less well mixed vertical profile of tracer as the mixing by the convection scheme mixing above the diagnosed boundary-layer top results in higher concentrations at the bottom of the convective cloud than at the top. Diagnosing stratus cloud instead of stratocumulus cloud, and therefore not having any top-down mixing, does not have an impact on surface level concentrations as changes take place only close to boundary-layer top. There are significant differences in the vertical profile of tracer at night, as the residual layer is not well mixed when there is no top-down mixing. The effects are not as pronounced during the day as in this regime surface-driven mixing is also present. In all experiments the differences in

concentrations increased with tracer lifetime.

Entrainment is another important process that is parameterised in models and affects boundary layer growth and formation of boundary layer cloud. When entrainment is switched off in the model the boundary layer is shallower. This has a small effect on surface concentrations due to the dilution effect. However, a larger effect is the reduction of the 100 m temperature, up to 4 K, due to the lack of entrainment of warm tropospheric air. Although removing entrainment completely is not realistic, the entrainment parameterisation used in the Met Office UM is not easily verifiable by observations, and thus it is possible that the true atmospheric entrainment velocity could be significantly different to the values used in the model.

5.2 Future work

There is great potential to expand on the work presented in this thesis. Firstly, Doppler lidar and sonic anemometer data is now available to extend the climatology of boundary-layer type at Chilbolton presented in Chapter 2 by approximately two years. In addition, the algorithm could be applied to any other site that has a co-located Doppler lidar and sonic anemometer. The application could be on a case study or climatological basis. Another suitable location in the UK is the Met Office observational site at Cardington. This and other European sites, such as those used in Cloudnet (Illingworth et al., 2007), could be used to verify the climatology of boundary-layer type over land in a variety of locations. This extension would provide more information on the frequency of stratocumulus cloud over land.

The algorithm could also be used to investigate the impact of surface heterogeneity on boundary-layer mixing. An obvious dataset to use to test this would be that taken by the Advanced Climate Technology:Urban Atmospheric Laboratory (ACTUAL) project that has measurements in central London. This would enable the impact of positive sensible heat flux at night on boundary-layer mixing and structure. Other sites in the Atmospheric Radiation Measurement (ARM) program (Stokes & Schwartz, 1994) could give opportunities to examine case studies and create climatologies of marine (e.g. Azores) and tropical (e.g. Darwin) boundary layers. A climatology of marine boundary-layer cloud, especially stratocumulus which are important for the Earth's radiation balance (Bony et al., 2006), could provide useful observational data to validate climate models. The most common diurnal transitions could be investigated for all these sites using the

method presented in Chapter 2.

The algorithm itself could be further developed to include radar data. This would enable cloud top height to be determined and thus remove the need for an intermediate data processing step for comparison to model data. This development would mean that its application would be less transferable to other observational sites. Small modifications could be made to output convective boundary-layer top, the top of the residual layer, cumulus and stratocumulus cloud base, the transition level in decoupled situations and the depth of penetration of cloud-top driven turbulence. It could also be extend to include the calculation of the turbulent kinetic energy dissipation rate (O'Connor et al., 2010) which would enable evaluations of the intensity of the turbulence predicted in NWP models.

The evaluation of the Met Office model could be extended by including other models in the operational suite (e.g. UKV that has 1.5 km resolution over the UK) and using a different observational site (e.g. Cardington). The evaluation performed in Chapter 3 compared the most probable observational boundary-layer type with the model boundary-layer type diagnosed at one particular timestep. Timestep-resolution model data or an ensemble of forecasts would enable the calculation of a model forecast of the probability of each boundary-layer type. This probabilistic forecast could then be compared to the observational probabilities by comparing the most probable model and observational type as in Chapter 3 techniques.

Both the climatological and SEDI verification performed on the Met Office model in Chapter 3 could be applied to any boundary-layer scheme that had a similar decision process for determining the boundary-layer mixing that needs to be applied. An example of one such scheme is the mass-flux eddy-diffusivity scheme used in the ECMWF operational model (Kohler et al., 2011). However, as discussed it in Chapter 3 it is anticipated that the skill scores over the UK for other models may be lower than that of the Met Office model due to the lower skill at predicting the presence and diurnal cycle of boundary-layer clouds (Barrett et al., 2009; Hogan et al., 2009b).

The next step in the single column modelling work presented in Chapter 4 would be to design an experiment to test the impact of diagnosing a stratocumulus-capped layer with a cumulus layer underneath instead of a cumulus-capped layer. This experiment would be non-trivial to set up. Based on the results of the other sensitivity experiments it is not anticipated that the surface concentrations would differ greatly. However, the

presence of stratocumulus cloud means that there is top-down mixing occurring thus there may be a difference in the vertical profile of tracer. These experiments could be extended further to simulate the marine boundary layer. In this situation there is very little diurnal evolution in the surface fluxes and therefore in the boundary-layer height. Observations show that decoupled stratocumulus cloud is very common over the ocean and therefore there is potential for near surface concentrations to be impacted more than is seen over land.

Studies by Donnell et al. (2001), Agusti-Panareda et al. (2005), Dacre et al. (2007) and Sinclair et al. (2008) found that convection could vent pollutants above the boundary layer into the free troposphere. This venting could potentially enable pollutants to be transported on continental scales. In the experiments conducted in Chapter 4 venting of pollutants was seen above the model diagnosed boundary-layer top by the convection scheme. However, in cumulus-capped boundary layers the model definition of boundary-layer top is the LCL so venting above this level does not mean that the pollutants have escaped the boundary layer. It can be seen in Figure 4.11 that the tracer does not get above the strong temperature inversion which caps the boundary layer. Experiments could be designed to enable tracer to be vented and thus understand the impact of the venting on the surface concentrations of tracer. It is hypothesised that once vented there is no mechanism for the tracer to return in to the boundary layer and thus surface concentrations would be reduced.

However, lidar observations at Chilbolton and Leipzig of the ash plume produced by the 2010 eruption of Eyjafjallajökull showed the ash rapidly mix throughout the boundary layer as it descended (Dacre et al., 2011). Idealised experiments could be setup in the SCM to have a tracer source above the capping temperature inversion to investigate whether this tracer could be entrained into the boundary layer and to investigate the impact of boundary-layer type diagnosis on the possible entrainment.

A further extension would be to consider case study days that could be simulated using observed surface and large scale forcings. This would enable a comparison of the lidar observations and simulated diffusivity profiles. These simulations could also be used to assess the relative importance of horizontal advection and vertical mixing to the distribution of tracer. If enough case studies were performed it could be possible to identify weather regimes that could potentially give the largest differences in the vertical distribution of pollutants. It also may be possible to qualitatively compare modelled passive tracer distributions to observed radon profiles (Williams et al., 2011).

The Met Office boundary-layer scheme categorises the boundary layer into seven different types (Lock & Edwards, 2011). The initial implementation of the scheme only had six categories as this was the number of ways that the different mixing types could be coupled. In the observational algorithm it was decided to have nine categories. An interesting aspect to study would be to determine how many boundary layer types there "should" be. Cluster analysis (Wilks, 1995) could be performed on observational parameters calculated by the algorithm. This technique has been used to group daily weather observations into synoptic types (Kalkstein et al., 1987) and grouping of forecast ensemble members (Tracton & Kalnay, 1993).

As boundary-layer type and thus the mixing parameterisation applied by models is so strongly dependent on the presence and type of cloud it is suggested that the focus should be on better predicting the boundary layer cloud type. Particular attention should be given to the diagnosis of cumulus cloud and the depth constraint that is currently applied. The 400m constraint that is currently applied is potentially missing up to 69% of cumulus cloud, which may be partly causing the low SEDI score for the presence of cumulus cloud. The improvement in boundary-layer cloud representation would also improve the understanding of cloud feedback that will be experienced in a warming climate. It is also possible that boundary-layer type diagnosis feeds back on the atmosphere and affects the evolution of the boundary-layer and thus boundary-layer clouds.

However, with model forecasts starting to be run at sub-1 km resolution larger eddies can be resolved. Thus another focus for research would be to assess how the boundary-layer scheme behaves at these resolutions and whether boundary-layer types are fit for purpose as higher and higher resolutions are used for weather forecasting. Another question to address is whether sharp distinctions between different boundary-layer types is realistic? From a data assimilation perspective switches are undesirable, however having a distinct number of types maybe the best approximation of the atmosphere. Data from Doppler lidars could be further exploited to not only determine discrete boundary-types but to determine diffusivity profiles based on long-term observations for a variety of different atmospheric conditions. This would remove the need to base the profiles used in models on results from large eddy simulations and limited in-situ balloon and aircraft measurements.

Appendix A

How to run the Met Office SCM (Vn 7.8) at the University of Reading

The Single Column Model version of the Unified model can be run locally at the University of Reading. The following instructions are a guide to how to do this. Further information about the SCM and the namelist used to specify input parameters and forcings can be found in the Unified Model Documentation Paper C9 (Wong, 2010).

- Request an account on PUMA at http://cms.ncas.ac.uk/index.php/ component/chronocontact /?chronoformname=PUMA_Registration

- In the UMUI copy the working single column model job xgtce to form the basis of your job

- Copy the following files from /home/grenville/SCMDATA to your local space

    - spec3c_sw_cloud
    - spec3a_sw_hgem1_6oyblean
    - spec3c_lw_cloud
    - spec3a_lw_hadgem1_6onyb
    - gabls2_murkem_tracer_L63_UM78.nml (namelist)
    - L63_41km_20m_20_6km_qs_o1(vertical namelist)

- Take ownership of the UMUI job, by substituting your username in User Information and Submit Method → General Details

- In the UMUI change the file locations of the above files to where you have them located. Files 1&2 (above) are specified in Model Selection → Atmosphere → Sci-

entific Parameters and Sections → Section by Section Choices → SW Radiation → Gen 2. Files 3 &4 are specified in in Model Selection → Atmosphere → Scientific Parameters and Sections → Section by Section Choices → LW Radiation → Gen 2. The vertical name list is specified in Model Selection → Atmosphere → Model resolution and domain → Vertical. The main name list is specified in Model Selection → Atmosphere → Model resolution and domain → Single Column settings.

- Change output file location in the UMUI (same window as namelist location in UMUI)

- Change the output directory in the FCM Configuration → FCM Extract directories

- Before processing the job in the UMUI you need to set up password-less ssh for oak. In order to do this follow the general instructions at http://climate.ncas.ac.uk/ssh/ssh_agent.html where for local you should read puma and for remote read oak.

- Save, process and submit the job in the UMUI.

- To build the executable file model cd into the location of the extracted UM code on the local machine (my location is /home/username/SCUMlocal/um_extracts/job_name/ummodel).

- Type . simon/um_local to setup your environment.

- Type fcm build (this will create a folder called bin with the executable inside). NOTE: this needs to be run on a 64 but machine.

- To run the model

  – cd to /home/username/umui_runs/job_name-number/

  – If you have setup the namelist to do netCDf output then type export LD_LIBRARY_PATH=/home/simon/data/rdata/build/ netcdf/lib:$LD_LIBRARY_PATH

  – Type the location of Now run the executable file by entering its location at /home/username/SCUMlocal/um_extracts/job_name/ummodel/ bin/job_name.exe

- This should give you output in the form of a .dat file. The location of the main ouput file is given in an on-screen message. To output as a netCDF file add strm_format(1) = 4 to the &DIAGS section of the namelist.

References

Abshire, N., Schwiesow, R. & Derr, V. 1974 Doppler Lidar Observations of Hydrometeors. *J. Appl. Meteorol.* **13**, 951–952.

Agusti-Panareda, A., Gray, S. L. & Methven, J. 2005 Numerical modeling study of boundary-layer ventilation by a cold front over Europe. *J. Geophys. Res.* **110**, p. D18,304.

Ahrens, C. D., Jackson, P. L. & Jackson, C. E. 2011 *Meteorology today: an introduction to weather, climate, and the environment*. Cengage Learning.

Alapaty, K., Pleim, J., Raman, S., Niyogi, D. & Byun, D. 1997 Simulation of atmospheric boundary layer processes using local-and nonlocal-closure schemes. *J. Appl. Meteorol.* **36**, 214–233.

Albrecht, B. A., Bretheton, C. S., Johnson, D. W., Schubert, W. H. & Frisch, A. S. 1995 The Atlantic Stratocumulus Transition Experiment - ASTEX. *B. Am. Meteorol. Soc.* **76**, 889–904.

André, J., De Moor, G., Lacarrere, P. & Du Vachat, R. 1978 Modeling the 24-hour evolution of the mean and turbulent structures of the planetary boundary layer. *J. Atmos. Sci.* **35**, 1861–1883.

Andrews, T., Gregory, J. M., Webb, M. J. & Taylor, K. E. 2012 Forcing, feedbacks and climate sensitivity in CMIP5 coupled atmosphere-ocean climate models. *Geophys. Res. Lett.* **39**.

Angevine, W. M., Senff, C. J., White, A. B., Williams, E. J., Koermer, J., Miller, S. T., Talbot, R., Johnston, P. E., McKeen, S. A. & Downs, T. 2004 Coastal boundary layer influence on pollutant transport in New England. *J. Appl. Meteorol.* **43**, 1425–1437.

Baas, P., Bosveld, F., Lenderink, G., Van Meijgaard, E. & Holtslag, A. 2010 How to design single-column model experiments for comparison with observed nocturnal low-level jets. *Q. J. Roy. Meteor. Soc.* **136**, 671–684.

Baldauf, M., Seifert, A., Förstner, J., Majewski, D., Raschendorfer, M. & Reinhardt, T. 2011 Operational convective-scale numerical weather prediction with the COSMO model: description and sensitivities. *Mon. Weather Rev.* **139**, 3887–3905.

Barlow, J. F., Dunbar, T. M., Nemitz, E. G., Wood, C. R., Gallagher, M. W., Davies, F., O'Connor, E. & Harrison, R. M. 2011 Boundary layer dynamics over London, UK, as

observed using Doppler lidar during REPARTEE-II. *Atmos. Chem. Phys* **11**, 2111–2125.

Barnett, T., Ritchie, J., Foat, J. & Stokes, G. 1998 On the space-time scales of the surface solar radiation field. *J. Climate* **11**, 88–96.

Barrett, A. I., Hogan, R. J. & O'Connor, E. J. 2009 Evaluating forecasts of the evolution of the cloudy boundary layer using diurnal composites of radar and lidar observations. *Geophys. Res. Lett.* **36**, p. L17,811.

Beare, R., Macvean, M., Holtslag, A., Cuxart, J., Esau, I., Golaz, J., Jimenez, M., Khairoutdinov, M., Kosovic, B., Lewellen, D. et al. 2006 An intercomparison of large-eddy simulations of the stable boundary layer. *Bound-Lay. Meteorol.* **118**, 247–272.

Beesley, J., Bretherton, C., Jakob, C., Andreas, E., Intrieri, J. & Uttal, T. 2000 A comparison of cloud and boundary layer variables in the ECMWF forecast model with observations at Surface Heat Budget of the Arctic Ocean (SHEBA) ice camp. *J. Geophys. Res.* **105**, 12,337–12,349.

Best, M. J., Pryor, M., Clark, D. B., Rooney, G. G., Essery, R. L. H., Ménard, C. B., Edwards, J. M., Hendry, M. A., Porson, A., Gedney, N., Mercado, L. M., Sitch, S., Blyth, E., Boucher, O., Cox, P. M., Grimmond, C. S. B. & Harding, R. J. 2011 The Joint UK Land Environment Simulator (JULES), model description Part 1: Energy and water fluxes. *Geoscientific Model Development* **4**, 677–699.

Betts, A. & Jakob, C. 2002 Evaluation of the diurnal cycle of precipitation, surface thermodynamics, and surface fluxes in the ECMWF model using LBA data. *J. Geophys. Res* **107**, LBA 12–1–LBA 12–8.

Betts, A. & Miller, M. 1986 A new convective adjustment scheme. Part II: Single column tests using GATE wave, BOMEX, ATEX and arctic air-mass data sets. *Q. J. Roy. Meteor. Soc.* **112**, 693–709.

Blackadar, A. K. 1962 The vertical distribution of wind and turbulent exchange in a neutral atmosphere. *J. Geophys. Res.* **67**.

Bony, S., Colman, R., Kattsov, V., Allan, R., Bretherton, C., Dufresne, J., Hall, A., Hallegatte, S., Holland, M., Ingram, W. et al. 2006 How well do we understand and evaluate climate change feedback processes? *J. Climate* **19**, 3445–3482.

Bony, S. & Dufresne, J.-L. 2005 Marine boundary layer clouds at the heart of tropical cloud feedback uncertainties in climate models. *Geophys. Res. Lett.* **32**, p. L20,806.

Bosveld, F. C., De Bruijn, C. & Holtslag, A. A. M. 2012 Intercomparison of Single-column Models for GABLS3 preliminary Results. In *18th Symp. on Boundary Layers and Turbulence, Boston, MA, Amer. Meteor. Soc*.

Bougeault, P. & André, J.-C. 1986 On the stability of the third-order turbulence closure

for the modeling of the stratocumulus-topped boundary layer. *J. Atmos. Sci.* **43**, 1574–1581.

Bougeault, P. & Lacarrere, P. 1989 Parameterization of Orography-Induced Turbulence in a Mesobeta–Scale Model. *Mon. Weath. Rev.* **117**, 1872–1890.

Boutle, I., Beare, R., Belcher, S. E., Brown, A. & Plant, R. S. 2010 The moist boundary layer under a mid-latitude weather system. *Bound-Lay. Meteorol.* **134**, 367–386.

Burnet, F. & Brenguier, J. 2007 Observational study of the entrainment-mixing process in warm convective clouds. *J. Atmos. Sci.* **64**, 1995–2011.

Byun, D. & Schere, K. L. 2006 Review of the governing equations, computational algorithms, and other components of the Models-3 Community Multiscale Air Quality (CMAQ) modeling system. *Applied Mechanics Reviews* **59**, p. 51.

Carson, D. 1973 The development of a dry inversion-capped convectively unstable boundary layer. *Q. J. Roy. Meteor. Soc.* **99**, 450–467.

Casati, B., Wilson, L. J., Stephenson, D. B., Nurmi, P., Ghelli, A., Pocernich, M., Damrath, U., Ebert, E. E., Brown, B. G. & Mason, S. 2008 Forecast verification: current status and future directions. *Meteorol. Appl.* **15**, 3–18.

Clark, D. B., Mercado, L. M., Sitch, S., Jones, C. D., Gedney, N., Best, M. J., Pryor, M., Rooney, G. G., Essery, R. L. H., Blyth, E., Boucher, O., Harding, R. J., Huntingford, C. & Cox, P. M. 2011 The Joint UK Land Environment Simulator (JULES), model description Part 2: Carbon fluxes and vegetation dynamics. *Geoscientific Model Development* **4**, 701–722.

Clarke, R. H. 1970 Observational studies in the atmospheric boundary layer. *Q. J. Roy. Meteor. Soc.* **96**, 91–114.

Cohen, A., Anderson, H., Ostro, B., Pandey, K., Krzyzanowski, M., Künzli, N., Gutschmidt, K., Pope, A., Romieu, I., Samet, J. & Smith, K. 2004 Urban Air Pollution. In Ezzati, M., Lopez, A., Rodgers, A. & C.U.J.L, M., editors, *Comparative quantification of health risks: Global and regional burden of disease due to selected major risk factors*. WHO, 1353–1434.

Cohen, A., Anderson, H., Ostro, B., Pandey, K., Krzyzanowski, M., Künzli, N., Gutschmidt, K., Pope, A., Romieu, I., Samet, J. & Smith, K. 2005 The global burden of disease due to outdoor air pollution. *J. Toxicol. Env. Health* **68**, 1301–1307.

Cohn, S. A., Mayor, S. D., Grund, C. J., Weckwerth, T. M. & Senff, C. 1998 The lidars in flat terrain (LIFT) experiment. *Bull. Am. Meteor. Soc.* **79**, 1329–1344.

Cullen, M. J. P., Davies, T., Mawson, M. H., James, J. A., Coulter, S. C. & Malcolm, A. 1997 An Overview of Numerical Methods for the Next Generation U.K. NWP and Climate

Model. *Atmosphere-Ocean* **35**, 425–444.

Cuxart, J., Holtslag, A., Beare, R., Bazile, E., Beljaars, A., Cheng, A., Conangla, L., Ek, M., Freedman, F., Hamdi, R. et al. 2006 Single-column model intercomparison for a stably stratified atmospheric boundary layer. *Bound-Lay. Meteorol.* **118**, 273–303.

Cuxart, J., Yague, C., Morales, G., Terradellas, E., Orbe, J., Calvo, J., Fernandez, A., Soler, M. R., Infante, C., Buenestado, P., Espinalt, A., Joergensen, H. E., Rees, J. M., Vila, J., Redondo, J. M., Cantalapiedra, I. R. & Conangla, L. 2000 Stable Atmospheric Boundary-Layer Experiment in Spain (SABLES98): A Report. *Bound-Lay Meteorol.* **96**, 337–370.

Dacre, H., Grant, A., Hogan, R., Belcher, S., Thomson, D., Devenish, B., Marenco, F., Hort, M., Haywood, J., Ansmann, A., Mattis, I. & Clarisse, L. 2011 Evaluating the structure and magnitude of the ash plume during the initial phase of the 2010 Eyjafjallajökull eruption using lidar observations and NAME simulations. *J. Geophys. Res.* **116**, p. D00U03.

Dacre, H. F., Gray, S. L. & Belcher, S. E. 2007 A case study of boundary layer ventilation by convection and coastal processes. *J. Geophys. Res.* **112**, p. D17,106.

Dai, A. & Trenberth, K. 2004 The diurnal cycle and its depiction in the Community Climate System Model. *J. Climate* **17**, 930–951.

Davies, F., Middleton, D. R. & Bozier, K. E. 2007 Urban air pollution modelling and measurements of boundary layer height. *Atmos. Environ* **41**, 4040–4049.

Davies, T., Cullen, M. J. P., Malcolm, A. J., Mawson, M. H., Staniforth, A., White, A. A. & Wood, N. 2005 A new dynamical core for the Met Office's global and regional modelling of the atmosphere. *Q. J. Roy. Meteor. Soc.* **131**, 1759–1782.

Davis, K. J., Gamage, N., Hagelberg, C. R., Kiemle, C., Lenschow, D. H. & Sullivan, P. P. 2000 An Objective Method for Deriving Atmospheric Structure from Airborne Lidar Observations. *J. Atmos. Ocean. Technol.* **17**, 1455–1468.

Davis, L. S. & Dacre, H. F. 2009 Can dispersion model predictions be improved by increasing the temporal and spatial resolution of the meteorological input data? *Weather* **64**, 232–237.

De Meij, A., Gzella, A., Cuvelier, C., Thunis, P., Bessagnet, B., Vinuesa, J., Menut, L. & Kelder, H. 2009 The impact of MM5 and WRF meteorology over complex terrain on CHIMERE model calculations. *Atmos. Chem. Phys* **9**, 6611–6632.

Deardorff, J. 1980 Cloud top entrainment instability. *J. Atmos. Sci.* **37**, 131–147.

Donnell, E. A., Fish, D. J., Dicks, E. M. & Thorpe, A. J. 2001 Mechanisms for pollutant transport between the boundary layer and the free troposphere. *J. Geophys. Res.* **106**, 7847–7856.

Donovan, D., Bird, J., Whiteway, J., Duck, T., Pal, S. & Carswell, A. 1995 Lidar observations of stratospheric ozone and aerosol above the Canadian high arctic during the 1994-95 winter. *Geophys. Res. Lett.* **22**, 3489–3492.

Doran, J., Berkowitz, C., Coulter, R., Shaw, W. & Spicer, C. 2003 The 2001 Phoenix Sunrise experiment: vertical mixing and chemistry during the morning transition in Phoenix. *Atmos. Environ.* **37**, 2365–2377.

Edwards, J. & Slingo, A. 1996 Studies with a flexible new radiation code. I: Choosing a configuration for a large-scale model. *Q. J. Roy. Meteor. Soc.* **122**, 689–719.

Emeis, S., Schafer, K. & Munkel, C. 2008 Surface-based remote sensing of the mixing-layer height - a review. *Meteorol. Z.* **17**, 621–630.

Endlich, R. M., Ludwig, F. & Uthe, E. 1979 An automatic method for determining the mixing depth from lidar observations. *Atmos. Environ.* **13**, 1051–1056.

Essery, R., Best, M. & Cox, P. 2001 MOSES 2.2 Tech. Doc. *Hadley Centre Tech. Rep. 30* .

Fang, Y., Fiore, A. M., Lamarque, J.-F., Horowitz, L. W. & Lin, M. 2013 Using synthetic tracers as a proxy for summertime PM2. 5 air quality over the Northeastern United States in physical climate models. *Geophys. Res. Lett.* .

Ferro, C. A. T. & Stephenson, D. B. 2011 Extremal Dependence Indices: Improved Verification Measures for Deterministic Forecasts of Rare Binary Events. *Weather Forecast.* **26**, 699–713.

Finley, J. 1884 Tornado Prediction. *American Meteorological Journal* **1**, 85–88.

Fischer, P. H., Brunekreef, B. & Lebret, E. 2003 Air pollution related deaths during the 2003 heat wave in the Netherlands. *Atmos. Environ.* **38**, 1083–1085.

Flamant, C., Pelon, J., Flamant, P. H. & Durand, P. 1997 Lidar Determination of the Entrainment Zone Thickness at the Top of the Unstable Marine Atmospheric Boundary Layer. *Bound-Lay. Meteorol.* **83**, 247–284.

Garland, J. & Branson, J. 1976 The mixing height and mass balance of SO2 in the atmosphere above Great Britain. *Atmos. Environ.* **10**, 353–362.

Garratt, J. R. 1992 *The atmospheric boundary layer*. Cambridge University Press, UK.

Gerber, H., Frick, G., Malinowski, S., Brenguier, J. & Burnet, F. 2005 Holes and entrainment in stratocumulus. *J. Atmos. Sci* **62**, 443–459.

Gimson, N. 1997 Pollution transport by convective clouds in a mesocale model. *Q. J. Roy. Meteorol. Soc.* **123**, 1805–1828.

Gregory, D. & Rowntree, P. 1990 A mass flux convection scheme with representation of cloud ensemble characteristics and stability-dependent closure. *Mon. Weather Rev.* **118**, 1483–1506.

Grell, G. A., Knoche, R., Peckham, S. E. & McKeen, S. A. 2004 Online versus offline air quality modeling on cloud-resolving scales. *Geophys. Res. Lett.* **31**, p. L16,117.

Grimmond, C. & Oke, T. 2002 Turbulent heat fluxes in urban areas: Observations and a local-scale urban meteorological parameterization scheme (LUMPS). *J. Appl. Meteorol.* **41**, 792–810.

Hahn, C., Warren, S., London, R., J.and Chervin & Jenne, R. 1990 Atlas of Simultaneous Occurrence of Different Cloud Types over Land. *NCAR Technical Note TN-241+STR* .

Hanna, S. R. & Yang, R. 2001 Evaluations of mesoscale models' simulations of near-surface winds, temperature gradients, and mixing depths. *J. Appl. Meteorol.* **40**, 1095–1104.

Hartmann, D. L. & Short, D. A. 1980 On the use of earth radiation budget statistics for studies of clouds and climate. *J. Atmos. Sci.* **37**, 1233–1250.

Harvey, N. J., Hogan, R. J. & Dacre, H. F. 2013 A method to diagnose boundary-layer type using Doppler lidar. *Q. J. Roy. Meteor. Soc.* .

Haugen, D. A., Kaimal, J. C. & Bradley, E. F. 1971 An experimental study of Reynolds stress and heat flux in the atmospheric surface layer. *Q. J. Roy. Meteor. Soc.* **97**, 168–180.

Hennemuth, B. & Lammert, A. 2006 Determination of the Atmospheric Boundary Layer Height from Radiosonde and Lidar Backscatter. *Bound-Lay. Meterol.* **120**, 181–200.

Hobbs, P. V. 2000 *Introduction to atmospheric chemistry*. Cambridge University Press.

Hogan, R. J., Grant, A. L. M., Illingworth, A. J., Pearson, G. N. & O'Connor, E. J. 2009a Vertical velocity variance and skewness in clear and cloud-topped boundary layers as revealed by Doppler Lidar. *Q. J. Roy. Meteor. Soc* **135**, 635–643.

Hogan, R. J. & Mason, I. B. 2012 Deterministic forecasts of binary events. In Jolliffe, I. T. & Stephenson, D. B., editors, *Forecast Verification A Practitioner's Guide in Atmosphere Science*. Wiley-Blackwell, 31–59.

Hogan, R. J., Munkunda, D. B., O'Connor, E. J. & Illingworth, A. J. 2004 Estimate of the global distribution of stratiform supercooled liquid water clouds using the LITE lidar. *Geophys. Res. Lett.* **31**, p. L05,106.

Hogan, R. J., O'Connor, E. J. & Illingworth, A. J. 2009b Verification of cloud-fraction forecasts. *Q. J. Roy. Meteor. Soc.* **135**, 1494–1511.

Holtslag, A. & Boville, B. 1993 Local versus non-local boundary-layer diffusion in a global climate model. *J. Climate* **6**, 1825–1825.

Holtslag, A. & Moeng, C.-H. 1991 Eddy diffusivity and countergradient transport in the convective atmospheric boundary layer. *J. Atmos. Sci.* **48**, 1690–1698.

Holtslag, A. A. M., Svensson, G., Basu, S., Beare, R., Bosveld, F. C. & Cuxart, J. 2012

Overview of the GEWEX Atmospheric Boundary Layer Study (GABLS). In *Proceedings of the workshop on Diurnal cycles and the stable boundary layer, Reading, UK.*

Hong, S. 2010 A new stable boundary-layer mixing scheme and its impact on the simulated East Asian summer monsoon. *Q. J. Roy. Meteor. Soc.* **136**, 1481–1496.

Hong, S., Noh, Y. & Dudhia, J. 2006 A new vertical diffusion package with an explicit treatment of entrainment processes. *Mon. Weather Rev.* **134**, 2318–2341.

Hong, S.-Y. & Pan, H.-L. 1996 Nonlocal boundary layer vertical diffusion in a medium-range forecast model. *Mon. Weath. Rev.* **124**, 2322–2339.

Hongisto, M. 2005 Uncertainties in the meteorological input of the chemistry-transport models and some examples of their consequences. *Int. J. Environ. Pollut.* **24**, 127–153.

Hu, X., Nielsen-Gammon, J. & Zhang, F. 2010 Evaluation of three planetary boundary layer schemes in the WRF model. *J. Appl. Meteorol. Clim.* **49**, 1831–1844.

Illingworth, A. J., Hogan, R. J., O'Connor, E. J., Bouniol, D., Brooks, M. E., Delanoe, J., Donovan, D. P., Eastment, J. D., Gaussiat, N., Goddard, J. W., Haeffelin, M., Klein Baltink, H., Krasnov, O. A., Pelon, J., Piriou, J. M., Protat, A., Russchenberg, H. W. J., Seifert, A., Tompkins, A. M., van Zadelhoff, G. J., Vinit, F., Willen, U., Wilson, D. & Wrench, C. L. 2007 Cloudnet - Continuous evaluation of cloud profiles in seven operational models using ground-based observations. *B. Am. Meteorol. Soc.* **88**, 883–898.

Jiang, H., Cotton, W., Pinto, J., Curry, J. & Weissbluth, M. 2000 Cloud resolving simulations of mixed-phase Arctic stratus observed during BASE: Sensitivity to concentration of ice crystals and large-scale heat and moisture advection. *J. Atmos. Sci.* **57**, 2105–2117.

Jolliffe, I. T. & Stephenson, D. B. 2012 *Forecast Verification: A Practitioner's's Guide in Atmospheric Science*. Wiley, The Atrium, Southern Gate, Chichester, West Sussex, England PO19 8SQ.

Kaimal, J. & Finnigan, J. J. 1994 *Atmospheric Boundary Layer Flows Their Structure and Measurement*. Oxford University Press, New York.

Kalkstein, L., Tan, G. & Skindlov, J. 1987 An evaluation of three clustering procedures for use in synoptic climatological classification. *J. Appl. Meteorol.* **26**, 717–730.

Klein, S. A. & Hartmann, D. L. 1993 The seasonal cycle of low stratiform clouds. *J. Climate.* **6**, 1587–1606.

Kohler, M., Ahlgrimm, M. & Beljaars, A. 2011 Unified treatment of dry convective and stratocumulus topped boundary layers in the ECMWF model. *Q. J. Roy. Meteor. Soc.* **137**, 43–57.

Kollias, P., Tselioudis, G. & Albrecht, B. A. 2007 Cloud climatology at the Southern Great

Plains and the layer structure, drizzle and atmospheric modes of continental stratus. *J. Geophys. Res.* **112**, p. D09,116.

Korsholm, U., Baklanov, A., Gross, A. & Sørensen, J. 2009 On the importance of the meteorological coupling interval in dispersion modeling during ETEX-1. *Atmos. Environ.* **43**, 4805–4810.

Kovacs, T. & McCormick, M. 2003 Observations of Typhoon Melissa during the Lidar In-Space Technology Experiment (LITE). *J. Appl. Meteorol.* **42**, 1003–1013.

Kowol-Santen, J., Beekmann, M., Schmitgen, S. & Dewey, K. 2001 Tracer analysis of transport from the boundary layer to the free troposphere. *Geophys. Res. Lett.* **28**, 2907–2910.

Kumar, A. & Goyal, P. 2011 Forecasting of air quality index in Delhi using principal component regression technique. *Atmos. Poll. Res.* **2**, 436–444.

Lazarus, S. M., Krueger, S. K. & Mace, G. G. 2000 A cloud climatology of the Southern Great Plains ARM CART. *J. Climate.* **13**, 17621,775–403.

Lean, W., H, Clark, P. A., Dixon, M., Roberts, N. M., Fitch, A., Forbes, R. & Halliwell, C. 2008 Characteristics of high-resolution versions of the met office unified model for forecasting convection over the United Kingdom. *Mon. Weather Rev.* **136**, 3408–3424.

LeMone, M. A. 1990 Some Observations of Vertical Velocity Skewness in the Convective planetary Boundary Layer. *J. Atmos. Sci.* **47**, 1163–1169.

Lenderink, G., Siebesma, A., Cheinet, S., Irons, S., Jones, C., Marquet, P., üLLER, F., Olmeda, D., Calvo, J., Sánchez, E. et al. 2004 The diurnal cycle of shallow cumulus clouds over land: A single-column model intercomparison study. *Q. J. Roy. Meteor. Soc.* **130**, 3339–3364.

Lenschow, D. H., Lothon, M., Mayor, S. D., Sullivan, P. P. & Canut, G. 2012 A comparison of higher-order vertical velocity moments in the convective boundary layer from lidar with in-situ measurements and large-eddy simulation. *Bound-Lay. Meteorol.* **143**, 107–123.

Lenschow, D. H., Wyngaard, J. C. & Pennell, W. T. 1980 Mean-field and second-moment budgets in a baroclinic, convective boundary layer. *J. Atmos. Sci.* **37**, 1313–1326.

Lilly, D. 1968 Models of cloud-topped mixed layers under a strong inversion. *Q. J. Roy. Meteor. Soc.* **94**, 292–309.

Lin, J. & McElroy, M. 2010 Impacts of boundary layer mixing on pollutant vertical profiles in the lower troposphere: Implications to satellite remote sensing. *Atmos. Environ.* **44**, 1726–1739.

Liu, S. & Liang, X.-Z. 2010 Observed Diurnal Cycle Climatology of Planetary Boundary Layer Height. *J. Climate* **23**, 5790–5809.

Livezey, R. E. 2012 Deterministic forecasts of binary events. In Jolliffe, I. T. & Stephenson, D. B., editors, *Forecast Verification A Practitioner's Guide in Atmosphere Science*. Wiley-Blackwell, 61–75.

Lock, A. 1998 The parametrization of entrainment in cloudy boundary layers. *Q. J. Roy. Meteor. Soc.* **124**, 2729–2753.

Lock, A. 2001 The numerical representation of entrainment in parameterizations of boundary layer turbulent mixing. *Mon. Weather Rev.* **129**, 1148–1163.

Lock, A. & Edwards, J. 2011 The parameterization of boundary layer processes. *UM Documentation Paper 24* .

Lock, A. P., Brown, A. R., Bush, M. R., Martin, G. M. & Smith, R. N. B. 2000 A new boundary-layer mixing scheme - 1. Scheme description and single-column model tests. *Mon. Weather. Rev.* **128**, 3187–3199.

Lohmann, U., Humble, J., Leaitch, W., Isaac, G. & Gultepe, I. 2001 Simulations of ice clouds during FIRE ACE using the CCCMA single-column model. *J. Geophys Res.* **106**, 15,123–15.

Lothon, M., Lenschow, D. H. & Mayor, S. D. 2006 Coherence and scale of vertical velocity in the convective boundary layer from a Doppler lidar. *Bound-Lay. Meteorol.* **121**, 521–536.

Lothon, M., Lenschow, D. H. & Mayor, S. D. 2009 Doppler Lidar Measurements of Vertical Velocity Spectra in the Convective Planetary Boundary Layer. *Bound-Lay. Meterol.* **132**, 205–226.

Louis, J. 1979 A parametric model of vertical eddy fluxes in the atmosphere. *Bound-Lay. Meteorol.* **17**, 187–202.

Lumley, J. L. & Khajeh-Nouri, B. 1974 Computational modeling of turbulent transport. *Adv. Geophys.* **18**, 169–192.

Luna, R. E. & Church, H. W. 1972 A Comparison of Turbulence Intensity and Stability Ratio Measurements to Pasquill Stability Classes. *J. Appl. Meteorol.* **11**, 663–669.

MacVean, M. & Mason, P. 1990 Cloud-top entrainment instability through small-scale mixing and its parameterization in numerical models. *J. Atmos. Sci.* **47**, 1012–1030.

Martin, G. M., Bush, M. R., Brown, A. R. & Smith, R. N. B. 2000 A new boundary-layer mixing scheme - 2. Tests in Climate and Mesoscale Models. *Mon. Weather Rev.* **128**, 3200–3217.

Mass, C., Ovens, D., Westrick, K. & Colle, B. 2002 Does increasing horizontal resolution produce more skillful forecasts. *B. Amer. Meteor. Soc* **83**, 407–430.

Melfi, S., Whiteman, D. & Ferrare, R. 1989 Observation of atmospheric fronts using Ra-

man lidar moisture measurements. *J. Appl. Meteorol.* **28**, 789–806.

Mellor, G. & Yamada, T. 1982 Development of a turbulence closure model for geophysical fluid problems. *Rev. Geophys. Space Ge.* **20**, 851–875.

Mellor, G. L. & Yamada, T. 1974 A hierarchy of turbulence closure models for planetary boundary layers. *J. Atmos. Sci.* **31**, 1791–1806.

Menzies, R. & Hardesty, R. 1989 Coherent Doppler lidar for measurements of wind fields. *Proceedings of the IEEE* **77**, 449–462.

Metcalfe, S., Whyatt, J., Broughton, R., Derwent, R., Finnegan, D., Hall, J., Mineter, M., O'Donoghue, M. & Sutton, M. 2001 Developing the Hull Acid Rain Model: its validation and implications for policy makers. *Environmental Science & Policy* **4**, 25 – 37.

Minguzzi, E., Bedogni, M., Carnevale, C. & Pirovano, G. 2005 Sensitivity of CTM simulations to meteorological input. *Int. J. Environ. Pollut.* **24**, 36–50.

Mittermaier, M. 2012 A critical assessment of surface cloud observations and their use for verifying cloud forecasts. *Q. J. Roy. Meteor. Soc.* .

Moeng, C., Lenschow, D. & Randall, D. 1995 Numerical investigations of the roles of radiative and evaporative feedbacks in stratocumulus entrainment and breakup. *J. Atmos. Sci.* **52**, 2869–2883.

Moeng, C. & Rotunno, R. 1990 Vertical-Velocity Skewness in the Bouyancy-Driven Boundary Layer. *J. Atmos. Sci.* **47**, 1149–1162.

Mok, T. M. & Rudowicz, C. Z. 2004 A lidar study of the atmospheric entrainment zone and mixed layer over Hong Kong. *Atmos. Res.* **69**, 147–163.

Morrison, H., Curry, J. A. & Khvorostyanov, V. I. 2005 A new double-moment microphysics parameterization for application in cloud and climate models. Part I: Description. *J. Atmos. Sci.* **62**, 1665–1677.

Moyer, K. A. & Young, G. S. 1991 Observations of Vertical Velocity Skewness within the Marine Stratocumulus-Topped Boundary Layer. *J. Atmos. Sci.* **48**, 403–410.

Mueller, S. F. 2009 Model representation of local air quality characteristics. *J. Appl. Meteorol. Clim.* **48**, 945–961.

Newsom, R. K., Ligon, D., Calhoun, R., Heap, R., Cregan, E. & Princevac, M. 2005 Retrieval of Microscale Wind and Temperature Fields from Single- and Dual-Doppler Lidar Data. *J. Appl. Meteorol.* **44**, 1324–1345.

Nicholls, S. & Turton, J. 1986 An observational study of the structure of stratiform cloud sheets: Part II. Entrainment. *Q. J. Roy. Meteor. Soc.* **112**, 461–480.

Nolan, D., Zhang, J. & Stern, D. 2009 Evaluation of planetary boundary layer parameterizations in tropical cyclones by comparison of in situ observations and high-resolution

simulations of Hurricane Isabel (2003). Part I: Initialization, maximum winds, and the outer-core boundary layer. *Mon. Weather Rev.* **137**, 3651–3674.

Norris, J. R. 1998 Low Cloud Type over the ocean from surface observations - 2. Geographical and seasonal variations. *J. Climate.* **11**, 383–403.

O'Connor, E., Illingworth, A., Brooks, I., Westbrook, C., Hogan, R., Davies, F. & Brooks, B. 2010 A method for estimating the turbulent kinetic energy dissipation rate from a vertically pointing Doppler lidar, and independent evaluation from balloon-borne in situ measurements. *J. Atmos. Ocean. Tech.* **27**, 1652–1664.

Pan, Y., Chamecki, M. & Isard, S. 2012 Dispersion of Heavy Particles Emitted from Area Sources in the Unstable Atmospheric Boundary Layer. *Bound-Lay. Meteorol.* , 1–22.

Pearson, G., Davies, F. & Collier, C. 2008 An Analysis of the Performance of the UFAM Pulsed Doppler Lidar for Observing the Boundary Layer. *J. Atmos. Ocean. Technol.* **26**, 240–250.

Pearson, G., Davies, F. & Collier, C. 2010 Remote Sensing of the tropical rain forest boundary layer using pulsed Doppler lidar. *Atmos. Chem. Phys. Discuss.* **10**, 5021–5049.

Petch, J. C., Craig, G. C. & Shine, K. P. 1997 A comparison of two bulk microphysical schemes and their effects on radiative transfer using a single-column model. *Q. J. Roy. Meteor. Soc.* **123**, 1561–1580.

Petch, J. C., Willett, M., Wong, R. Y. & Woolnough, S. J. 2007 Modelling suppressed and active convection. Comparing a numerical weather prediction, cloud-resolving and single-column model. *Q. J. Roy. Meteor. Soc.* **133**, 1087–1100.

Pisano, J., McKendry, I., Steyn, D. & Hastie, D. 1997 Vertical nitrogen dioxide and ozone concentrations measured from a tethered balloon in the Lower Fraser Valley. *Atmos. Environ.* **31**, 2071–2078.

Platt, C. 1973 Lidar and radioimetric observations of cirrus clouds. *J. Atmos. Sci.* **30**, 1191–1204.

Pleim, J. 2007 A combined local and nonlocal closure model for the atmospheric boundary layer. Part I: Model description and testing. *J. Appl. Meteorol. Clim.* **46**, 1383–1395.

Poulos, G. S., Blumen, W., Fritts, D. C., Lundquist, J. K., Sun, J., Burns, S. P., Nappo, C., Banta, R., Newsom, R., Cuxart, J., Terradellas, E., Balsley, B. & Jensen, M. 2002 CASES-99: A Comprehensive Investigation of the Stable Nocturnal Boundary Layer. *B. Am. Meteorol. Soc.* **83**, 555–581.

Powell, M. 1980 Evaluations of Diagnostic Marine Boundary-Layer Models Applied to Hurricanes. *Mon. Weather Rev.* **108**, p. 757.

Pul, W., Holtslag, A. & Swart, D. 1994 A comparison of ABL heights inferred routinely

from lidar and radiosondes at noontime. *Bound-Lay. Meteorol.* **68**, 173–191.

Queen, A. & Zhang, Y. 2008 Examining the sensitivity of MM5CMAQ predictions to explicit microphysics schemes and horizontal grid resolutions, Part IIIThe impact of horizontal grid resolution. *Atmos. Environ.* **42**, 3869 – 3881.

Ramanathan, V., Crutzen, P., Kiehl, J. & Rosenfeld, D. 2001 Aerosols, climate, and the hydrological cycle. *Science* **294**, 2119–2124.

Randall, D. 1980 Conditional instability of the first kind upside-down. *J. Atmos. Sci* **37**, 125–130.

Randall, D. 1984 Stratocumulus cloud deepening through entrainment. *Tellus A* **36**, 446–457.

Reynolds, O. 1895 On the Dynamical Theory of Incompressible Viscous Fluids and the Determination of the Criterion. *Philos. T. R. Soc. A* **186**, pp. 123–164.

Rogers, D., Businger, J. & Charnock, H. 1985 A numerical investigation of the JASIN atmospheric boundary layer. *Bound-Lay. Meteorol.* **32**, 373–399.

Sanderson, B. M., Piani, C., Ingram, W., Stone, D. & Allen, M. 2008 Towards constraining climate sensitivity by linear analysis of feedback patterns in thousands of perturbed-physics GCM simulations. *Clim. Dynam.* **30**, 175–190.

Schlunzen, K. H. & Sokhi, R. S. 2006 Overview of tools and methods for meteorological and air pollution mesoscale model evaluation and user training. *Joint report of COST Action 728 (Enhancing mesoscale meteorological modelling capabilities for air pollution and dispersion applications) and GURME (GAW Urban Research Meteorology and Environment project)* .

Seaman, N. L. 2000 Meteorological modeling for air-quality assessments. *Atmos. Environ.* **34**, 2231 – 2259.

Seibert, P., Beyrich, F., Gryning, S.-E., Joffre, S., Rasmussen, A. & Tercier, P. 2000 Review and intercomparison of operational methods for the determiniation of the mixing height. *Atmos. Environ.* **34**, 1001–1027.

Sengupta, M., Clothiaux, E. & Ackerman, T. 2004 Climatology of warm boundary layer clouds at the ARM SGP site and their comparison to models. *J. Climate* **17**, 4760–4782.

Shin, H. S. & Hong, S. 2011 Intercomparison of Planetary Boundary-Layer Parametrizations in the WRF Model for a Single Day from CASES-99. *Bound-Lay. Meteorol.* **139**, 261–281.

Siebesma, A., Soares, P. & Teixeira, J. 2007 A combined eddy-diffusivity mass-flux approach for the convective boundary layer. *J. Atmos. Sci.* **64**, 1230–1248.

Siebesma, A. & Teixeira, J. 2000 An advection–diffusion scheme for the convective

boundary layer: Description and 1D results. In *14th Symp. on Boundary Layers and Turbulence, Aspen, CO, Amer. Meteor. Soc*, volume 4.

Sinclair, V. A., Gray, S. L. & Belcher, S. E. 2008 Boundary-layer ventilation by baroclinic life cycles. *Q. J. Roy. Meteor. Soc.* **134**, 1409–1424.

Singles, R., Sutton, M. & Weston, K. 1998 A multi-layer model to describe the atmospheric transport and deposition of ammonia in Great Britain. *Atmospheric Environment* **32**, 393 – 399.

Smith, R. 1990 A scheme for predicting layer clouds and their water content in a general circulation model. *Q. J. Roy. Meteor. Soc.* **116**, 435–460.

Smyth, S. C., Yin, D., Roth, H., Jiang, W., Moran, M. D. & Crevier, L.-P. 2006 The Impact of GEM and MM5 Modeled Meteorological Conditions on CMAQ Air Quality Modeling Results in Eastern Canada and the Northeastern United States. *J. Appl. Meteorol. Clim.* **45**, 1525–1541.

Soares, P., Miranda, P., Siebesma, A. & Teixeira, J. 2004 An eddy-diffusivity/mass-flux parametrization for dry and shallow cumulus convection. *Q. J. Roy. Meteor. Soc.* **130**, 3365–3383.

Sorbjan, Z. 1989 *Structure of the atmospheric boundary layer*. Prentice Hall, New Jersey.

Spiegel, M. R. & Stephens, L. J. 1998 *Schaum's outline of theory and problems of statistics*. McGraw-Hill, London.

Stedman, J. R. 2003 The predicted number of air pollution related deaths in the UK during the August 2003 heatwave. *Atmos. Environ.* **38**, 1087–1090.

Stensrud, D. 1996 Importance of low-level jets to climate: A review. *J. Climate* **9**, 1698–1711.

Stensrud, D. & Weiss, S. 2002 Mesoscale model ensemble forecasts of the 3 May 1999 tornado outbreak. *Weather Forecast.* **17**, 526–543.

Stephenson, D. B. 2000 Use of the 'odds ratio' for diagnosing forecast skill. *Weather Forecast.* **15**, 221–232.

Stern, R., Builtjes, P., Schaap, M., Timmermans, R., Vautard, R., Hodzic, A., Memmesheimer, M., Feldmann, H., Renner, E., Wolke, R. et al. 2008 A model intercomparison study focussing on episodes with elevated PM10 concentrations. *Atmos. Environ.* **42**, 4567–4588.

Stevens, B., Moeng, C., Ackerman, A., Bretherton, C., Chlond, A., de Roode, S., Edwards, J., Golaz, J., Jiang, H., Khairoutdinov, M. et al. 2005 Evaluation of large-eddy simulations via observations of nocturnal marine stratocumulus. *Mon. Weather Rev.* **133**, 1443–1462.

Steyn, D. G., Baldi, M. & Hoff, R. M. 1999 The Detection of Mixed Layer Depth and Entrainment Zone Thickness from Lidar Backscatter Profiles. *J. Atmos. Ocean. Technol.* **16**, 953–959.

Stokes, G. & Schwartz, S. 1994 The Atmospheric Radiation Measurement (ARM) Program: Programmatic background and design of the cloud and radiation test bed. *B. Am. Meteorol. Soc.* **75**.

Stull, R. B. 1976 The energetics of entrainment across a density interface. *J. Atmos. Sci.* **33**, 1260–1278.

Stull, R. B. 1988 *An Introduction to Boundary Layer Meteorology*. Kluwer Academic Publishers, The Netherlands.

Sukoriansky, S., Galperin, B. & Perov, V. 2005 Application of a new spectral theory of stably stratified turbulence to the atmospheric boundary layer over sea ice. *Bound-Lay. Meteorol.* **117**, 231–257.

Sukoriansky, S., Galperin, B., Perov, V. et al. 2006 A quasi-normal scale elimination model of turbulence and its application to stably stratified flows. *Nonlinear Pro. Geoph.* **13**, 9–22.

Svensson, G. 1996 A numerical model for chemical and meteorological processes in the atmospheric boundary layer. Part II: A case study of the air quality situation in Athens, Greece. *J. Appl. Meteorol.* **35**, 955–973.

Svensson, G., Holtslag, A. A. M., Kumar, V., Mauritsen, T., Steeneveld, G., Angevine, W. M., Bazile, E., Beljaars, A., de Bruijn, E., Cheng, A., Conangla, L., Cuxart, J., Ek, M., Falk, M. J., Freedman, F., Kitagawa, H., Larson, V. E., Lock, A., Mailhot, J., Masson, V., Park, S., Pleim, J., Soderberg, S., Weng, W. & Zampieri, M. 2011 Evaluation of the Diurnal Cycle in the Atmospheric Boundary Layer Over Land as Represented by a Variety of Single-Column Models: The Second GABLS Experiment. *Bound-Lay. Meteorol.* **140**, 177–206.

Tabachnick, B. G. & Fidell, L. S. 1989 *Using multivariate statistics*. Harper and Row, New York.

Tracton, M. & Kalnay, E. 1993 Operational ensemble prediction at the National Meteorological Center: Practical aspects. *Weather Forecast.* **8**, 379–398.

Troen, I. & Mahrt, L. 1986 A simple model of the atmospheric boundary layer; sensitivity to surface evaporation. *Bound-Lay. Meteorol.* **37**, 129–148.

Vihma, T., Kilpelinen, T., Rontu, L., Anderson, P. S., Orr, A., Phillips, T., Finkele, K., Rodrigo, J. S., Holtslag, A. A. M. & Svensson, G. 2012 Towards the fourth GEWEX atmospheric boundary layer model intercomparison study (GABLS4): exploration of

very stable conditions over an Antarctic ice shelf. In *20th Symp. on Boundary Layers and Turbulence, Boston, MA, Amer. Meteor. Soc*.

Von Storch, H. & Zwiers, F. W. 1999 *Statistical analysis in Climate Research*. Cambridge.

Wang, Q. & Albrecht, B. 1994 Observations of cloud-top entrainment in marine stratocumulus clouds. *J. Atmos. Sci.* **51**, 1530–1547.

Wang, S., Ackermann, R., Stutz, J. et al. 2006 Vertical profiles of O3 and NOx chemistry in the polluted nocturnal boundary layer in Phoenix, AZ: I. Field observations by long-path DOAS. *Atmos. Chem. Phys.* **6**, 2671–2693.

Warner, T. T., Fizz, R. R. & Seaman, N. L. 1983 A Comparison of Two Types of Atmospheric Transport Models–Use of Observed Winds Versus Dynamically Predicted Winds. *J. Appl. Meteorol.* **22**, 394–406.

Weaver, E., Bilbro, J., Dunkin, J., Johnson, S., Jones, W., Harris, C. & DiMarzio, C. 1981 Pulsed Doppler lidar for the detection of turbulence in clear air. *NASA. Langley Research Center The 1980 Aircraft Safety and Operating Probl, Pt. 1 p 313-327(SEE N 81-19035 10-03)* .

Webb, M. J., Senior, C. A., Sexton, D. M. H., Ingram, W. J., Williams, K. D., Ringer, M. A., McAvaney, B. J., Colman, R., Soden, B. J., Gudgel, R., Knutson, T., Emori, S., Ogura, T., Tsushima, Y., Andronova, N., Li, B., Musat, I., Bony, S. & Taylor, K. 2006 On the contribution of local feedback mechanisms to the range of climate sensitivity in two GCM ensembles. *Clim. Dynam.* **27**, 7–38.

Weitkamp, C. 2005 *Lidar: Range-Resolved Optical Remote Sensing of the Atmosphere*. Springer, Singapore.

Werner, C. 2005 Doppler wind lidar. In Weitkamp, C., editor, *Lidar: Range-Resolved Optical Remote Sensing of the Atmosphere*. Springer, 325–354.

Westbrook, C. D., Illingworth, A. J., O'Connor, E. J. & Hogan, R. J. 2010 Doppler lidar measurements of oriented planar ice crystals falling from supercooled and glaciated layer clouds. *Q. J. Roy. Meteor. Soc.* **136**, 260–276.

Wichmann, M. & Schaller, E. 1986 On the determination of the closure parameters in higher-order closure models. *Bound-Lay Meteorol.* **37**, 323–341.

Wilks, D. A. 1995 *Statistical Methods in the Atmospheric Sciences*. Academic Press, London.

Williams, A., Zahorowski, W., Chambers, S., Griffiths, A., Hacker, J., Element, A. & Werczynski, S. 2011 The vertical distribution of radon in clear and cloudy daytime terrestrial boundary layers. *J. Atmos. Sci.* **68**, 155–174.

Wilson, D. R. & Ballard, S. P. 1999 A microphysically based precipitation scheme for the UK meteorological office unified model. *Q. J. Roy. Meteor. Soc.* **125**, 1607–1636.

Wolke, R., Schrder, W., Schrdner, R. & Renner, E. 2012 Influence of grid resolution and meteorological forcing on simulated European air quality: A sensitivity study with the modeling system COSMOMUSCAT. *Atmos. Environ.* **53**, 110 – 130.

Wong, R. 2010 The Single Column Model. *UM Documentation Paper C9* .

Wood, C. R., Lacser, A., Barlow, J. F., Padhra, A., Belcher, S. E., Nemita, E., Helfter, C., Famulari, D. & Grimmond, C. S. B. 2010 Turbulent Flow at 190m Height Above London During 2006-2008: A Climatology and the Applicability of Similarity Theory. *Bound-Lay Meteorol.* **137**, 77–96.

World Health Organisation 2003 Influenza.

World Health Organisation 2006 World Health Organisation Air quality guidelines for particulate matter, ozone, nitrogen dioxide and sulfur dioxide, Global update 2005.

Wyant, M., Bretherton, C., Chlond, A., Griffin, B., Kitagawa, H., Lappen, C., Larson, V., Lock, A., Park, S., De Roode, S. et al. 2007 A single-column model intercomparison of a heavily drizzling stratocumulus-topped boundary layer. *J. Geophys. Res.* **112**, p. D24,204.

Wyngaard, J. C. 1990 Scalar fluxes in the planetary boundary layertheory, modeling, and measurement. *Bound-Lay Meteorol.* **50**, 49–75.

Yamada, T. & Mellor, G. 1975 A simulation of the Wangara atmospheric boundary layer data. *J. Atmos. Sci.* **32**, 2309–2329.

Yamaguchi, T. & Randall, D. 2008 Large-eddy simulation of evaporatively driven entrainment in cloud-topped mixed layers. *J. Atmos Sci* **65**, 1481–1504.

Zampieri, M., Malguzzi, P. & Buzzi, A. 2005 Sensitivity of quantitative precipitation forecasts to boundary layer parameterization: a flash flood case study in the Western Mediterranean. *Natural Hazards and Earth System Sciences* **5**, 603–612.

Zanis, P., Katragkou, E., Tegoulias, I., Poupkou, A., Melas, D., Huszar, P. & Giorgi, F. 2011 Evaluation of near surface ozone in air quality simulations forced by a regional climate model over Europe for the period 1991–2000. *Atmos. Environ.* **45**, 6489–6500.

Zeman, O. & Lumley, J. L. 1976 Modeling buoyancy driven mixed layers. *J. Atmos. Sci.* **33**, 1974–1988.

Zhang, D. & Zheng, W. 2004 Diurnal cycles of surface winds and temperatures as simulated by five boundary layer parameterizations. *J. Appl. Meteorol.* **43**, 157–169.

Zhang, M., Lin, W., Klein, S., Bacmeister, J., Bony, S., Cederwall, R., Del Genio, A., Hack, J., Loeb, N., Lohmann, U. et al. 2005 Comparing clouds and their seasonal variations in 10 atmospheric general circulation models with satellite measurements. *J. Geophys. Res* **110**, p. D15.

Zhu, P., Bretherton, C., Köhler, M., Cheng, A., Chlond, A., Geng, Q., Austin, P., Golaz, J., Lenderink, G., Lock, A. et al. 2005 Intercomparison and interpretation of single-column model simulations of a nocturnal stratocumulus-topped marine boundary layer. *Mon. Weather Rev.* **133**, 2741–2758.